Geochronology of Landslides in the Kluane Lake Region, Southwest Yukon

by

Nora Whelan

B.Sc., Dalhousie University, 2017

B.Sc., Dalhousie University, 2014

Thesis Submitted in Partial Fulfillment of the
Requirements for the Degree of
Master of Science

in the
Department of Earth Sciences
Faculty of Science

SIMON FRASER UNIVERSITY

Summer 2022

Declaration of Committee

Name:	**Nora Whelan**
Degree:	**Master of Science**
Title:	**Geochronology of Landslides in the Kluane Lake Region, Southwest Yukon**
Committee:	**Chair:** **Glyn Williams-Jones** Professor, Earth Sciences
	Brent Ward Supervisor Professor, Earth Sciences
	John Gosse Committee Member Professor, Earth and Environmental Sciences Dalhousie University
	Kristen Kennedy Committee Member Surficial Geologist Yukon Geological Survey
	Andrée Blais-Stevens Examiner Research Scientist/Geologist Geological Survey of Canada

Abstract

Landslides are dangerous, expensive, and ubiquitous hazards that affect people globally. The Kluane Lake region of southwest Yukon is prone to landsliding owing to its relatively high relief, seismic activity, and climate conditions conducive to slope failure. The purpose of this research is to determine the ages of rock slides in Kluane Lake region to contribute to a regional landslide frequency and help establish triggering mechanisms and causal conditions. Five rock slides (Sheep Mountain, Gladstone-1 and -2, Aishihik, and Generc) were dated using terrestrial cosmogenic nuclides, radiocarbon dating, and dendrochronology. The resulting ages were: Sheep Mountain *ca.,* 2.0 cal kyr BP; Gladstone-1, 10.5 ± 0.3 cal kyr BP; Gladstone-2, 11.2 ± 0.3 cal kyr BP; Aishihik, ca. 5.7 ± 0.4 cal kyr BP; Generc, 1996-1997 CE. Regional paleoseismic records suggest Sheep Mountain may have been triggered by a seismic event 2.2 cal kyr BP. While seismicity may have triggered all five events, Gladstone-1 and -2 were potentially conditioned by glacial debuttressing following deglaciation around 11 kyr ago and possibly concomitant permafrost thaw. Aishihik may have been triggered by a paleoseismic event dated at 6.1 ± 0.1 cal kyr BP. Generc may have been conditioned by tectonic fracturing due to its proximity to the Denali Fault and ultimately failed due to weakened bedrock. The new chronological results will provide an important foundation for future landslide hazard assessment studies related to seismicity and climate change in a region undergoing rapid development with expensive infrastructure and rapid landscape change.

Keywords: Denali Fault System; terrestrial cosmogenic nuclide dating; dendrochronology; radiocarbon dating; landslide dating; co-seismic landslides

Dedication

This project could not have been completed without the support of my family and friends, so this is for them!

I also dedicate this to all those who pursue academics and feel like they might not deserve to be there. You do.

Acknowledgements

A very special thanks to Brent, John, and Kristen for all your guidance! It takes a team to complete a project like this and I thank you for all the time and patience!

I would like to acknowledge the tremendous efforts at Dalhousie's CRISDal Laboratory: John, Guang, Sean, Sydney, and Winson. I would also like to acknowledge all those at Lawrence Livermore and Keck Carbon Cycle Facility who processed my samples. Completing a thesis during a pandemic could not have been completed without the assistance of all these individuals.

Thank you, Panya Lipovsky, Britta Jensen, and Andrée Blais-Stevens, for your personal correspondences; your information was greatly appreciated! Thank you to the YGS, for all your support and access to your offices while I prepared for my field season.

Thank you to Icefields Discovery for hosting us at your beautiful facility and Crey and Kelly for assisting me.

Thank you to the Kluane and Aishihik and Champagne First Nations for allowing me to conduct my research on your land.

Table of Contents

List of Tables

List of Figures

List of Acronyms

AMS	Accelerator Mass Spectrometry
a.s.l.	Above Sea Level
^{10}Be	Beryllium – 10
^{14}C	Carbon – 14
^{36}Cl	Chlorine – 36
CRISDal	Cosmic Ray Isotopes Science at Dalhousie
GCR	Galactic cosmic radiation
HCl	Hydrochloric Acid
HNO_3	Nitric Acid
KCC AMS	Keck Carbon Cycle AMS Facility
KLA	Kluane Lake Area
n^o	Neutron
KS	Kluane Schist
NRCan	Natural Resources Canada
^{14}N	Nitrogen – 14
p^+	Proton
PRIME Lab	Purdue Rare Isotope Measurement Laboratory
SOP	Standard operating procedure
TCN	Terrestrial cosmogenic nuclides
n_{th}	Thermal neutron
USGS	United States Geological Survey
WRT	White River Tephra
YGS	Yukon Geological Survey

Chapter 1. Introduction

Southwest Yukon is a unique setting characterized by some of the highest rock uplift rates in world (Bruhn *et al.,* 2012; Ojo *et al.*, 2021), combined with extensive glaciation. These processes lead to high erosion rates and unloading (Enkelmann *et al.* 2015), active fault lines, and highly variable microclimatic zones (Scudder 1997; Smith *et al.,* 2004). Landslides are a common occurrence in this dynamic landscape and their formation can be attributed to a variety of triggers: over-steepened slopes created by cyclical glaciations, permafrost thaw, seismic activity, remobilization of slope materials, and structural integrity loss on bedrock slopes. This thesis is the first to attempt to chronologically constrain large-scale rock slides and contribute to landslide frequency analyses by directly dating five rock landslides within the Kluane Lake region.

1.2. Rationale & Objectives

Large-scale rock slides are common in southwest Yukon and have the potential to cause direct injury, death, and infrastructure damage, as well as secondary impacts such as damage to fisheries resulting in reduced fish stocks (Guthrie, 2013). At least 700 people in Canada have died from landslides since 1771 (Blais-Stevens, 2020) and globally there are at least several thousand deaths per year (Perkins, 2012). Canada ranks as one of the top 20 countries worldwide to be financially affected by geological hazards, and millions of dollars are lost every year to direct impacts and preventative expenditures related to mass wasting. This does not include the cascading financial consequences that these hazards can create (Guthrie, 2013). Improving our ability to predict landslides decreases these costs through preventative measures to create safer environments for people inhabiting landslide-prone regions. It also decreases the financial burden of landslides on infrastructure and allows us to plan for secondary effects of mass wasting processes on fragile ecosystems. Risk assessments will be instrumental in the ongoing development of northern communities and will require an understanding of the frequency of landslides in this region. Provincial, Indigenous, and Federal
governments fund operations such as highways, fiber-optics installation, pipeline right-of-way construction, and other essential industries that can benefit from further understandings of landslides in the Kluane Lake region.

Although there are many observations of earthquakes (Jibson *et al.,* 2006; Lamontagne *et al.,* 2008; Leonard *et al.,* 2008; Lipovsky *et al.,* 2008; Seitz *et al.,* 2008; Natural Resources Canada; United States Geological Survey; among others) and landslides (Rampton, 1979a,b,c; Clague, 1981, Everard, 1994, Huscroft *et al.,* 2004; Blais-Stevens *et al.,* 2010; Koch *et al.,* 2014; Brideau *et al.,* 2016; 2019; Bessette-Kirton & Coe, 2020; among others) in southwest Yukon, few pre-historic earthquakes are dated (Seitz *et al.,* 2008; Blais-Stevens *et al.,* 2020), and even fewer landslides have been successfully correlated with seismic events (Brideau *et al.,* 2009; Brideau, 2014; Koch *et al.,* 2014). Reconstructing the timing and triggers of past landslides improves our ability to predict future landslides. Extensive fieldwork and laboratory work are required to gain this knowledge; this is normally a costly endeavour and requires the analysis of multiple mass movements to determine a probabilistic landslide frequency (Morgan *et al.,* 1992; Bell & Glade, 2004; Sterlacchini *et al.,* 2007; LaHusen, 2019).

To understand how and when landslides occur, it is important to differentiate between two commonly used terms: conditioning and triggering. Hervás & Bobrowsky (2009) describe conditioning mechanisms as are any factors that contribute to slope failure; factors such as internal features (pre-existing faults, fractures, joints, rock bridges, lithology) (Zêzere, *et al.* 1999; Chen *et al.,* 2018), glacial debuttressing (Lewis 1954; Grämiger *et al.,* 2017; McColl *et al.,* 2010), permafrost thaw (Dramis *et al.,* 1995; Patton *et al.,* 2019; Hilger *et al.,* 2021), or unloading (Fernandes *et al.,* 2004). These are factors that increase the probability of catastrophic failures but may not be the exact reason why a slope fails. Conversely, a triggering mechanism is the direct cause of a catastrophic failure, *e.g.,* a proximal, shallow, high magnitude seismic event (Antinao & Gosse, 2009) or high intensity rainfall, acting on a previously conditioned slope (Sæmundsson *et al.,* 2018; Fan *et al.,* 2021; Pfiffner *et al.,* 2021). Landslide triggers act upon pre-existing zones of weakness, thereby exceeding a slope's internal structural integrity threshold and creating a failure plane. However, not every mass wasting event has a distinct triggering event; sometimes a slope simply fails due to the previous conditioning.

The overall objective of this project is to facilitate the future creation of a landslide-age database for the Kluane Lake region that can be used as a chronological constraint in landslide hazard assessments as well as regional paleoseismology.

Through field investigation, laboratory analysis, and data interpretation I will contribute to this goal by:

1) providing new ages on five large rock slides in the Kluane Lake region.
2) attempting to link those slides to previously known seismic events or periods of climate change.
3) testing the existing chronology compiled at Sheep Mountain (Clague, 1981; Koch *et al.,* 2014) with TCN.

Landslides around the Kluane Lake area have not been extensively dated. An improved understanding of when large scale mass wasting events have occurred, how frequently they recur, and what their triggering/conditioning mechanisms may be, will be a significant contribution to future landslide risk assessments in the region.

1.3. Study Area

The study area is in southwest Yukon and is within the bounds of the greater Kluane region (Figs. 1.1, 1.2). It extends ~250 km from the White River to the Aishihik River and extends ~70 km from the southwestern tip of Kluane Lake to Gladstone Lakes in the north. The region includes the communities of Haines Junction, Burwash Landing and Destruction Bay. It is transected by the Alaska Highway Corridor which travels through Haines Junction towards Kluane Lake where it continues northwest into Alaska. Five landslides were examined within the study area which include: 1) Generc, 2) Sheep Mountain, 3) Gladstone-1, 4) Gladstone-2, and 5) Aishihik. Several of these landslides are outside of the Kluane Lake area, such as Aishihik, which is ~30 km northeast of Haines Junction, as well as Generc, which is closer to the White River area. For the sake of simplicity, the study area, which will henceforth be referred to as the Kluane Lake area (KLA), will consist of the overall Kluane Lake region and the two landslides outside of that area.

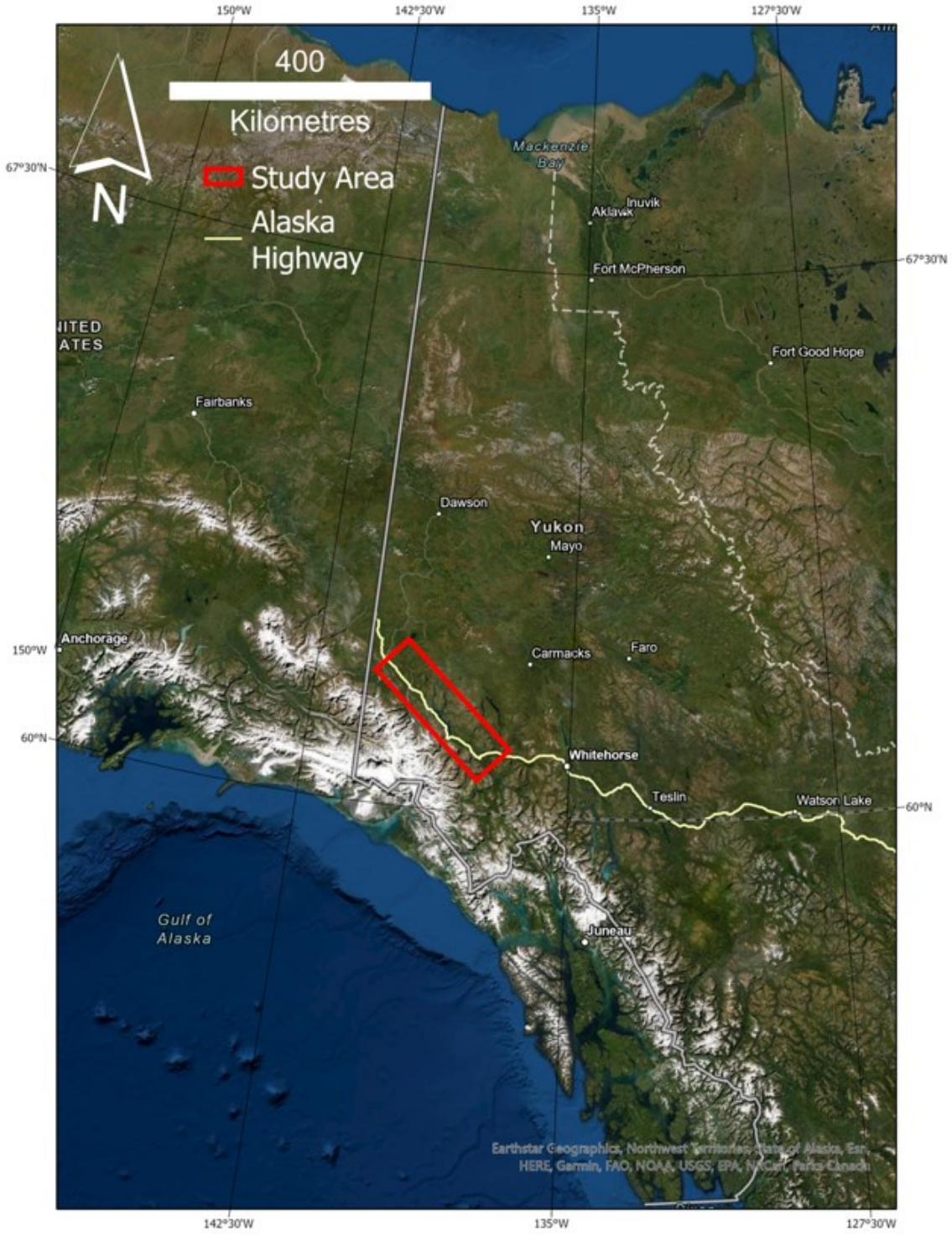

Figure 1.1. Satellite image showing the regional extent of the study area located in southwestern Yukon.

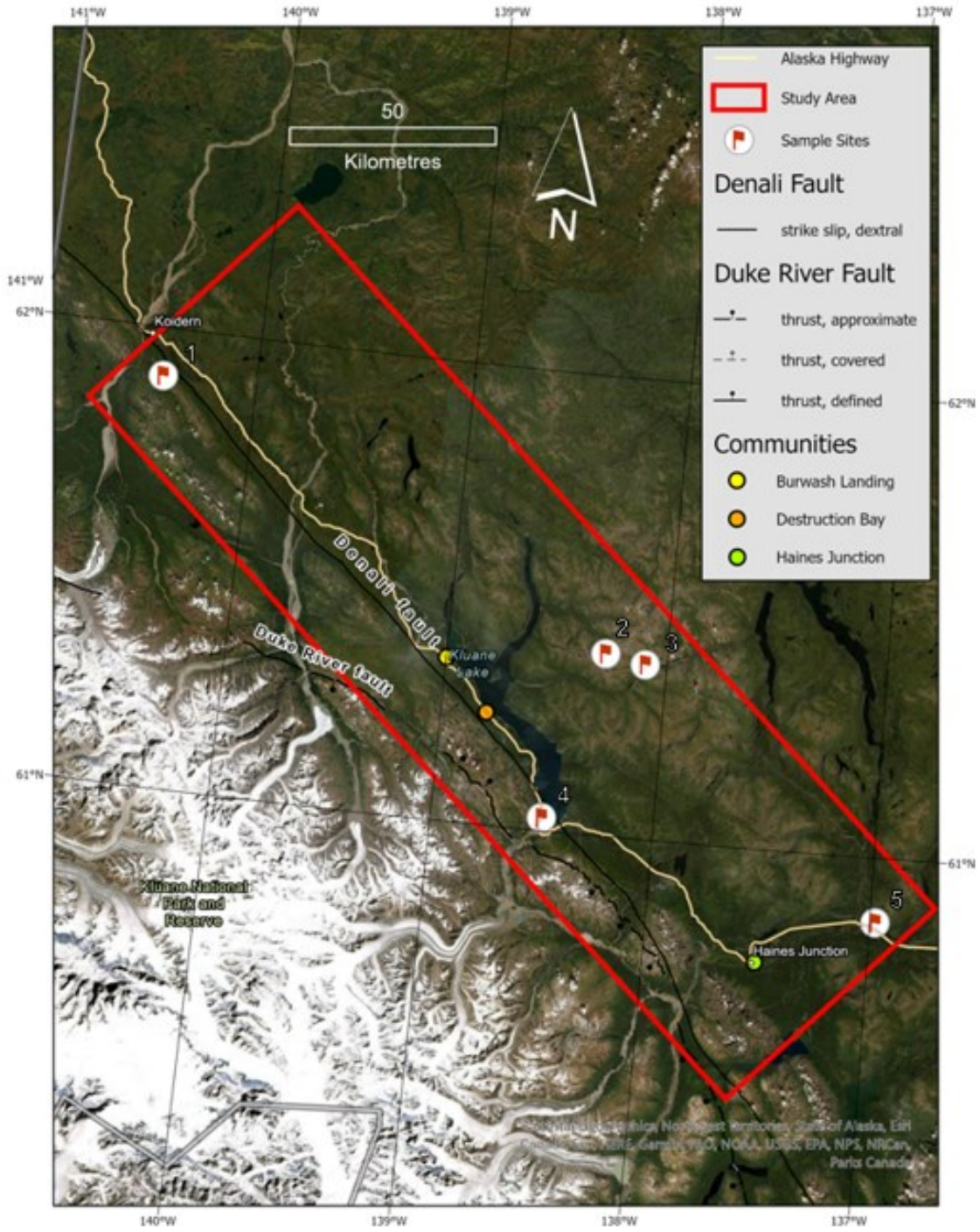

Figure 1.2. Location map of the five landslide sites examined (from north to south): (1) Generc, (2) Gladstone-1, (3) Gladstone-2, (4) Sheep Mountain, and (5) Aishihik.

1.3.2. Biophysical Setting

Situated in southwestern Yukon near the Alaska-Yukon border, Kluane Lake is located on the leeward side of the Kluane Ranges in the Shakwak Trench (Fig. 1.3). In this area, dry katabatic winds emerge from glaciers that permeate the mountain scape. The St. Elias Mountains, the highest in Canada, are a major physiographic component in the regulation of climate in the region (Wang & Geurts, 1991). To the northeast of the lake, the Ruby Range trends NW-SE towards British Columbia and Alaska and is located within the Yukon Plateau.

The study area is in the boreal zone, located north of the 60th parallel. In the Shakwak Valley region, the treeline is between 1,060 m and 1,220 m on the steep mountain slopes (Smith *et al.,* 2004). Below ~1,100 m, the study area is dominated by the subalpine spruce-willow-birch ecosystem. Southwest Yukon experienced tundra conditions from 13.6 –11.0 cal kyr BP with varying herbaceous and birch shrub assemblages, as indicated by collected pollen spectra (Bunbury & Gajewski, 2009). Around 10.2 cal kyr BP, white spruce (*Picea glauca)* became established and now remains one of the primary assemblages in the open spruce forest ecosystem (Rainville & Gajewski, 2013).

80-90% of the area (Heginbottom *et al*., 1995; Bonnaventure *et al*., 2012). This would impact sample sites such as Generc and the Gladstone sites. Lower elevation slopes, such as Aishihik and Sheep Mountain likely contain sporadic discontinuous permafrost. Permafrost thaw can contribute to the initiation of landslides due to changes in drainage patterns and soil/rock strength (Huscroft et al., 2003). In permafrost-rich zones (*i.e.* areas with continuous permafrost), such as Generc, the loss of structural support from permafrost thaw can impact internal structures, such as rock bridges within the bedrock.

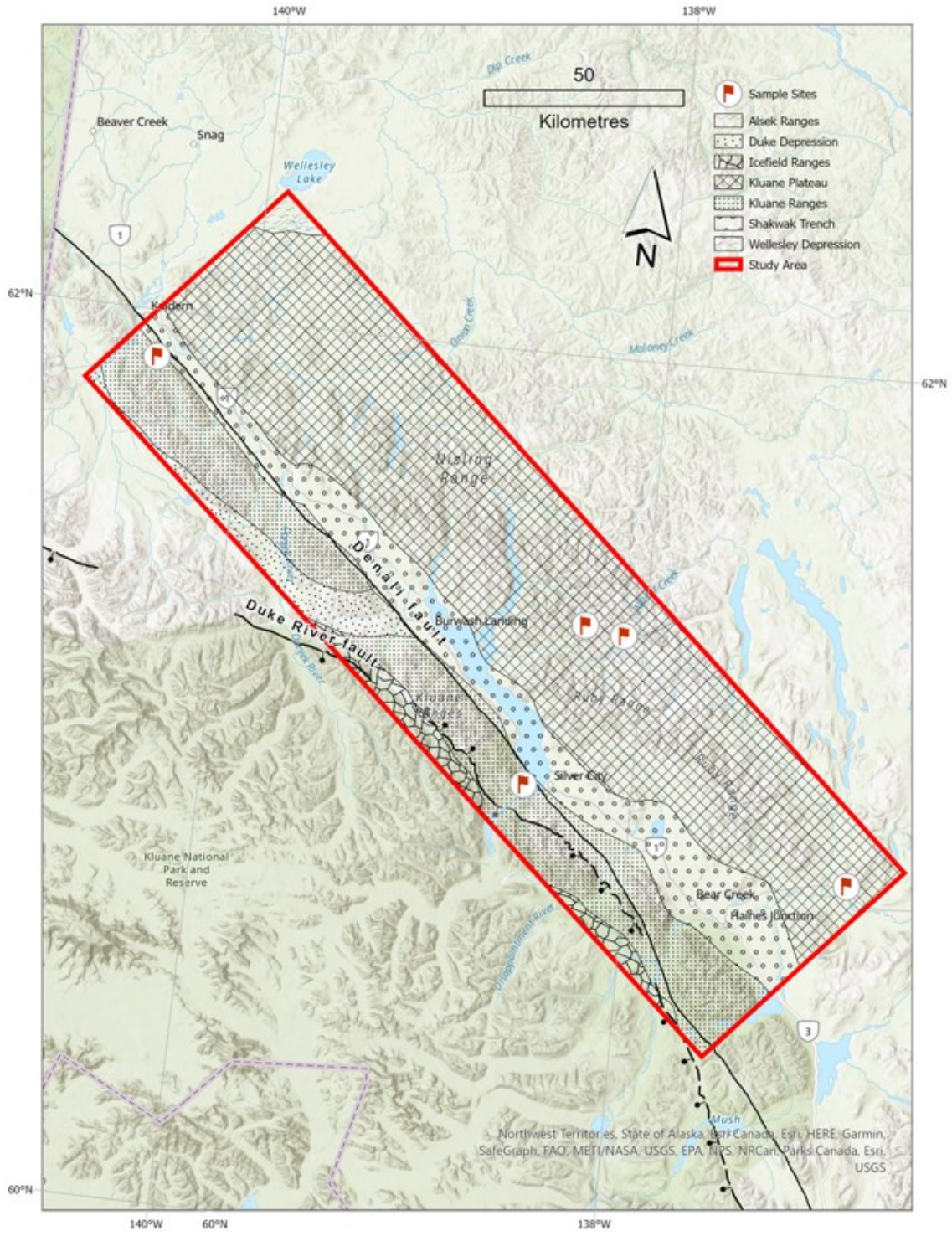

Figure 1.3. Physiographic terranes of the study area.

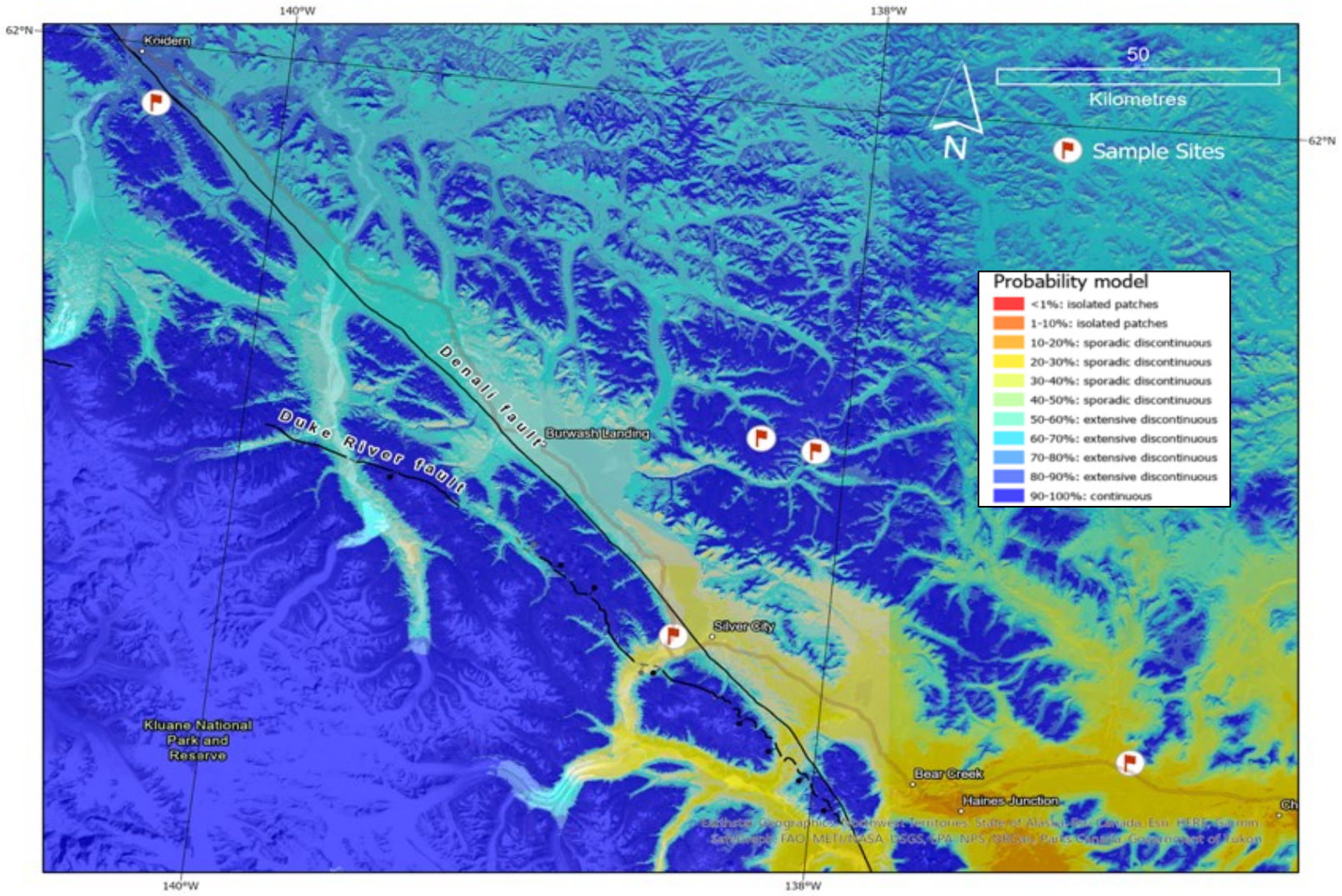

Figure 1.4. Permafrost probability model of the Kluane Lake region after Bonnaventure et al. (2012). Retrieved from Open Government Yukon.

1.3.3. Climate

The study area is located in the Upper Yukon Stikine Basin climate zone where summers tend to be warm and short while long, dark winters can get as little as four hours of daylight (Wahl et al., 1987; Environment Canada, 2022). Under the Köppen-Geiger climate classification scheme, southwest Yukon is a continental subarctic climate (Dfc) with highly variable daily and seasonal temperatures depending on latitude and elevation (Peel *et al.,* 2007). There is a significant rain shadow east of the St. Elias-Coast Mountains and precipitation varies according to topographic position and proximity to the Pacific Ocean (Wahl, 1987). The Kluane Ranges, which are visible from the highway, experience dry, cold, continental conditions due to the rain shadow effect of the adjacent St. Elias Mountains (Gajewski *et al.,* 2014). Kluane Lake is situated in the Shakwak Trench where it lies in the rain shadow of the Kluane Ranges; the valley bottom receives an average annual precipitation of 280 mm (Environment Canada, 2022; Lagerbäck Adolphi, 2014). The Ruby Ranges to the north of the trench are also contained within this rain shadow and the area experiences comparable precipitation each year, 250-300 mm (Smith *et al*., 2004). Climate normal data (1981-2010) for select weather stations can be found in Table 1.1 (Environment Canada, 2022). Station locations are found in Fig.1.5.

Table 1.1. Climate normal data from select weather stations around the study area.

Weather Station	Latitude (N)	Longitude (W)	Elevation (m a.s.l)	Mean July Temperature (°C)	Mean January Temperature (°C)	Total Yearly Precipitation (mm)
Burwash Landing	61°22’	139°03’	806.2	12.8	-22.0	279.7
Otter Falls	61°02’	137°03’	829.7	13.1	-16.4	297.3
Beaver Creek	62°22'	140°52'	649.0	14.1	-25.2	298.6

Figure 1.5. Locations of weather stations in the Kluane Lake area.

Paleoclimate Reconstructions

Paleoclimate proxies from lake sediment cores can help ascertain if climate variability contributed to pre-historic mass wasting events. Analysing modern climate conditions and comparing these data to sites where paleoclimate records are obtained helps to understand past climatic conditions.

The Burwash Landing weather station (61°22’ N, 139°03’ W, 806.20 m a.s.l.) acts as an analogue for paleoclimatic conditions in the Shakwak Trench, for example, the slopes of Sheep Mountain. This is based on the assumption that present climatic conditions may closely resemble those in the recent past. At this station, mean July and January temperatures are 12.8°C and -22.0°C, respectively, and average annual precipitation is 279.7 mm (Environment Canada, 2022).

Further east of Kluane Lake, mean July and January temperatures as recorded at the Otter Falls Station (61°02’ N, 137°03’ W, 829.70 m a.s.l) are 13.1°C and -16.4°C, respectively. Average annual precipitation at this site is 297.3 mm (Environment Canada, 2022). This station serves as an approximate analogue for the higher elevation sites such as the Gladstone sites.

Four lake sediment cores from previous studies were selected based on their relative proximity to landslide sites and modern weather stations. Lake sediment cores can provide multiple proxy records (pollen, chironomids, macrofossils), so a more comprehensive image of the paleoclimate of southwest Yukon during the Holocene can be achieved (Rainville & Gajewski, 2013).

Upper Fly Lake & Jenny Lake

Bunbury & Gajewski (2009) examined both chironomid and pollen assemblages from Upper Fly Lake (61.04ºN 138.09ºW, 1326 m a.s.l.) and Jenny Lake (61.04°N, 138.36°W, 817 m a.s.l) to infer July temperatures in the Shakwak Trench (Fig. 1.6). Conditions at Jenny Lake (Fig. 1.7) were warm between 850 and 550 yr BP then transitioned to colder conditions between ~550-100 yr BP during the Little Ice Age. A warmer regime dominated again from 100 yr BP onward (Bunbury & Gajewski, 2012). Conditions at Upper Fly Lake were cooler and drier during the Younger Dryas around 12.9 – 11.2 kyr BP (shown between the two red lines in Fig. 1.8) with warmer conditions following the Younger Dryas (11.2 kyr BP).

Comparing chironomid- and pollen-inferred July temperatures shows that over the early- to mid-Holocene there was long-term cooling. At Jenny Lake, there was also a considerable shift in chironomid assemblages around 50 yr BP which is indicative of a transition into warmer temperatures, possibly associated with the Anthropocene. In general, prior to 1150 yr BP (AD 800), temperatures in southwest Yukon were relatively cooler, but warming, whereas temperature fluctuations between 10 and 14°C were more common after 1150 yr BP.

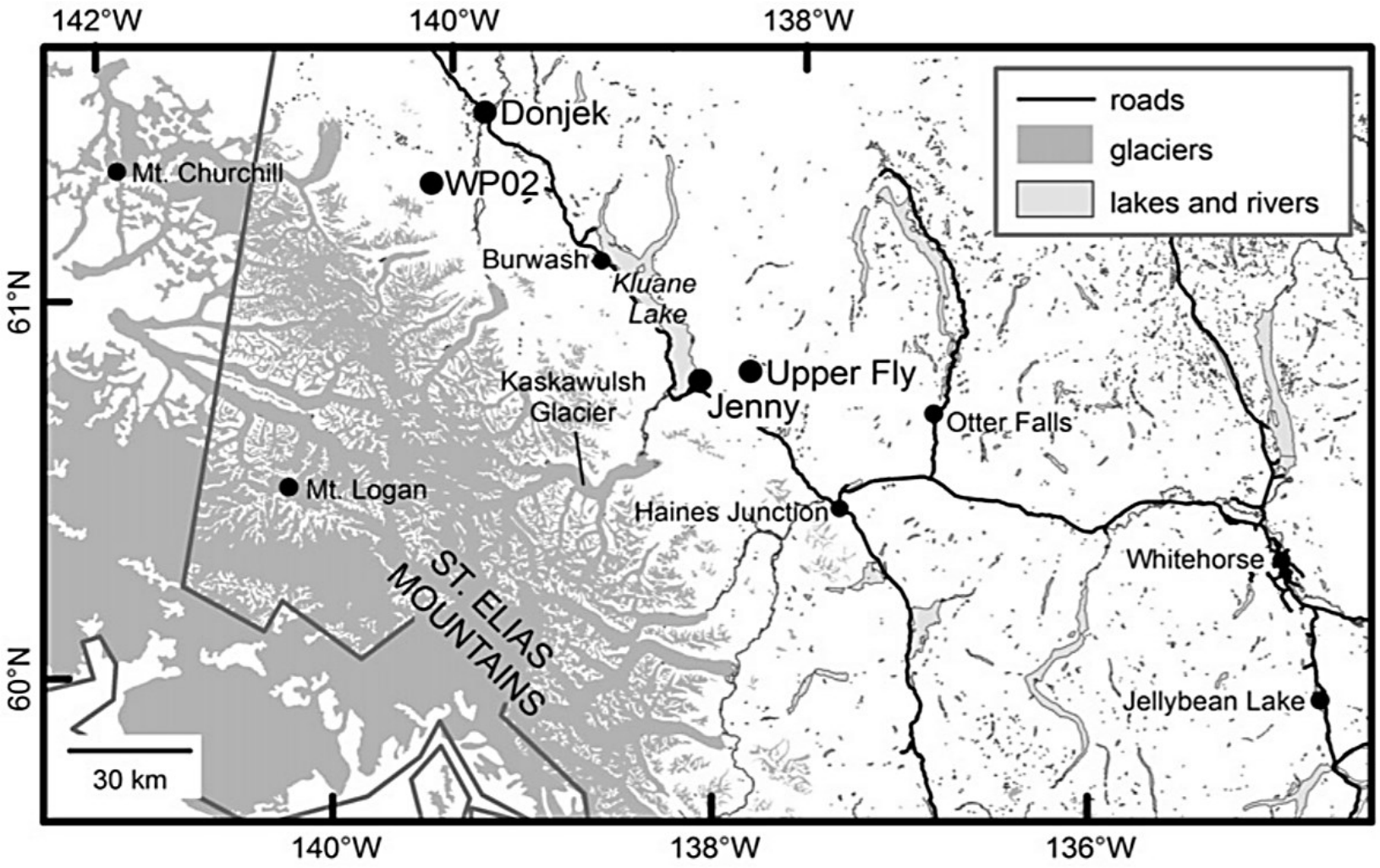

Figure 1.6. Location of two lake sediment cores used for paleoclimatic reconstructions (Upper Fly & Jenny Lake). As well as the locations of local weather stations (Otter Falls & Burwash Landing). Modified from Bunbury & Gajewski 2012.

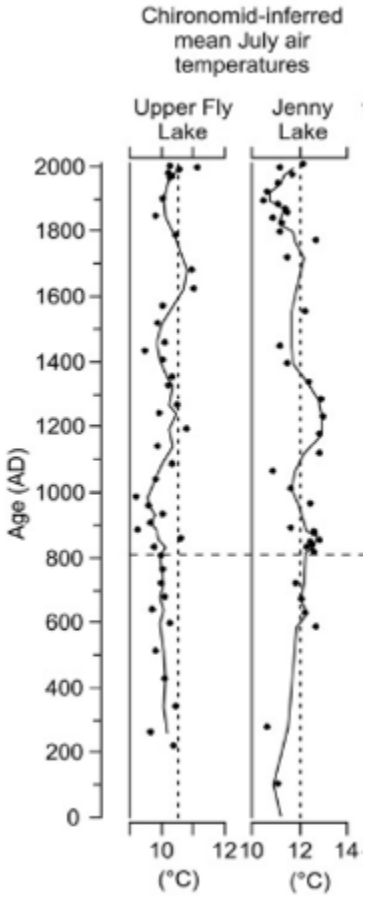

Figure 1.7. Mean July temperatures (°C) from Upper Fly and Jenny Lakes for the last 2000 years derived from Chironomid assemblages. Modified from Bunbury and Gajewski (2012).

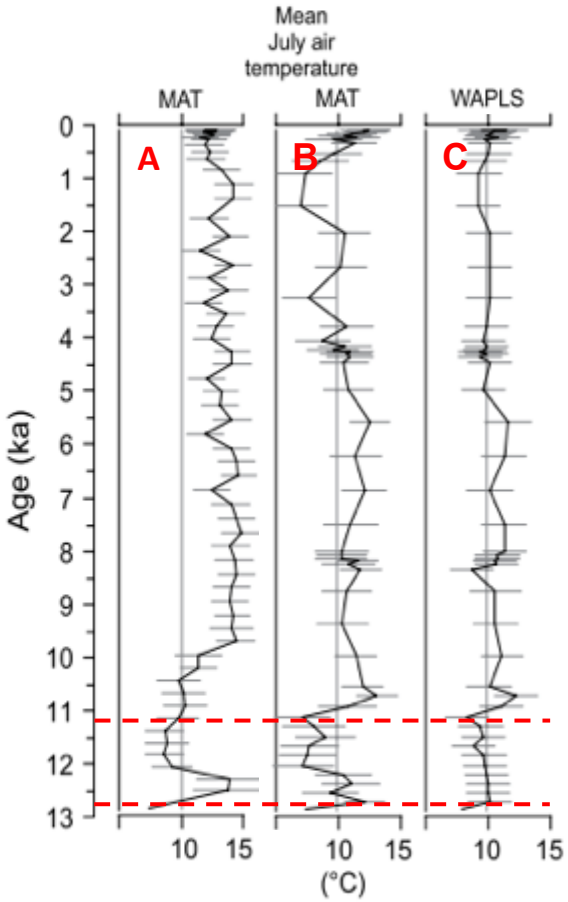

Figure 1.8. Mean July air temperatures (°C) for Upper Fly Lake. (A) Pollen-inferred temperatures using a modern analogue technique (MAT). (B) Chironomid-derived mean July air temperature using MAT. (C) Chironomid-derived mean July air temperature using a weighted average partial least squares regression (WAPLS). Red dashed lines denote the boundaries of the Younger Dryas. Modified from Bunbury & Gajewski (2009).

Moose Lake and Hudson Lake

Clegg *et al.* (2011) used midge assemblages from Moose Lake (61°37'N, 143°6'W) to infer mean July temperatures (T_{July}) in southeast Alaska (Fig. 1.9). The abrupt reversal of a warming trend from ~6000-4000 cal BP may be attributed to precessional cycles and decreased summer insolation (Clegg *et al.,* 2010). Notable T_{July} peaks of ~14.5°C occurred around 5500 and 4200 cal BP. There were also periods of climatic cooling, a decrease of up to 1°C, that were observed around 4000, 3300, 1800-1300, 600, and 250 cal BP. These trends are similar to other climatological proxy records in Alaska: The Little Ice Age, the Medieval Climate Anomaly and the First Millennial Cooling, which occurred around 1400 cal BP (Clegg *et al.,* 2010; Clegg *et al.,* 2011).

Midge assemblages from Hudson Lake (61° 54′N, 145° 40′W, 657 m a.s.l) were also used to infer mean July temperatures ranging from 11.2-12.9°C which decreased between 10,000-6,000 cal yr BP before increasing to modern values around 4000 cal yr BP (Clegg *et al.,* 2011; Figure 1.9). Both Moose and Hudson Lake display a local T_{July} minimum around 200 cal yr BP which corresponds to the timing of the Little Ice Age in the area. The inferred temperatures at Hudson Lake and Moose Lake may have been influenced by summer temperatures but assemblages may also have been affected by factors such as lake depth and terrestrial vegetation (Clegg *et al.*, 2011).

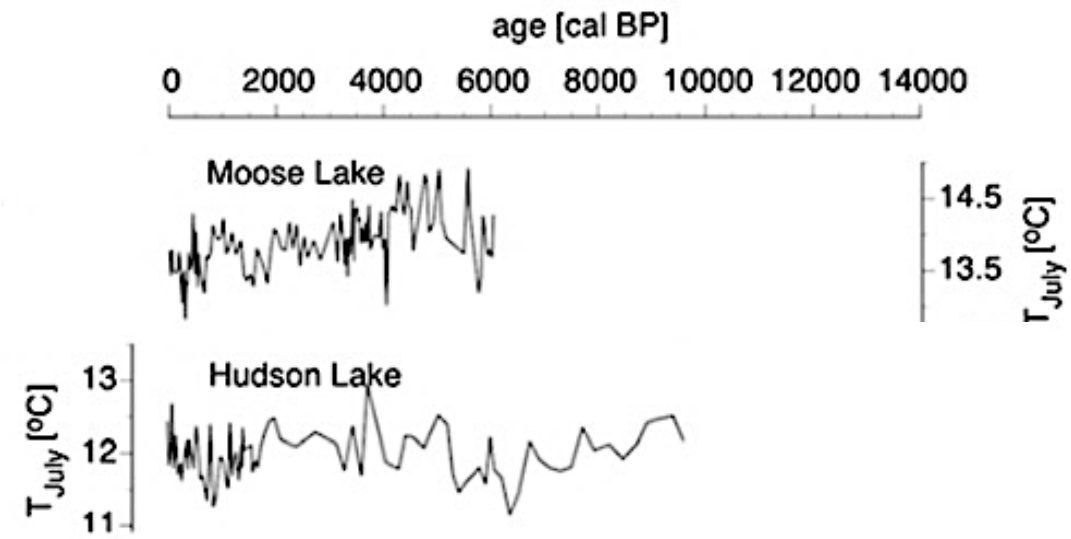

Figure 1.9. Moose and Hudson lakes records showing individual summer temperatures (°C) inferred from midge analysis. Lake sediment cores exhibit July temperatures for mid- to late-Holocene Modified from Clegg et al., 2011.

1.3.4. Glacial History

Knowing the glacial history of an area is essential to understanding the surficial geology, sediment supply, and structural conditioning of a region. It is also beneficial when sampling boulders for terrestrial cosmogenic nuclide exposure dating, to determine which samples may have experienced shielding due to glacial or glaciolacustrine activity. During the Pleistocene, glaciers in southwest Yukon initiated from the St. Elias and Coast mountains and progressed into the Shakwak Trench before extending northward into the Ruby Ranges and Yukon Plateau and coalescing to form the St. Elias Lobe of the Cordilleran Ice Sheet (Jackson *et al.,* 1991). There were several periods of glaciation in the Kluane Lake Region: the McConnell (MIS 2), Gladstone (MIS 4), Reid (MIS 6) and a number older, restricted glacial advances (Duk- Rodkin, 1999; Ward *et al.,* 2007; Fig. 1.10). Within the study area, two limits of Cordilleran Ice Sheet advances are mapped: a more extensive MIS 4 and/or MIS 6 limit and a less extensive MIS 2 limit. Older glaciations, although identified in stratigraphic section (Turner *et al.,* 2016), were not as extensive as MIS 6/4 glaciers (Fig. 1.10). Extensive upland areas in the region were never glaciated (Kennedy, 2018; Cronmiller et al., 2018; Cronmiller, 2019; Kennedy and Ellis, 2020). The last glaciation in the area, the MIS 2 McConnell Glaciation, occurred from roughly 23.9 – 10.7 ka BP (Bond, 2004).

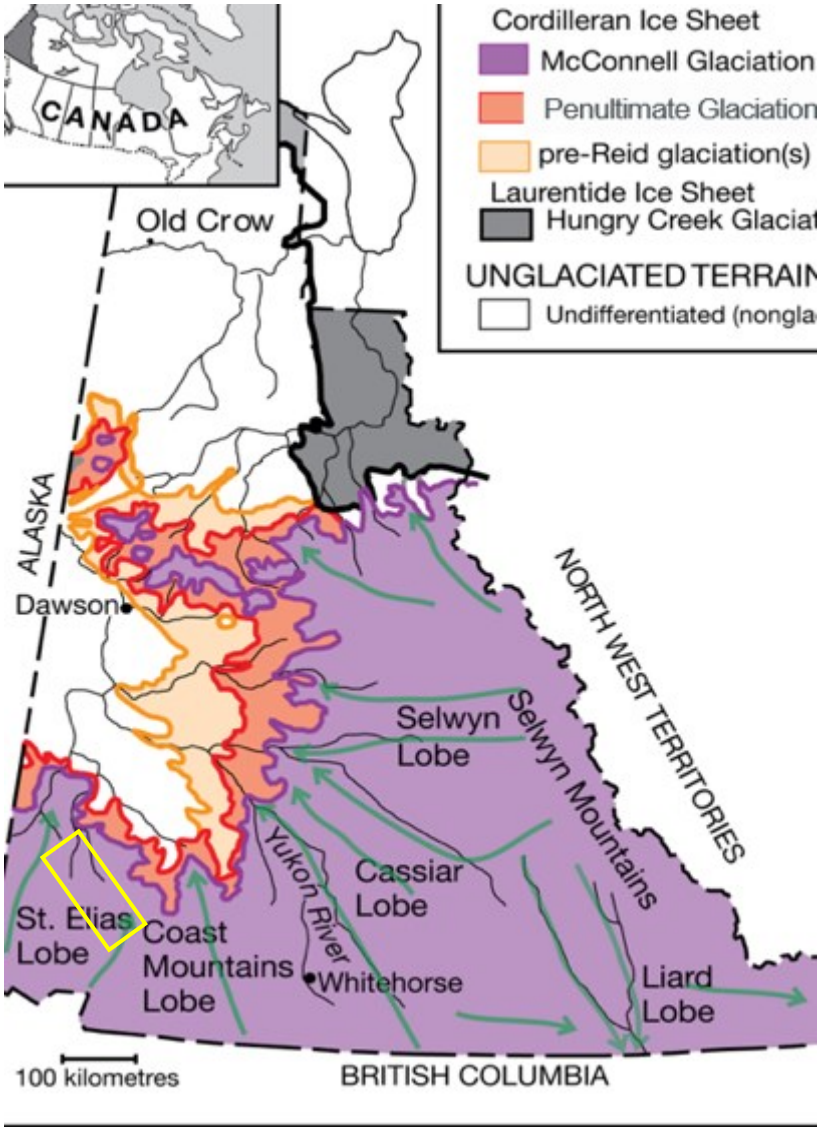

Figure 1.10. Regional glacial extents of the Pre-Reid (yellow), Reid (orange), and McConnell (purple) glaciations. Non-glaciated terrains are white. Approximate study area is marked by the yellow box. Late Wisconsinan ice flow is shown by the green arrows. Glacial limits are modified from Duk-Rodkin (1999). While not visible at this scale, some areas within the Kluane Lake region remained ice-free, for example Generc.

While glaciation was ubiquitous throughout the study area, certain areas experienced different degrees of glaciation. For example, higher elevations, such as the source area for the Generc rock avalanche, remained unglaciated and originated on a nunatak (Muller, 1966). In lower areas, such as the Shakwak Trench, glacier flutings to the northwest of the lake are indicative of large-scale glaciation (Blais-Stevens *et al.,* 2020). To the east of the lake, drumlins, fluted till, and rock drumlins have also been mapped in the valley bottom (Rampton, 1979c). Thicker glacial ice from the St.Elias Lobe would buttress slopes at lower elevations in the Shakwak Trench, such as Sheep

Mountain. East of Kluane Lake, the Aishihik rock avalanche occurred on the southern slopes of the Kluane Plateau, which also would have been influenced by valley glaciation of the St.Elias Lobe. These lower slopes would be more heavily subjected to glacial erosion and buttressing/debuttressing glacial processes. Till blankets have been mapped at mid-slope elevations in the area surrounding the Aishihik rock avalanche (Rampton & Paradis, 1982). To the north of Kluane Lake, local Ruby Range cirques in tributary valleys of the Gladstone area advanced down gradient towards the larger valley glaciers (Cronmiller, 2019). These smaller valley glaciers would have influenced areas such as Gladstone-1 (GLS-1) and Gladstone-2 (GLS-2) and would have eroded these slopes, oversteepening and conditioning them for future failure.

Deglaciation varied regionally and while the exact timing is still relatively unknown, based on ^{10}Be ages, deglaciation in the Coast Mountains and St. Elias lobes began roughly 18.2 and 17.4 ka, respectively (Ward *et al.,* unpublished). Retreat of glaciers back to source areas in the St. Elias Mountains dammed some of the major valleys with meltwater and carved out fluvial drainage channels. Glacial Lake Champagne, a lake in the Aishihik River valley, existed between 13.66 and 9.5 cal kyr BP (Hughes *et al.,* 1989; Barnes, 1997; Brideau *et al.,* 2005). The slopes adjacent to the Aishihik landslide have shorelines from Glacial Lake Champagne (Brideau *et al.,* 2005) (Fig. 1.11). Gladstone-2 landslide occurred in a meltwater corridor which formed as the Coast Mountains Lobe retreated out of the Ruby Ranges (Clague, 1981; Harris & McDermid, 1998). The study area was deglaciated around 12,500 ka, allowing cosmogenically-produced nuclides to accumulate in exposed rock and soil.

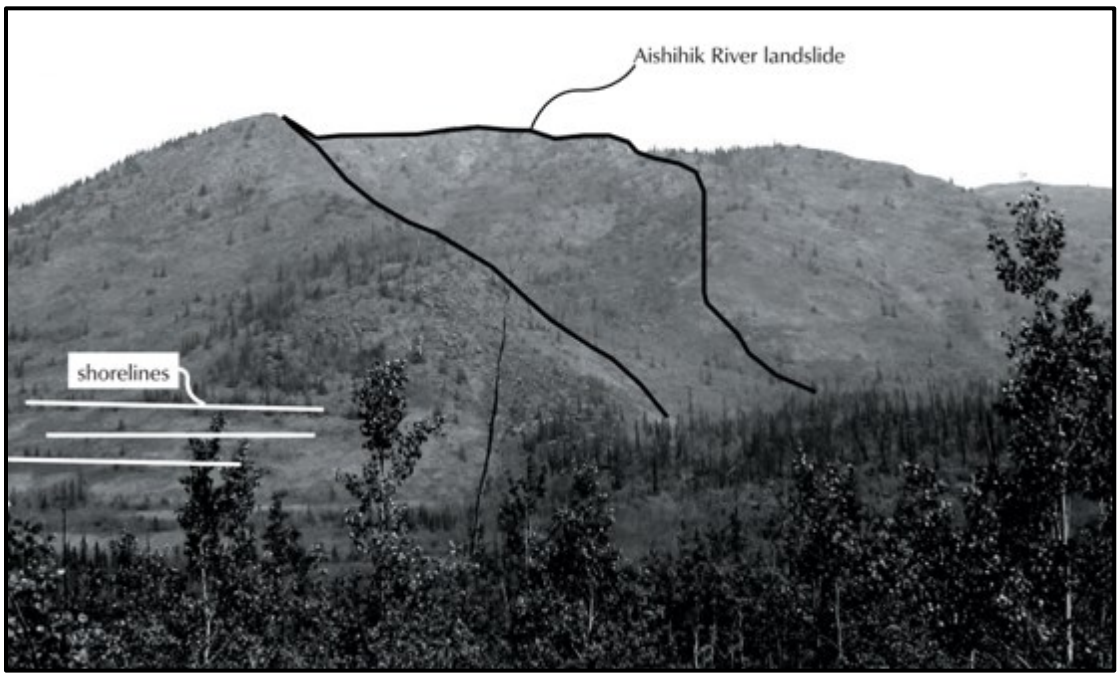

Figure 1.11. The black line traces the Aishihik landslide (looking north). Shown in white, shorelines from Glacial Lake Champagne are also depicted (Brideau et al., 2005).

Ongoing alpine glaciation during the Holocene in the Kluane Lake region exhibited local advances and retreats due to global and local climatic variability that would have further conditioned higher elevation slopes. Gilbert and Desloges (2005) proposed that local glaciers reached a maximum Holocene extent ~5.0 ka.

1.3.5. Sediment Supply

While this study primarily analyzed blocky bedrock-derived landslide deposits, sediments play a crucial role in determining the depositional setting at a site. Silty to fine-grained sand deposits are present as veneers on the boulders primarily on the Sheep Mountain landslide. These are eolian sediments (loess) that are primarily transported by katabatic winds off the nearby Kaskawulsh Glacier. These sediments may have also been supplied to the area through fluctuations in Kluane Lake or from the Little Ice Age advance of the Kaskawulsh Glacier (Reyes *et al*., 2006).

Two Plinian eruptions separated by ~500 years created two lobes of ash that extend through Alaska, Yukon, and western Northwest Territories (Fig. 1.12). The eastern lobe of the White River tephra (E) is found throughout the study area and allows relative age estimates of landslides in this study. This tephra originated from the Mt.

Churchill-Bona eruption in southeastern Alaska (1170-1097 cal yr BP; Lerbekmo *et al.*, 2008; Jensen *et al.,* 2014). Tephra thickness in the study area decreases eastward (Lerbekmo, 2008) and is only present in isolated patches.

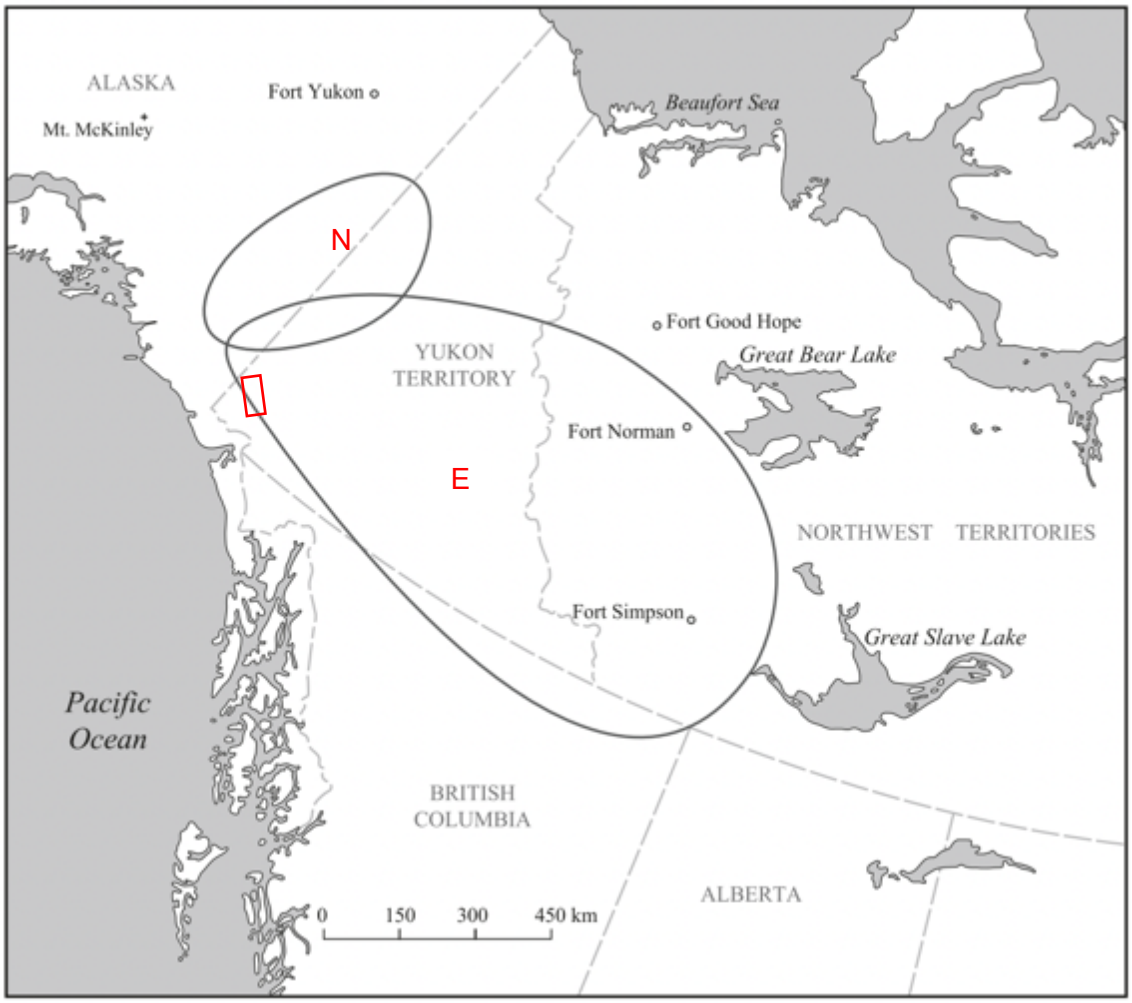

Figure 1.12. The approximate boundaries of the northern (N) and eastern (E) White River Tephra lobes. The study area is shown in the red box. Modified from Lerbekmo (2008).

1.3.6. Bedrock Geology

Kluane Lake and the Kluane Ranges fall within the Coast Belt of the Cordillera, which consists of granitic and metamorphic rocks (Roots & Hart, 2004; Fig. 1.13). Wedged between the Denali and Duke River faults, part of the study area is underlain by the Wrangellia Insular terrane which is a component of the Insular composite terrane (Israel *et al.*, 2014; Cobbett *et al.,* 2017). This terrane was accreted to the western Laurentian margin as a cohesive block around the Early to Middle Jurassic. Due to this

accretion of oceanic plateau, volcanic sequences are present (Greene *et al.*, 2004). Miocene-aged Wrangell volcanic rocks are also present, composed of basalt, andesite, volcaniclastic rocks, and tuff. They are linked to the subduction of the Pacific Plate beneath Alaska and Yukon (Israel *et al.,* 2014).

To the northeast of the Denali Fault bedrock is composed of rocks of the Yukon Tanana Terrane (Fig. 1.13). The Kluane Schist is a metamorphic package consisting of muscovite, biotite, and quartz-rich schists (Israel *et al*., 2014). It can be found to the south of the Ruby Range Batholith within the much larger Yukon Tanana Terrane (Stanley, 2012). These rocks have more quartz-rich assemblages, which can be useful for ^{10}Be exposure dating. These types of rock, however, are less prone to failure due to stronger internal structural and less faulting and jointing. The Yukon Tanana Terrane can be divided into upper and lower assemblages: a lower metasedimentary assemblage with minor volcanic rocks and an upper assemblage of arc metavolcanics that unconformably overlies it (Israel *et al.,* 2014). Unlike the Wrangellia Terrane, this assemblage of minerals was useful for ^{10}Be dating.

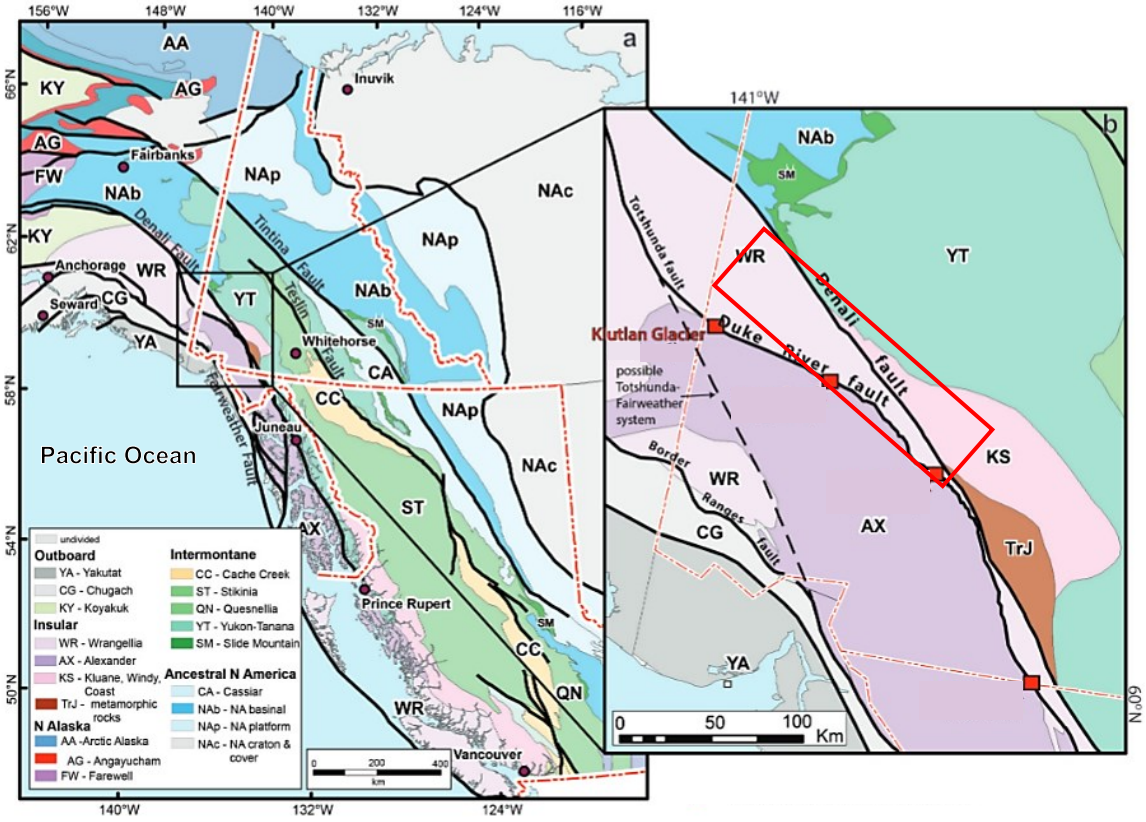

Figure 1.13. Regional terrane map of northern Cordillera. Inset shows local terranes and major faults (Denali and Duke River faults) found within the study area. The study area is shown in the red box. Modified from Cobbet et al., 2017.

1.3.7. Tectonic History

Alaska and northwestern Canada are in a highly dynamic tectonic setting as the Pacific Plate converges northward into the North American Plate (Elliott & Freymueller, 2020). Carried by the Pacific Plate, the Yakutat Block, or microplate, is accreting against the North American Plate at a rate of ~50 mm/yr in a northwestern trajectory (Christeson *et al.,* 2010; Maréchal *et al.,* 2018). The Denali Fault System was formed due to Paleozoic continental material colliding with a Late Paleozoic island-arc system (Gorum *et al.,* 2014). Seismic imagery depicting crustal structures and velocities indicate that this tectonic collision drives dextral transpression in the region (He *et al.,* 2018). There is a combination of both subduction and strike-slip mechanisms controlling the deformation of these two plates as they collide (Haeussler *et al.,* 2004; Maréchal *et al.,* 2015).

Some of this resulting strain is accommodated on the Denali Fault System and related faults in the St. Elias Mountains, such as the Duke River and Eastern Denali

faults (referred to as the Denali fault in Canadian publications) (Maréchal *et al.,* 2015; 2018). In southwestern Yukon, strain manifests prominently as displacements along strike-slip faults between the St. Elias Mountains and the Shakwak Trench, southwest of Kluane Lake (Maréchal *et al.,* 2018). In the study area, positive and negative flower structures, elongated mounds, and sag ponds are surficial expressions of the Denali Fault (Seitz *et al.,* 2008; Bender & Haeussler, 2017; Blais-Stevens *et al.,* 2020).

The Denali Fault System

The Denali Fault System is an extensive intracontinental fault network that extends southeast from Alaska, through Yukon, and into northwestern British Columbia. Extending more than 2000 km, this system combines strike-slip faulting with thrust portions that vary in intensity along segmented trunks of the fault line (Boucher & Fitch, 1969; Lanphere 1978; He *et al.,* 2018). The system includes major fault lines such as the Totschunda, the Eastern, Western, and Central Denali, the Susitna Glacier Thrust, and Duke River faults (Clague, 1979; Maréchal *et al.,* 2018). In general, the faults trend northwest-southeast in Yukon and as they continue into Alaska, they then trend northeast-southwest with secondary faults branching off along the Eastern and Central portions of the Denali fault (Clague, 1979).

Along the Denali fault, sometimes referred to as the Shakwak and/or Dalton faults (Lanphere, 1978; Clague, 1979), slip rates are lower than Alaskan counterparts (Matmon *et al,.* 2006). This decrease in slip rate indicates that part of the strain is being converted into compressional forces in parts of the Denali and Duke River fault zones. Maréchal *et al.* (2018) performed a geomorphological investigation into the Yakutat indentor and how strain is partitioned along the various faults. The researchers used satellite imagery, DEMs, and field observations in conjunction with ^{10}Be and recalibrated radiocarbon ages to calculate slip rates along the fault system. These data allowed calculation of mean vertical and horizontal slip rates at four sites along the Denali (0.9 $\pm$ 0.3 mm/yr, 0.3 ± 0.1mm/yr) and Duke River faults (3.0 $\pm$ 0.4 mm/yr, ~4.8 ± 0.3 mm/yr). They determined that these were primarily dextral strike-slip faults with areas of reverse faulting on the eastern portion of the study area. As the fault continues east towards and beyond the study area, strike-slip regimes dominate again.

Study sites closer to these active fault lines are more likely to experience fracturing due to continuous seismic activity and subsequent weakening of bedrock. This

conditioning may also exacerbate pre-existing fracture planes in source zones, thereby increasing a slope's probability of failure. This may be a factor in slopes such as Generc and Sheep Mountain that are near the Denali Fault.

Seismicity

Although the area is more extensively monitored now, prior to the 2010s, there was a distinct paucity in seismic data collected from this region. More recently, clusters of low magnitude earthquakes, the majority of which have magnitudes < 2.0 M_L, are continuously recorded around the junction between the Denali and Duke River faults, as well as the portion of the Duke River fault that spans the Kluane Ranges (He *et al.,* 2018) (Fig. 1.14). Earthquakes are more prominent southwest of the Denali fault in the St. Elias Mountains and Kluane Ranges. Towards the Kluane Plateau, seismic activity decreases drastically.

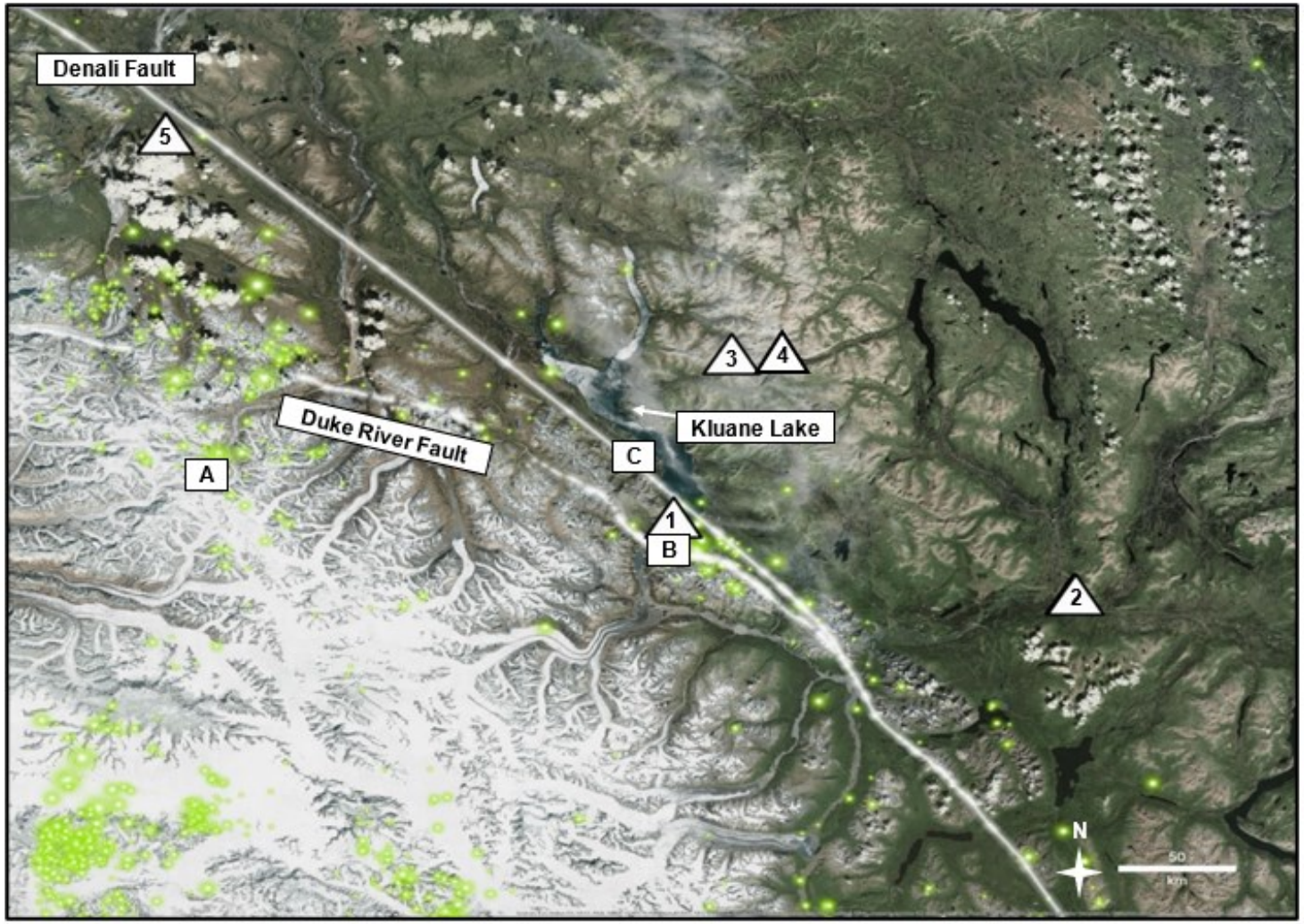

Figure 1.14. An overview of the Kluane Lake study area and with studied landslides (white triangles). 1 - Sheep Mountain; 2 - Aishihik; 3 – Gladstone-1; 4 – Gladstone-2; 5 – Generc. White boxes indicate landslides in the region that were not examined in this study but were used as a comparison. A – Mt.Steele, B – Vulcan Creek, C – Congdon Creek. The green circles indicate recent seismic activity over the last century (1963-2020) Magnitudes range from <2.0 – 6.0 M_L (Natural Resources Canada, 2019). The Eastern Denali fault, to the north, and Duke River fault, to the south, are shown by the separate white lines before they merge and progress southeastward into B.C. Imagery courtesy of ©Google Earth, ©NATO, and ©Esri.

Due to indentor tectonic kinematics, the Kluane Lake area is constantly undergoing displacements as strain is partitioned along the Denali and Duke River faults (Haeussler *et al.,* 2017). A collection of recent moment tensor diagrams (2004-2011) was examined, and their focal mechanisms were obtained from centroid moment tensor analysis (Doser, 2014). To correlate whether landslides were seismically induced or not requires a literature study of all previously documented seismic events that occurred in the study area during the Holocene.

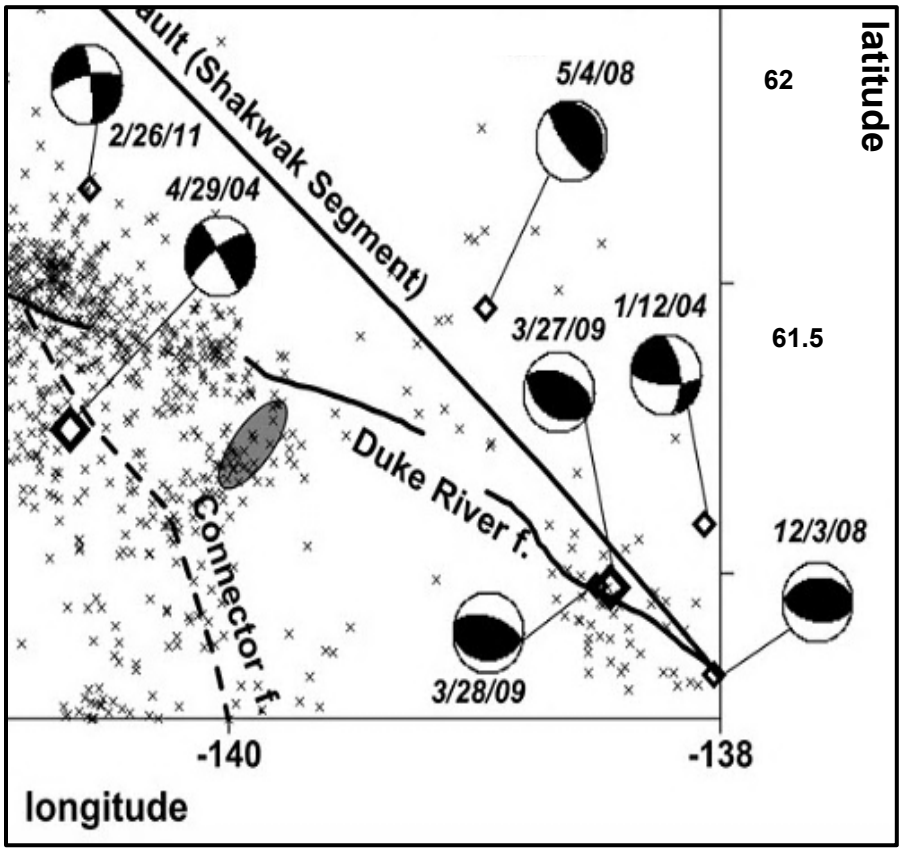

Figure 1.15. Select moment tensor diagrams around the Shakwak segment, or Denali Fault, and Duke River Fault. Crosses indicate seismicity in the area around these two active fault lines. Diamonds are events that had Mw >5. The grey oval denotes any area previously examined by Meighan et al. (2013) that displayed microseismicity. Modified from Doser, 2014.

Paleoseismicity

Landslides that cannot be correlated to historical earthquakes require paleoseismic data to identify potential co-seismic triggers. Paleoseismic data within the study area are limited but include several key studies (Doig, 1998; Seitz *et al.*, 2008; Blais-Stevens *et al.,* 2020). In a joint effort from the United States Geological Survey

(USGS) and the Yukon Geological Survey (YGS), the Denali and Duke River faults have been extensively studied due to their proximity to major infrastructure in the area (Fig. 1.16). Post glacial movement of the Denali fault system is indicated by scarps and mounds observed on Late Pleistocene and Holocene sediments (Lipovsky *et al.,* 2008). Excavations in these deformed sediments and exposure of one of the mounds along Duke River bluffs allowed dating of periods of fault movement to 300-1200, 2200, 3000, and 6000 cal yr BP (Seitz *et al.,* 2008; Blais-Stevens *et al*., 2020). Crescent Lake, a sag pond along the Denali fault, showed fluctuations in lake sediment and diatom assemblages which was interpreted to be caused by earthquake disturbances between 1900 and 1200, 6000 and 2000 years, and roughly 6500-6800 cal BP (Blais-Stevens *et al*., 2020). Chapter 3 will attempt to correlate these periods of paleoseismicity with calculated landslide ages.

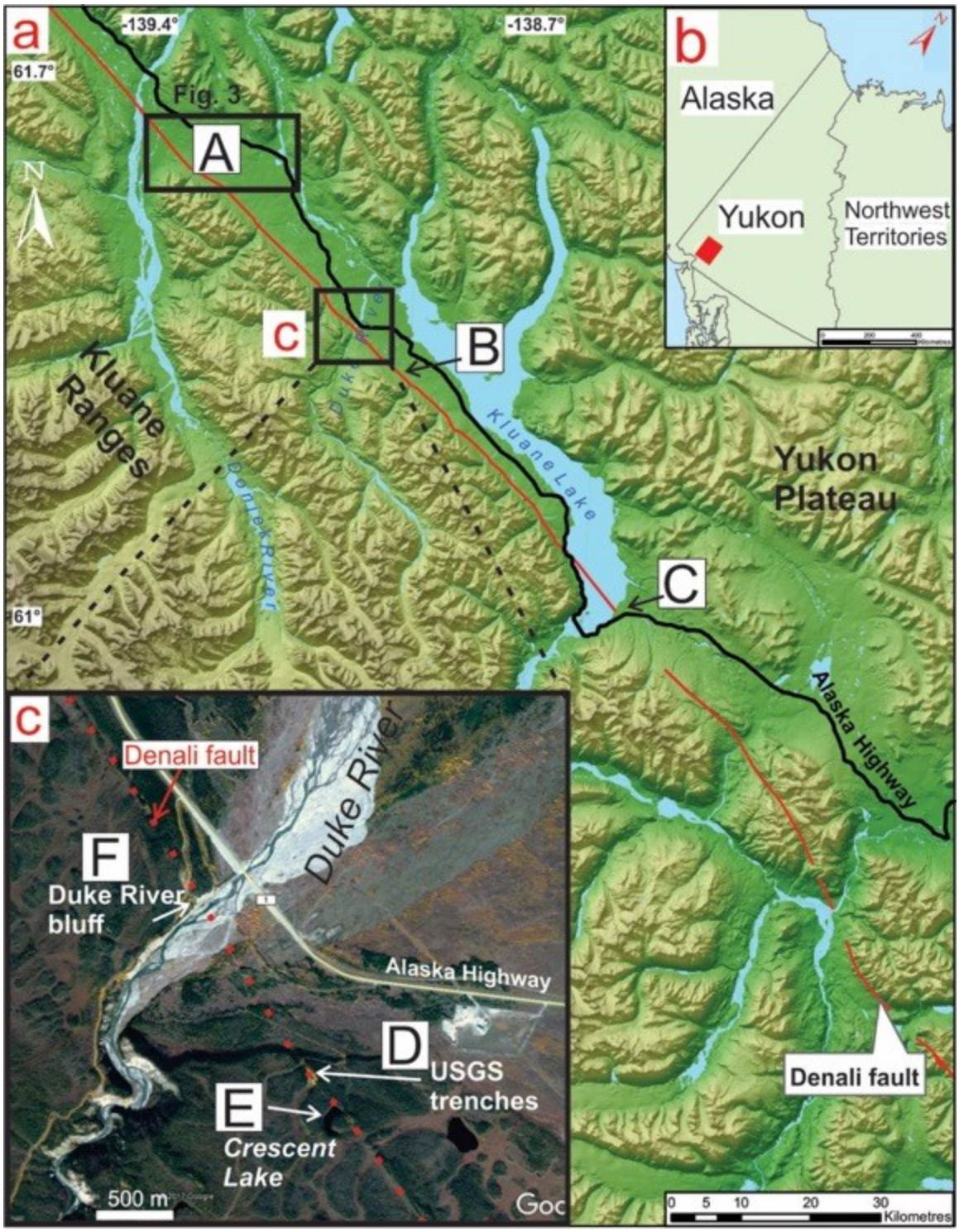

Figure 1.16. Overview of the study sites from Blais-Stevens et al.'s paleoseismic study. (a) Study sites A-C, black letters. The approximate trace of the Denali fault is shown by the red line; (b) the red rectangle shows their study area in SW Yukon, (c) Study sites D-F, which will be further explored in Chapter 3. Courtesy of Blais-Stevens et al., 2020.

1.4. Previous Landslide Work

Many rock slides are observed throughout the study area; some are well documented, such as Vulcan Creek (Brideau *et al.,* 2016, 2019) and Sheep Mountain (Clague, 1981), while others are just mapped (Rampton, 1979 a,b,c; Everard, 1994; Huscroft *et al*., 2003; Lipovksy, 2004; Blais-Stevens *et al.,* 2010). While landslides are extensive in the area, the timing, genesis, and conditioning of these hazards are largely unknown. Historical and/or well documented rock slides in the region can act as analogues to the landslides examined in this project. For example, both the Congdon Creek (Box “C”, Fig. 1.14) and Vulcan Creek (Box “B”, Fig. 1.14) landslides occurred in a similar geologic setting as the Generc and Sheep Mountain landslides and may have been conditioned by similar mechanisms. The timing of the Mt. Steele rock and ice avalanche occurred roughly between those of the Generc and Sheep Mountain landslides in the St. Elias Mountains and may also serve as an analogue (Box “A”, Fig 1.14).

1.4.2. Vulcan Creek Landslide

This historical landslide was studied by Brideau *et al.* (2016, 2019) and is a presumed re-activation of a relict failure along the west-facing slopes of Vulcan Creek near its confluence with Jessie Creek. It is ~5 km from the southern tip of Kluane Lake and occurred between August 15 and September 9, 2014. This estimated 800,000-1,300,000 m^3 landslide blocked Vulcan Creek forming a lake. Precursor slope deformation was observed in 2003 and 2013 satellite imagery. The landslide travelled ~1.2 km from the head scarp at 355 m in elevation above the distal end of the deposit. Situated between the Wrangell and Alexander terranes, this landslide occurred near the Duke River fault trace; fine-grained sedimentary anhydrite and intrusive mafics were observed both in the head scarp as well as within the boulder field. Clasts observed are grey and schistosic, reddish brown and volcanic (Donjek fm) and till was also present. A seismic trigger was assumed at this site due to the proximity of Duke River fault. A query of the USGS and NRCan catalogues of earthquakes that occurred between April – October 2014 and were within 100 km of the failure were deemed unlikely to have triggered the event based on Keefer’s (1984) empirically-derived relationship between earthquake magnitude and the distance at which a landslide can be initiated. The

proximity to the fault likely resulted in a large amount of rock deformation. This, combined with warmer conditions (~10°C warmer) and higher than normal precipitation levels (approximately twice as high) recorded at the Burwash Landing weather station during January and July 2014 likely contributed to this landslide. A trigger, however, was not determined in this study; highlighting the fact that even though a slope may have several conditioning factors, an exact trigger may not be ascertained.

1.4.3. Mt. Steele Rock and Ice Landslide

The Mt. Steele landslide occurred in July 2007 in the St. Elias Mountains between the Generc and Sheep Mountain landslides (Lipovsky *et al.,* 2008; Brideau *et al.,* 2009) (Fig. 1.17). The failure was on the north-facing side of the mountain, at the intersection between the NNE-and NNW-facing walls and extended ~5.75 km onto the Steele Glacier, descending 2,160 m. The source of the failure is believed to be from the Late Miocene Wrangell Suite (granodiorite, diorite, and gabbro) (Dodds & Campbell, 1992). This large rock slide was well documented by glaciologists, park wardens and seismographs. It happened in several sequences over the course of a few days, and like the Vulcan Creek landslide, both seismic and climatic triggers were ruled out. Sixteen earthquakes had been documented between July 1-24 within 300 km of Mt. Steele, but none occurred in the days leading up to the event (Lipovsky *et al.,* 2008). Based on daily average temperatures from Burwash Landing, temperatures were 2.7°C above the normal (1971-2000 July temperatures) at least 10 days before the event; for the month of July, temperatures were 0.6°C higher than normal. These temperatures were concluded to not be anomalous for the area. A fine-textured red-brown debris found within the zone of deposition suggested that the source materials originated from a local fault zone. The debris was also highly sheared and had low rock mass strength which also suggests that overall bedrock integrity was decreased. Brideau *et al.* (2009) suggested that the failure initiated as an ice avalanche that then plucked and entrained the weakened bedrock material. Like Vulcan Creek, historical events like Mt. Steele provide insight into pre-historic landslides in the region.

Figure 1.17. Oblique view of the Mt.Steele rock slide (Photo credit: P. von Gaza; Lipovsky et al., 2008).

1.4.4. Congdon Creek Rock Avalanche

The Congdon Creek rock avalanche is a large failure along the southern portion of Kluane Lake. It is on the northeast flank of the Kluane Ranges and is roughly 15 km away from the Sheep Mountain rock slide (Figs. 1.18, 1.19). It is not a historical event so

its age is uncertain. It is close to the Sheep Mountain site which means it may have experienced similar conditioning mechanisms (climate and proximity to active faults).

The rock avalanche has an approximate volume of 70 x 10^6 m^3 (Thurber Consultants, 1989). Lidar imagery shows the extent of the event (Fig. 1.18). The source area is likely a concave scar on the northern slopes of the Kluane Ranges between 1150 and 1600 m in elevation (Everard, 1994). Modern fan outwash is found adjacent to and lower than the landslide deposit. The surface of the landslide deposit is pockmarked by pits which were proposed to have formed by the ablation of entrained ice (Everard, 1994). Hummocky debris and contorted debris ridges are also observed scattered over the deposit.

This landslide was deemed not eligible for exposure dating during my 2019 field season (Fig. 1.19). The deposit was covered by a coniferous forest as well as a thick, silty loess deposit. Datable materials underneath the leading edge of the landslide were not observed due to permafrost cover and no accessible exposures. The northwestern ridge of the toe of the deposit was traversed and boulders were encountered sporadically along the ridge. The boulders on the deposit appeared to be mafic in origin and were not selected for TCN analysis due to severe weathering and loess cover (Fig. 1.19 A,B). Perhaps with significant machine-assisted excavation, datable material can be retrieved underneath the leading edge of the deposit.

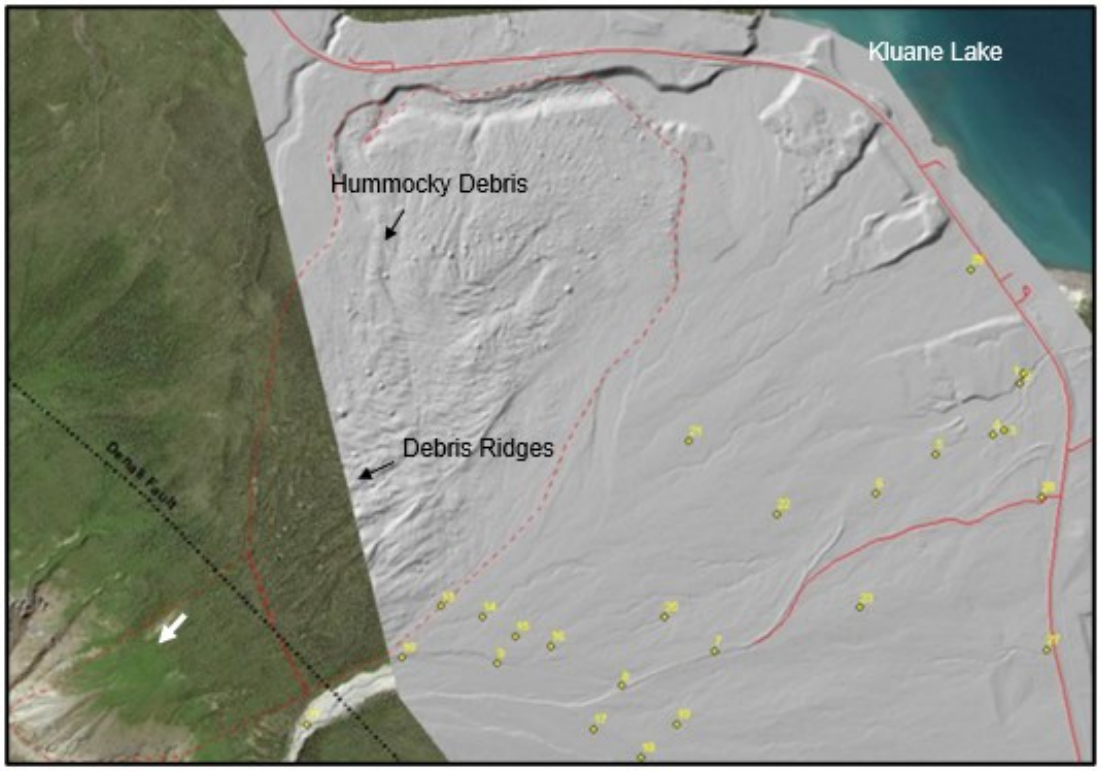

Figure 1.18. The Congdon Creek fan. Lidar imagery provided by the YGS showing the alluvial fan at Congdon Creek. Rock avalanche deposits can be seen to the northwest and are outlined by the dashed red line. Yellow dots represent sample sites in Koch et al's 2014 study. The suspected source area is indicated by the white arrow and the Denali Fault can be seen to the south of the deposits (black dashed line) (Modified from Koch et al., 2014).

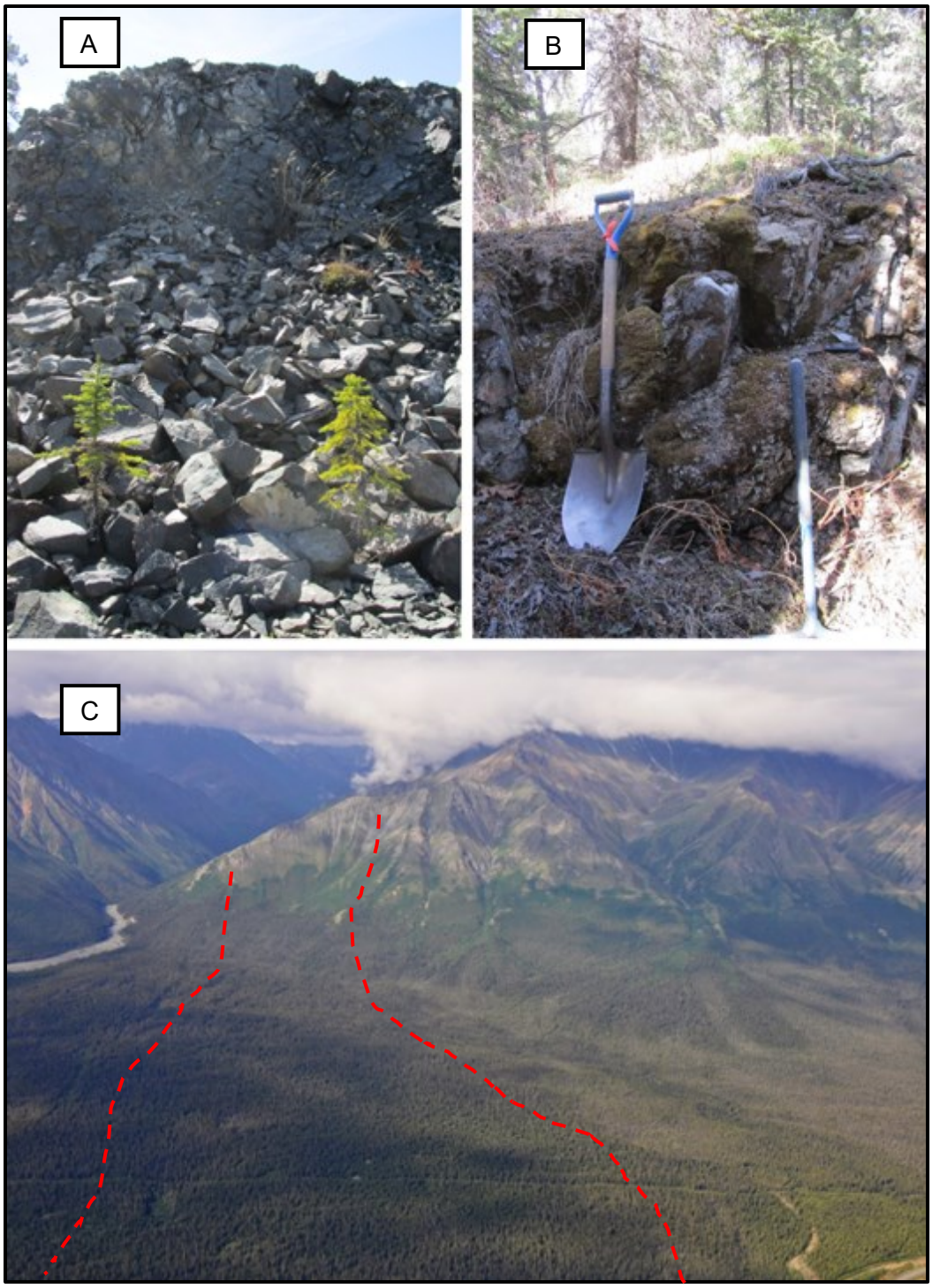

Figure 1.19. Congdon Creek as observed during the 2019 field season. (A) Blocky debris from the Congdon Creek rock avalanche. This disaggregated block was roughly 6 m tall and makes up part of the landslide's hummocky deposits. (B) Disaggregated boulder near the toe of the deposit that was covered by the loess and moss. This site was not dated by TCN due to excessive shielding by loess and vegetation which made TCN dating problematic. No suitable dateable radiocarbon materials were found. Shown above is a disaggregated boulder seen near the toe of the deposit that was covered by the loess and moss. Shovel is ~120 cm. (C) The Congdon Creek alluvial fan and avalanche deposit as viewed from a helicopter, looking south. The red line denotes the approximate outline of the rock avalanche deposits.

1.5. Landslide Background

This section is an introduction to the landslides examined in this thesis including imagery examined, site overview, geological background, and previous knowledge. A more detailed analysis of exposures is presented in Chapter 3. Sheep Mountain and Generc landslides are in the Kluane Ranges, while Gladstone-1, Gladstone-2 and Aishihik landslides are located on the Yukon Plateau. Landslides were selected based on their potential suitability for Quaternary dating methods such as terrestrial cosmogenic nuclide (TCN) exposure dating, their accessibility, large volume, and their proximity to the Denali fault.

1.5.2. Sheep Mountain Rock Avalanche

The Sheep Mountain landslide (61.03° N, -138.50° W) is located on the southwest margin of Kluane Lake (Fig. 1.20) and was previously investigated by Clague (1981) and Koch *et al.,* (2014). It is the closest landslide to the Denali fault (~3 km to the north). The source area is between 1200 and 1550 m in elevation on a northeast facing flank of a spur ridge.

Two exposures were examined at this site: Northern Roadcut (61.04°, -138.50°) and Soldier's Pass (61.03°, -138.51°) (Figs. 1.21, 1.22 respectively). These sites were selected based on their potential for bracketing the stratigraphy of the rock avalanche deposit: the Northern Roadcut exposes units below the rock avalanche, while Soldier's Pass exposes materials overlying the rock avalanche.

Figure 1.20. The Sheep Mountain rock avalanche. The Alaska Highway bisects the deposit and Kluane Lake is shown to the east. Locations of the Northern Roadcut (NRC) and Soldier's Pass (SP) exposures are shown.

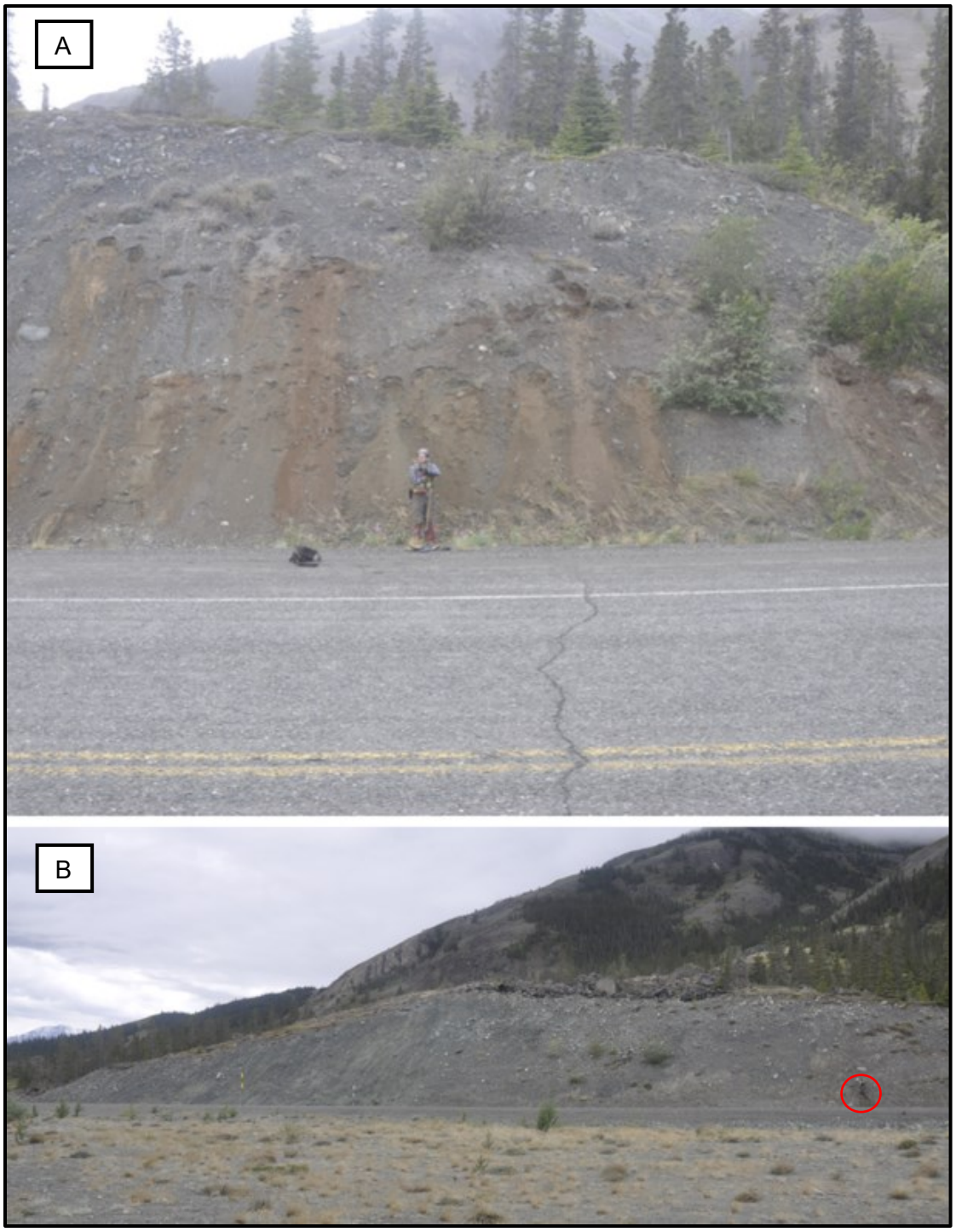

Figure 1.21. The Northern Roadcut exposure. (A) Beds underlying the landslide deposit were examined for their radiocarbon potential. The Alaska Highway is in the foreground (B) The full extent of the roadcut, person for scale (red circle).

Figure 1.22. The Soldier's Pass exposure. (A) The exposure prior to excavation. (B,C) Organic layers were observed immediately overlying blockier material and were sampled for radiocarbon dating. Scraper is ~20 cm long. (D) The exposure is roughly 2 m tall.

The rock avalanche occurred within the Nikolai (uTrN2) and Chitistone (uTrC) formations on the southern edge of Kluane Lake, near the Slim's River delta (Fig. 1.23). The Nikolai formation is Upper Triassic amygdaloidal basaltic and andesitic flows, approximately 229–204 Ma old (Greene *et al.,* 2009). The Chitistone formation is composed of argillaceous limestone and dark grey argillite, 229-204 Ma old. Blocks found in the debris field originated from these metavolcanic assemblages and included metabasaltic and meta-andesitic blocks.

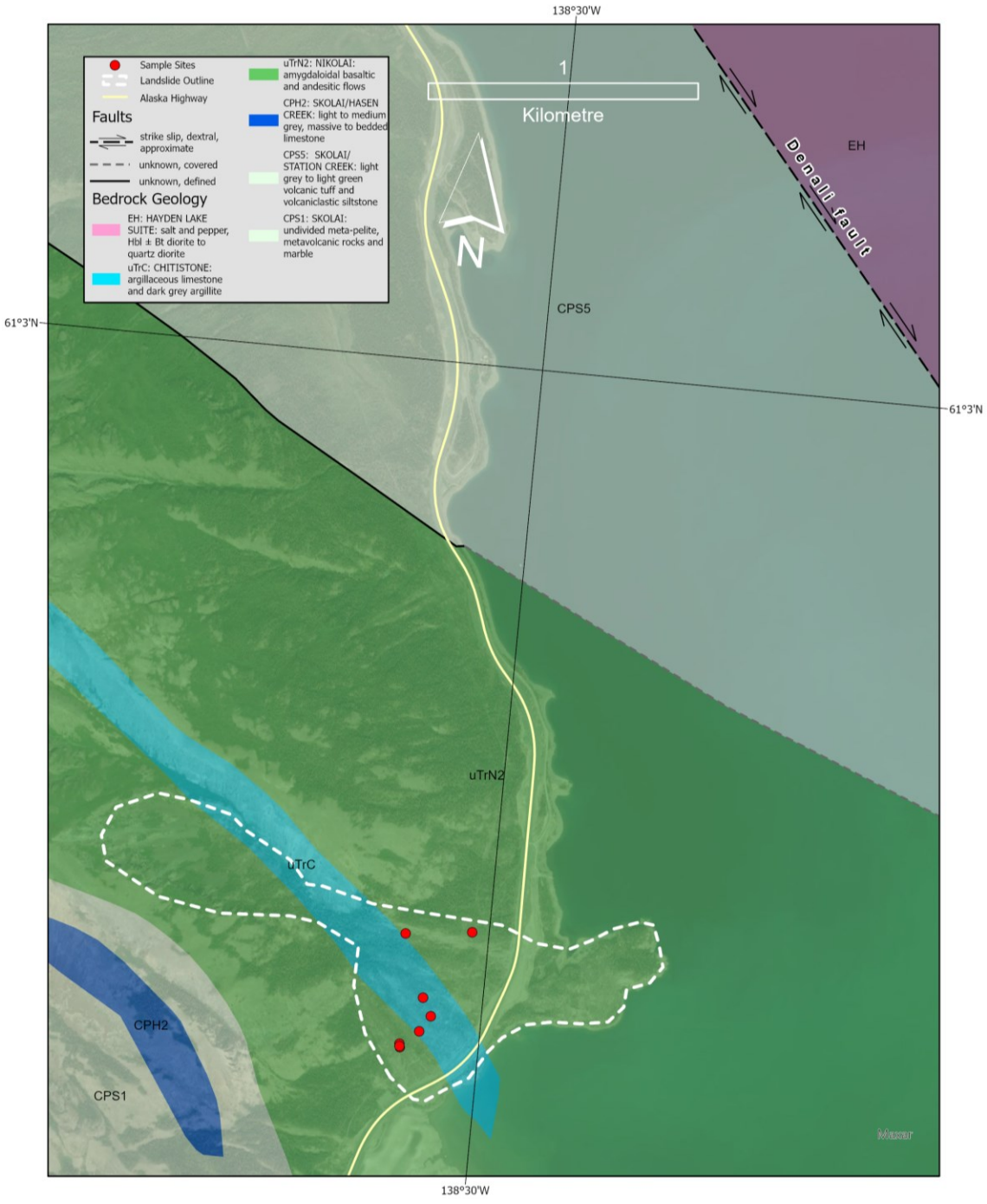

Figure 1.23. Local bedrock geology around the Sheep Mountain rock avalanche (YGS, 2022).

Clague (1981) proposed that the Sheep Mountain rock avalanche occurred in two phases. To determine the ages of these phases, wood from a buried forest bed underlying the landslide deposit and a pith sample from a dead stump rooted on top of the landslide were radiocarbon dated to 1950 ± 50 yr BP and 490 ± 50 yr BP. White

River tephra was observed in the immediate vicinity of the deposit in eolian sands overlying landslide debris which was presumed to be the lower landslide deposit. However, White River tephra was not found overlying the upper deposit. With this additional constraint, the two phases of the deposit were presumed to be between 1950 – 1200 ^{14}C yr, and 1200-500 ^{14}C yr. Underlying debris flow deposits were noted during Clague's initial study and were further investigated by Koch *et al.* (2014). In this study, three debris flow deposits were observed in the Northern Roadcut exposure underlying the rock avalanche deposit. The lowermost unit was described as a clast-supported diamicton with sub-angular to sub-rounded clasts that reached up to 1 m in diameter. The middle debris flow unit was comparable but had more sub-rounded clasts. Finally, the uppermost debris flow unit also consisted of a clast-supported diamicton. These units were separated by thin soil layers which contained dateable wood debris, branches, and potentially *in situ* roots. Radiocarbon dating these organics from bottom to top yielded ages of 2,025 ± 20 ^{14}C years BP (1995–1950 cal yr BP) between units 1 and 2, 1,910 ± 20 ^{14}C years BP (1881 – 1742 cal yr BP; AD 70 –125) between units 2 and 3, and 1,920 ± 20 ^{14}C years BP (1918 – 1744 cal yr BP; AD 60–125) between the uppermost debris flow unit and the rock avalanche deposit. In this project, radiocarbon samples were collected from the previously investigated Northern Roadcut and the newly discovered exposure, termed the Soldier's Pass exposure. Additionally, TCN samples were collected across the surface of the deposit to supplement the radiocarbon data.

1.5.3. Generc Rock Slide

This site is located on the SSW-facing slopes of the Kluane Ranges near White River (61.89° N, -140.45° W; Fig. 1.24). A previous failure at this site was mapped by Rampton (1979c). This site is the furthest west in the study area and is ~6 km south of the Denali fault. This landslide has not been previously investigated and provides a novel opportunity for dating.

This landslide terminates into Hazel Creek where modern fluvial channels bisect the deposit. The head scarp is roughly 640 m up the steep valley wall near the summit of the range (~1,500 m a.s.l.) and the deposit covers approximately 0.26 km^2 of the valley bottom. The deposit terminates roughly 260 m away from the base of the slope.

The landslide initiated in the Station Creek Formation which is composed of volcanic tuff and volcaniclastic siltstones approximately 359 to 299 Ma old (Israel *et al.,* 2007) (Fig. 1.25). The zone of propagation displays scours into the Hasen Creek Fm which consists of dark grey and brown-weathered siltstone, mudstone and sandstone (Israel *et al.,* 2007). This site was studied due to its proximity to the fault as well as the presence of what appeared to be large bedrock blocks in the landslide debris (Fig. 1.26 A,B). Field investigations later determined the mounds to be molards. While molards can occur without the presence of ice or permafrost (Cassie *et al.,* 1988), due to the high probability of extensive discontinuous to continuous permafrost at this site, it is presumed that the landslide mobilized ice-rich sediments (*cf.* Morino *et al.,* 2019) (Fig. 1.26 D).

Due to the relative “freshness” of the deposit and the presence of rafted trees (Fig. 1.26 C), the site was found to be too young for TCN dating. However, the presence of tilted and scarred conifers around the leading edge of the landslide deposit proved viable for dendrochronology.

Figure 1.24. Generc Landslide. The debris in the valley bottom is outlined by the white dashed line. The head scarp and trace of propagation are clearly visible and distinguished by the lighter brown tone. ©GoogleEarth, 2019.

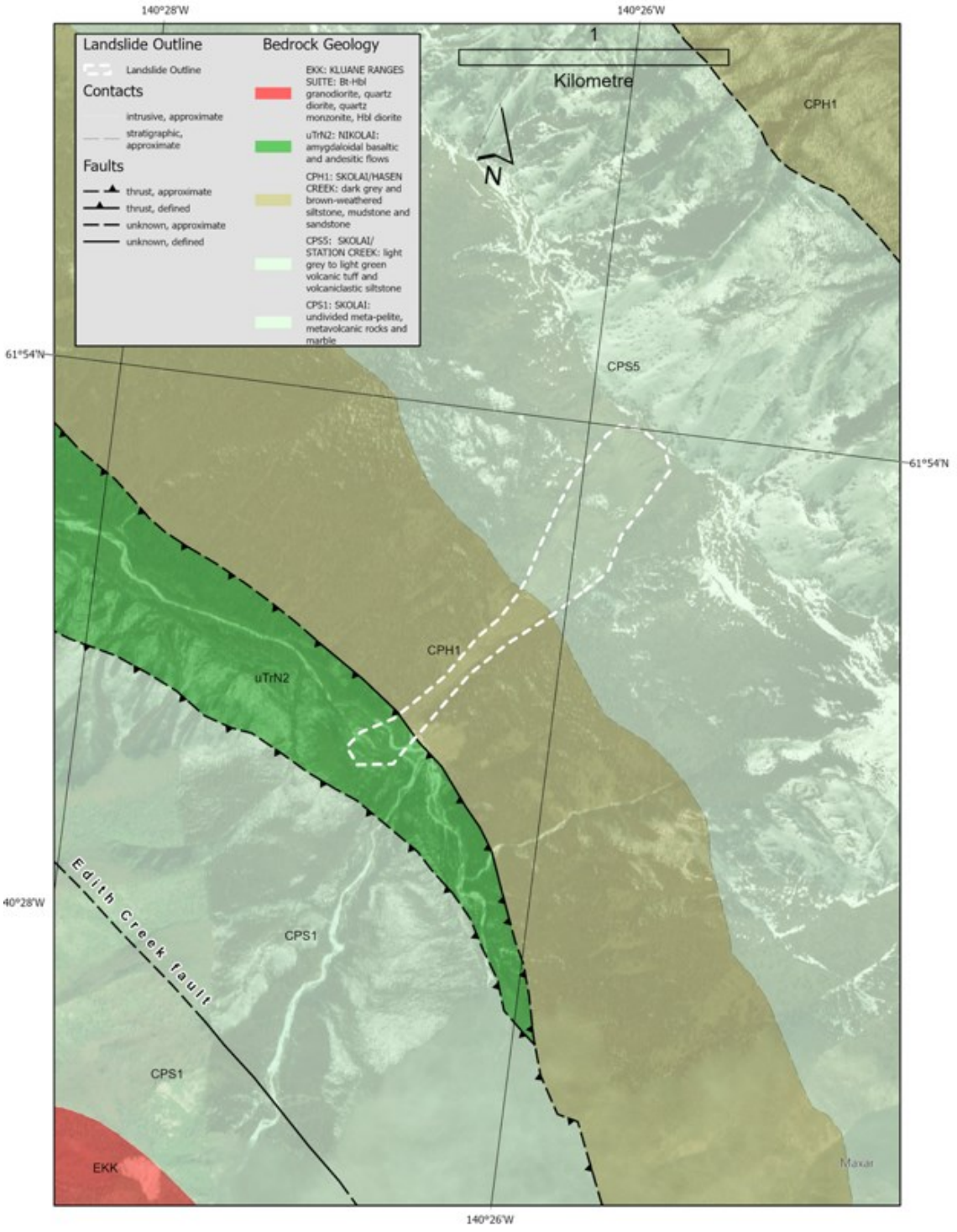

Figure 1.25. Bedrock geology at the Generc site (YGS, 2022)

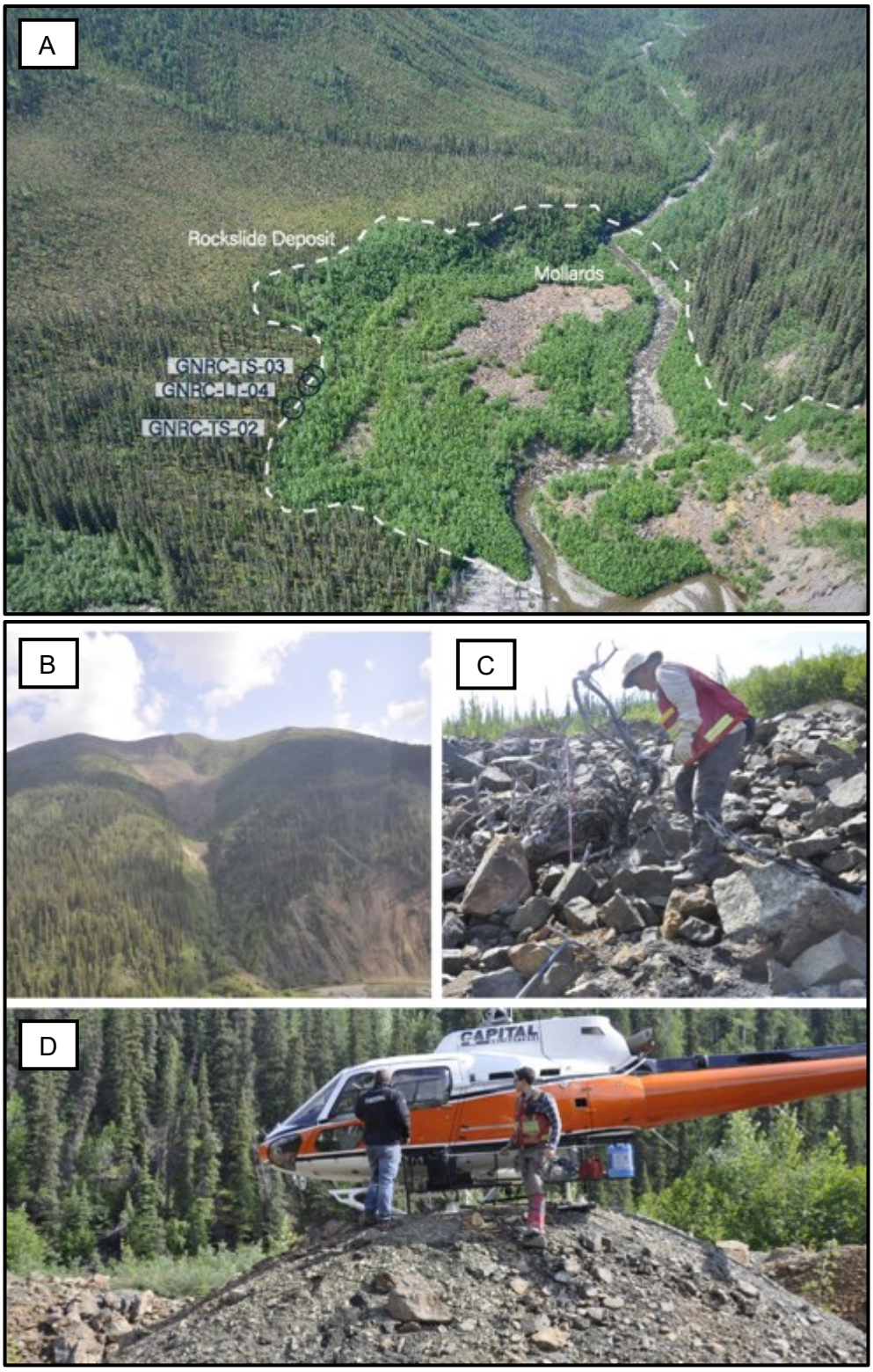

Figure 1.26. The Generc landslide. (A) Outline of the deposit with dendrochronological samples indicated. (B) Aerial imagery of the head scarp of this event. (C) Rafted trees present on the landslide. (D) An example of one of the molards, which was approximately 7 m across, 2 m tall.

1.5.4. Aishihik Rock Avalanche

The Aishihik rock avalanche (60.86° N, -136.97° W) is roughly 1 km north of the Alaska Highway and is located within the Yukon Plateau (Figs. 1.27, 1.28, 1.29, 1.30). This site was previously studied by Huscroft *et al.* (2004) and Brideau *et al.* (2005) due to its proximity to the major transportation corridor. Three dominant discontinuity sets and twenty-five tension cracks within the head scarp (roughly 500 m above the base of the deposit), as well as pre-existing tectonic conditions that reduced rock mass quality in the head scarp were determined to be the primary conditioning mechanisms (Fig. 1.28 A,B) (Brideau *et al.,* 2005). Huscroft *et al.* (2004) postulated that the failure may have also been conditioned due to the thinning and recession of a Late Wisconsinan glacier in the Dezadeash Valley.

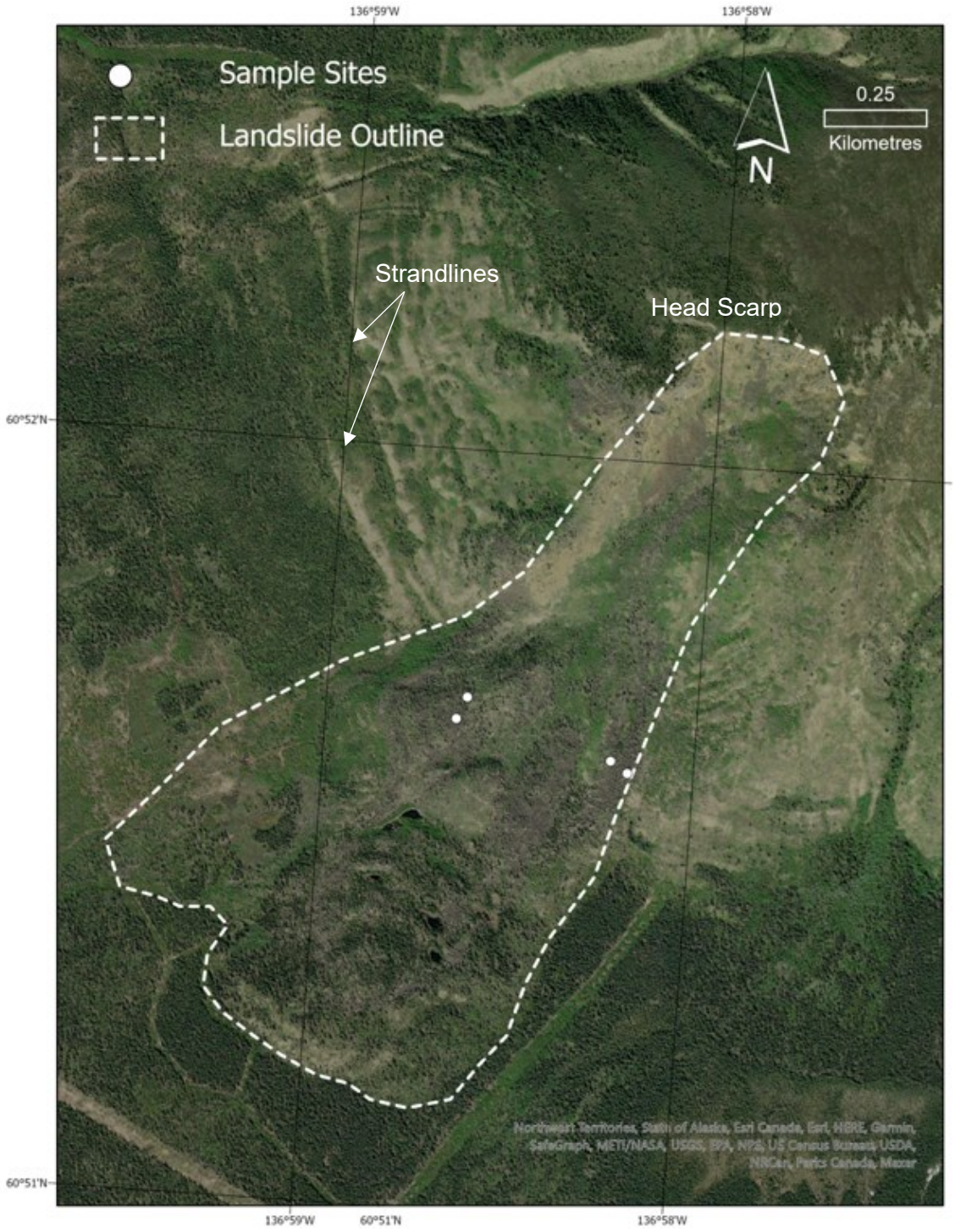

Figure 1.27. Aerial view of the Aishihik rock avalanche. Four TCN samples were obtained from two ridges on the landslide deposit, two on the west 1 (A-01, A-02) and two on the east ridge (A-03, A-04).

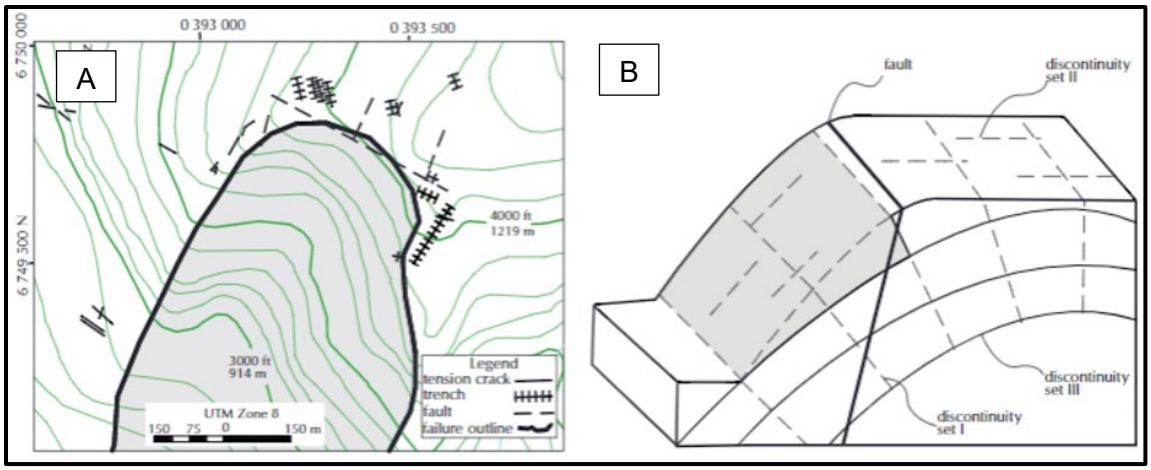

Figure 1.28. Aishihik head scarp. (A) Twenty-five joints, three discontinuity sets, trenches, and minor faults were documented in the head scarp area. (B) These faults and discontinuity sets were determined to be oriented in a way that facilitated the creation of an unstable zone (shaded area). Modified from Brideau et al., 2005.

The rock avalanche is located within the Kluane Schist (Mezger 1997, 2000, 2003; Brideau *et al.,* 2005) (Fig. 1.29). The head scarp is situated near the boundary between the Ruby Range Batholith and the Kluane Metamorphic Assemblage (KK1) where contact metamorphism initiated by the intruded Ruby Range Batholith caused the transformation of the primarily schistose rocks into gneissic assemblages (Fig. 1.30 C; Mezger 1997, 2000; Brideau *et al.* 2005). Debris at this site comprises sub-angular, gneissic blocks of Proterozoic to Mesozoic age Kluane Schist (KK1). Major rock compositions found here are schists with minor assemblages of quartzite; these rocks date from roughly 140-82 Ma ago, during the Cretaceous (Yukon Geological Survey, 2020). No faults have been mapped at this site, but the landslide is located ~ 50 km northeast of the Denali fault.

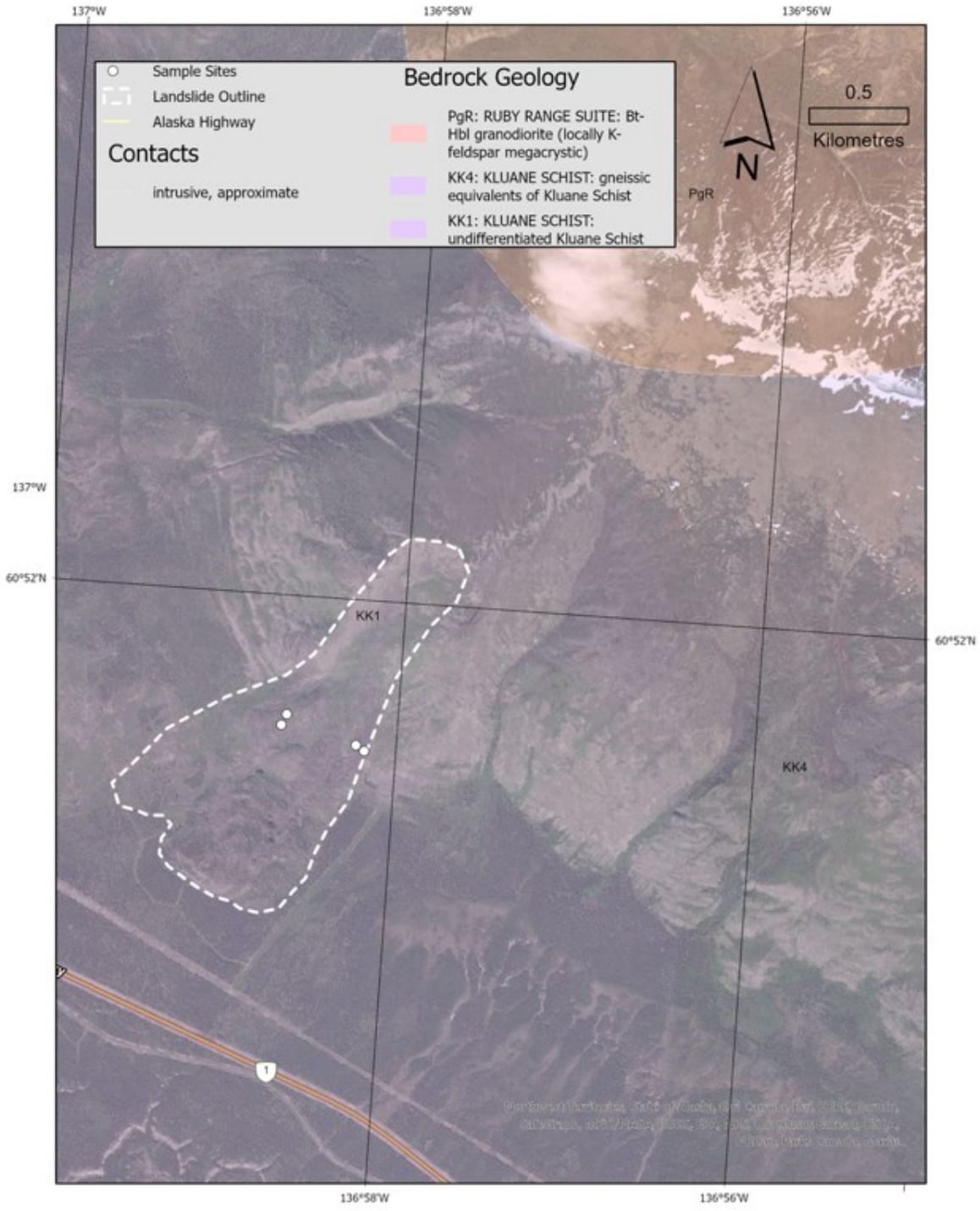

Figure 1.29. Local bedrock geology of the Aishihik landslide (YGS, 2022).

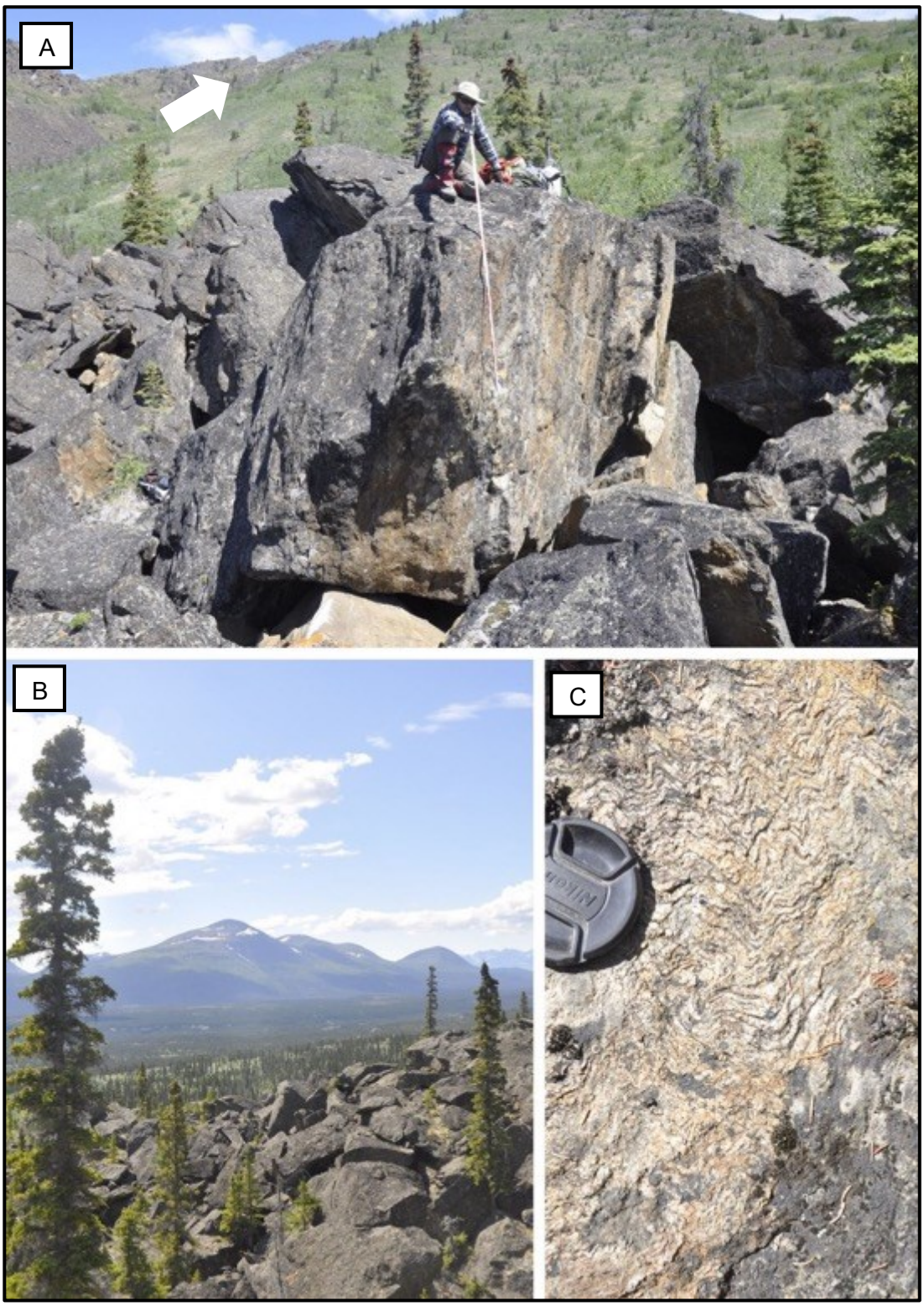

Figure 1.30. The Aishihik landslide. (A) One of the sampled boulders used in ^{10}Be exposure dating. Looking north, the white arrow points to the head scarp (not shown in this image). (B) The boulder field consists of sub-angular blocks and has conifers growing between the boulders of the deposit. (C). Crenulations were present within the boulders at this site.

1.5.5. Gladstone Area

Two landslides were found within the Ruby Ranges to the north of Kluane Lake: Gladstone-1 (61.40° N, -138.28° W) and Gladstone-2 (61.38°, -138.10°W). These landslides were previously mapped by Cronmiller (2019) and are situated within the Ruby Range Batholith (PgR) on the Yukon Plateau (Fig.1.31). Based on U-Pb ages, the age of the batholith's main intrusive phases ranges from 64-57 Ma ago (Israel *et al.,* 2011). Both failures originated from biotite-hornblende granodiorites therefore both deposits consisted of quartz-rich lithology. Based on surficial geology maps of the area, Gladstone-1 terminates above Early Wisconsin – Gladstone tills deposited at the bottom of the cirque (Cronmiller *et al.*, 2019). Gladestone-2 is situated within the larger Gladstone lakes valley which drains into Gladstone Creek. McConnell – Late Wisconsin Marine Isotope Stage 2 glacial limits have been mapped above both head scarps in the Gladstone area (Cronmiller *et al.*, 2019).

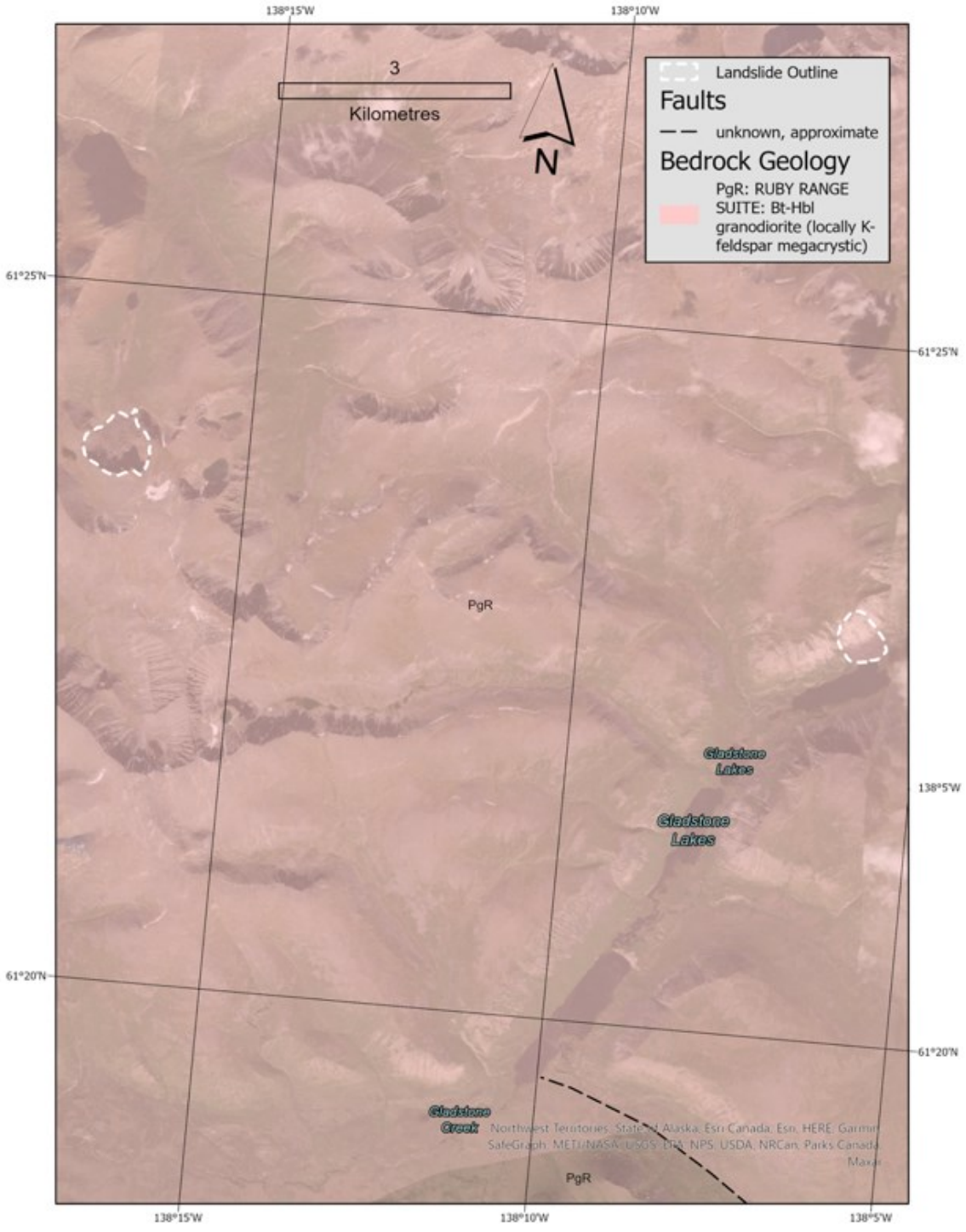

Figure 1.31. The Gladstone area. Two landslides were studied in this region, Gladstone-1 (left) and Gladstone-2 (right) (YGS, 2022).

Gladstone-1 Rock Slide

This NNW-facing rock slide originated from an arcuate head scarp ~0.5 km in elevation and extended ~0.85 km from the failure source (Fig. 1.32 A). The deposit consists of hummocky blocks throughout the base of the cirque valley (Fig. 1.32 B). The toe terminates into a saturated, marshy material (Fig. 1.32 D).

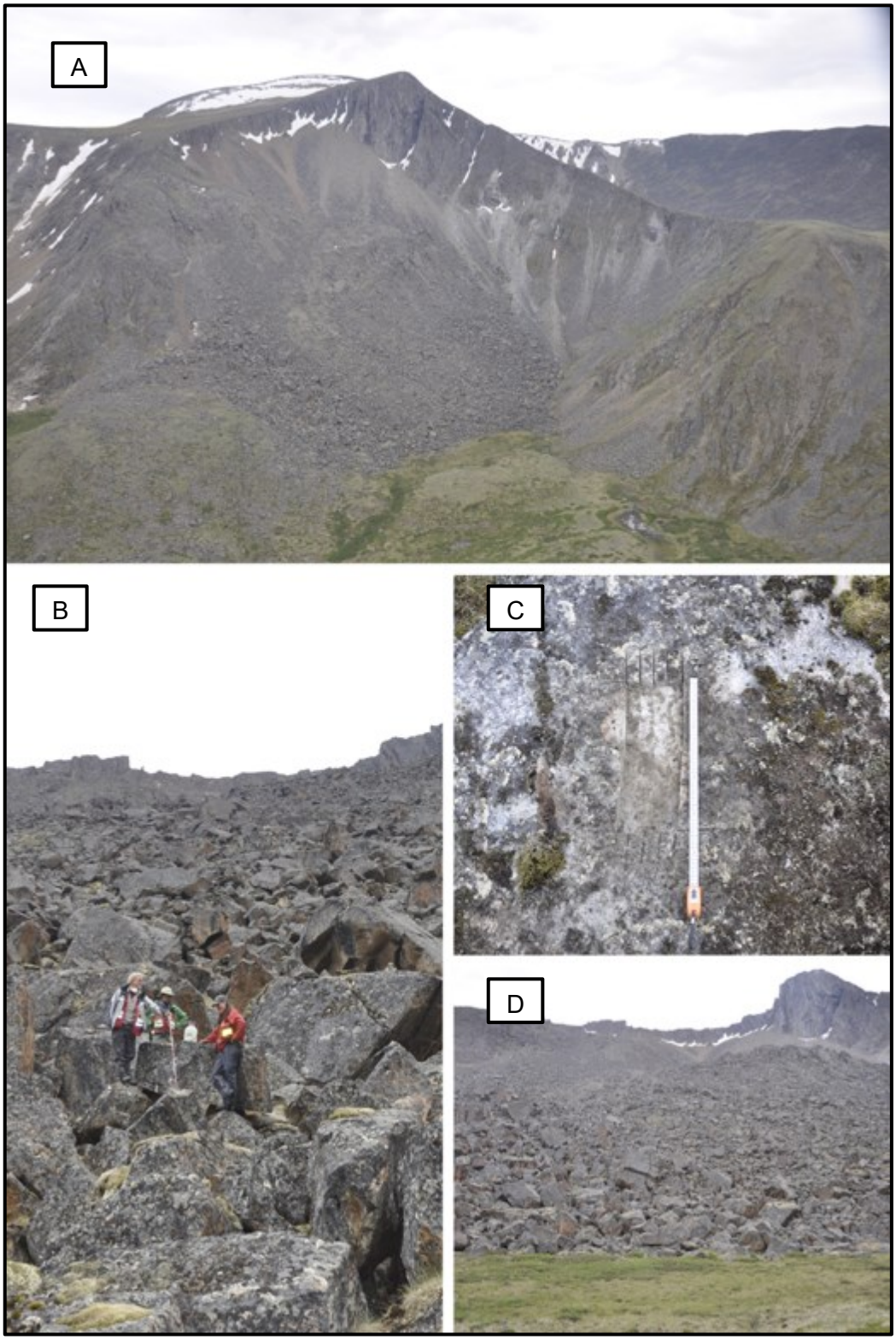

Figure 1.32. Gladstone-1 rock slide. (A) Oblique aerial view of the NNW-facing head scarp and deposit. This rock slide terminated in bog-like vegetation in this cirque. (B) One of the boulders sampled for TCN dating (NW-GC-02); Boulders had a homogenous size distribution and ranged from half a metre to a few metres tall. (C) Another typical sampling surface for a TCN-dated boulder. (D) Boggy, mossy terrain is present at the base of the slide.

Gladstone-2 Rock Avalanche

This landslide is approximately 10 km ESE of Gladstone-1 on a south-facing slope in a meltwater-excavated valley (Fig. 1.33). It appears flatter and has a more spread-like morphology than Gladstone-1. The head scarp is roughly 400 m in elevation and is less arcuate than Gladstone-1. The blocky deposit (Fig. 1.34 A, B, C), which extends ~0.3 km from the head scarp, covers ~0.25 km^2 and abuts Gladstone Lake.

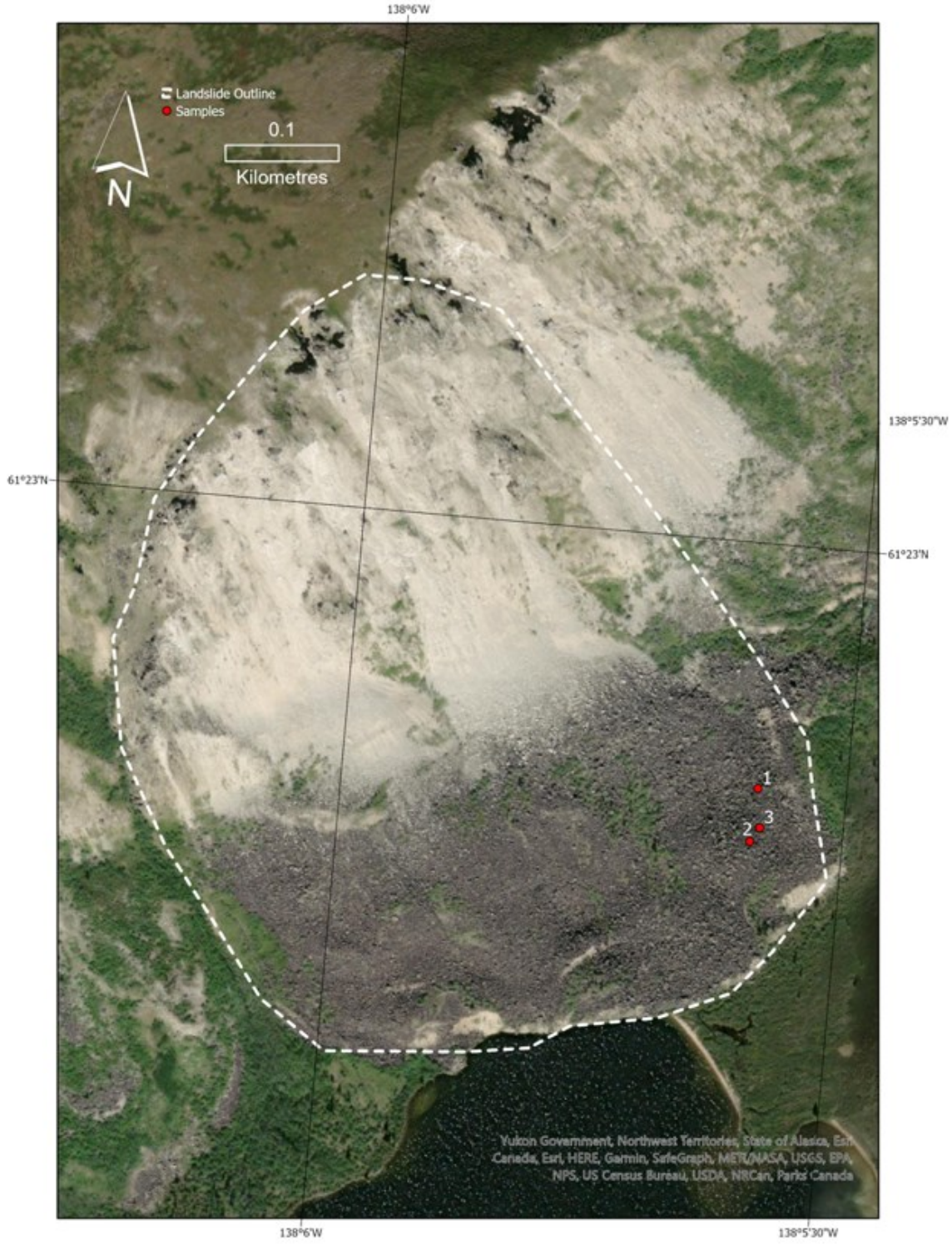

Figure 1.33. Gladstone-2 rock avalanche. Boulders sampled for TCN dating are indicated by the red dots.

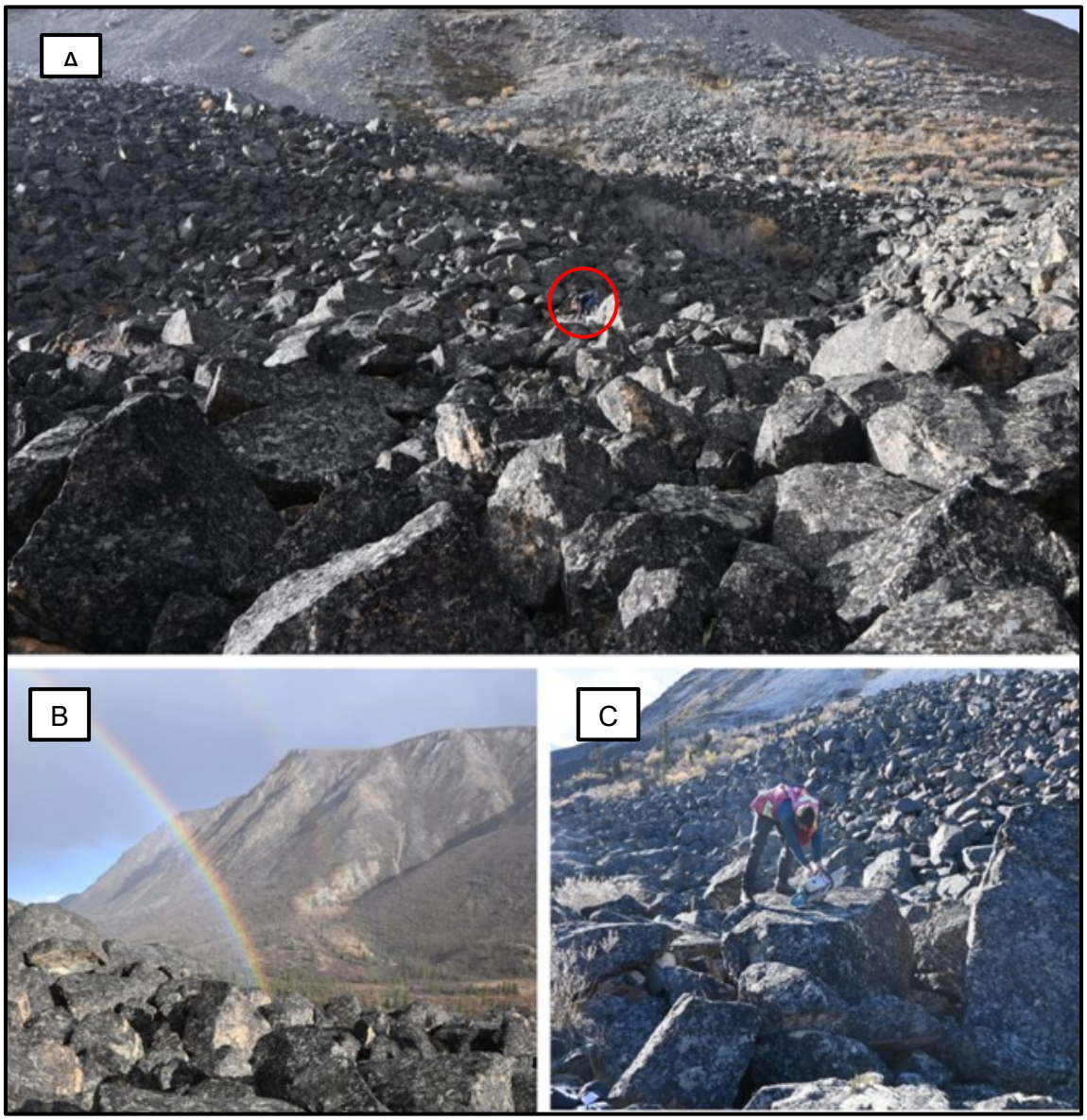

Figure 1.34. Gladstone-2 rock avalanche. (A) Looking up slope on the toe of the landslide, person for scale (red circle). (B) Granodioritic blocks found at this site. (C) TCN sampling boulders.

1.6. Thesis Organization

This thesis will be presented in a modified paper format so that some chapters can be easily converted to journal articles. Chapter 1 is an introduction to the project including the study area and relevant information such as: tectonic, glacial, paleoseismic, and paleoclimatic histories, geological and biophysical settings, and local fault systems. Previous landslide cataloguing research will also be introduced. The study area is described with a brief overview of the five sampled landslides. The short and long-term goals of this study are also addressed here. Chapter 2 describes in detail the methods used during this project: terrestrial cosmogenic nuclide dating, radiocarbon dating, dendrochronology, and tephrochronology. Chapter 3 is a modified journal paper outlining the main research findings of the thesis, including a shortened description of the methodology, expanded landslide descriptions, as well as the ages calculated and their potential triggering mechanisms. Chapter 4 will be an overall summary of the research, exploring future directions and implications of this project while also expanding upon some of the limitations encountered throughout this research process.

Chapter 2. Methodology & Chronological Dating Techniques of Landslides

Before attempting to date a landslide deposit, the deposits were preselected based on their priority and feasibility (*e.g.*, access, sample media, complexity related to multiple landslide events or rockfalls) by desktop mapping using ArcGIS suite, Google Earth®, lidar imagery, air photos, and helicopter traverses. Terrestrial cosmogenic nuclide exposure dating, radiocarbon dating, dendrochronology, and tephrochronology were utilized during this project to obtain ages on as many significant landslides as possible. The chronology benefitted from employing more than one technique for a landslide because each method has advantages and disadvantages. If the site was not deemed viable for TCN dating, exposures that could potentially contain samples for radiocarbon analysis needed to be identified. If these exposures were found, units that were present needed to be described and related to the landslide chronology. At sites where both radiocarbon and TCN samples could be collected, radiocarbon samples were used to verify the calculated TCN ages. If neither TCN nor radiocarbon samples were available, or the event was outside the age constraints of these chronological methods, the perimeter of the event was examined for potential dendrochronological samples. The presence of the eastern lobe of the White River Tephra was also utilized as a relative dating technique since it is common in the study area.

This chapter documents the fundamentals of each dating technique and describes the sampling, laboratory, and interpretation methodologies in more detail than is practical for a journal paper. In some cases, we modified the standard operating procedure, *i.e.*, in the TCN dating portion. The fundamental principles of each technique are described and relevant information for their specific applications to each landslide site is provided.

2.2. Landslide Inventory & Desktop Mapping

The first phase of this project was an extensive background study on landslides, earthquakes, climate studies, glacial history, and other pertinent information in the Kluane Lake region. Digital photogrammetry-based techniques including DATEM Summit Evolution 3D heads-up mapping software, ESRI ArcMap GIS, Google Earth Pro,

orthomosaics, and lidar provided by Brian Menounos (1 m bare earth DEM and hillshade) were all used to identify landslides in the study area. Landslides were compared with a pre-existing inventory provided by the Yukon Geological Survey (YGS). That inventory consisted of landslides catalogued by Rampton (1979), Rampton and S. Paradis (1982), Everard (1994), and Huscroft *et al.* (2004) Koch *et al.,* (2014), as well as a collection of maps, air photos, and open files available from the YGS, the National Air Photo Library, and Natural Resources Canada (Blais-Stevens *et al.* 2010). Surficial geology maps from Natural Resources Canada and associated landslide inventories were compiled from mosaics of aerial photographs catalogued by the National Air Photo Library from 1977, 1979, 198-89, 1992, or 1995.

A desktop investigation of selected landslides was conducted prior to sampling to determine the viability of individual landslides for geochronology. Initial assessments of the landslides helped determine which would be the most accessible in the field, their approximate size, and viability for TCN dating. Landslides were ranked based on: (1) the lithology present (which is important for TCN), (2) the estimated age of the event , (3) the type and complexity of the event (*i.e.* we did not include slow moving mass wasting processes such as progressive rockfall or rock slides, or landslides such as slumps that do not have sufficient mixing of the debris to reset the TCN clock) and (4) the presence of large boulders to optimize TCN exposure dating. Landslides that were selected were chosen based on proximity to fault lines, lithology, failure type, and the volume of failed material, preferably within boulder fields.

Air photos were instrumental in determining the size and type of the examined landslides (Fig. 2.1). This type of evidence provides different temporal perspectives, for example “before and after” photos of the Generc landslide (Fig. 2.2).

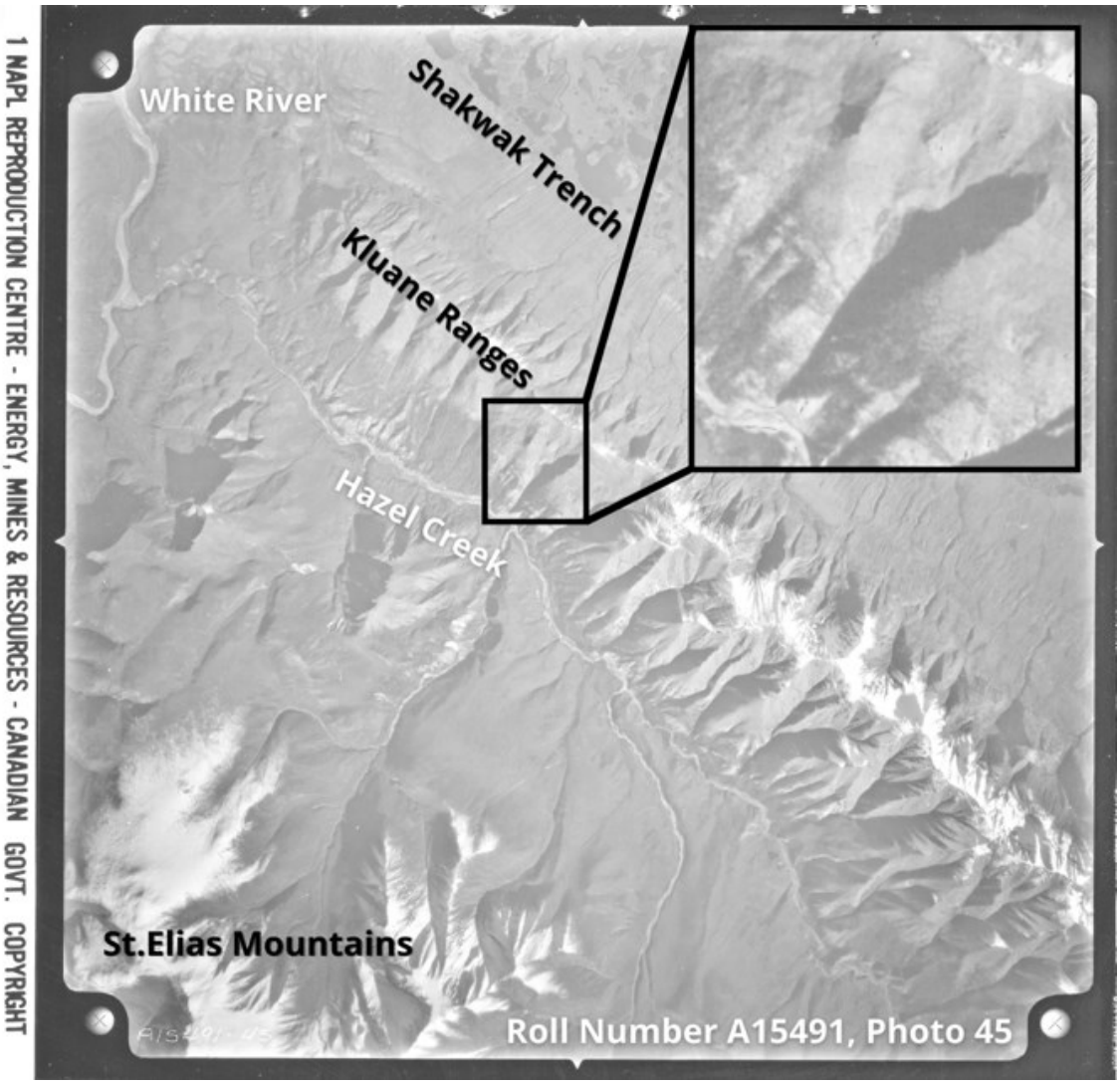

Figure 2.1. The Generc rock slide observed using aerial photography. ©YukonGovernment ©NationalAirPhotoLibrarv.

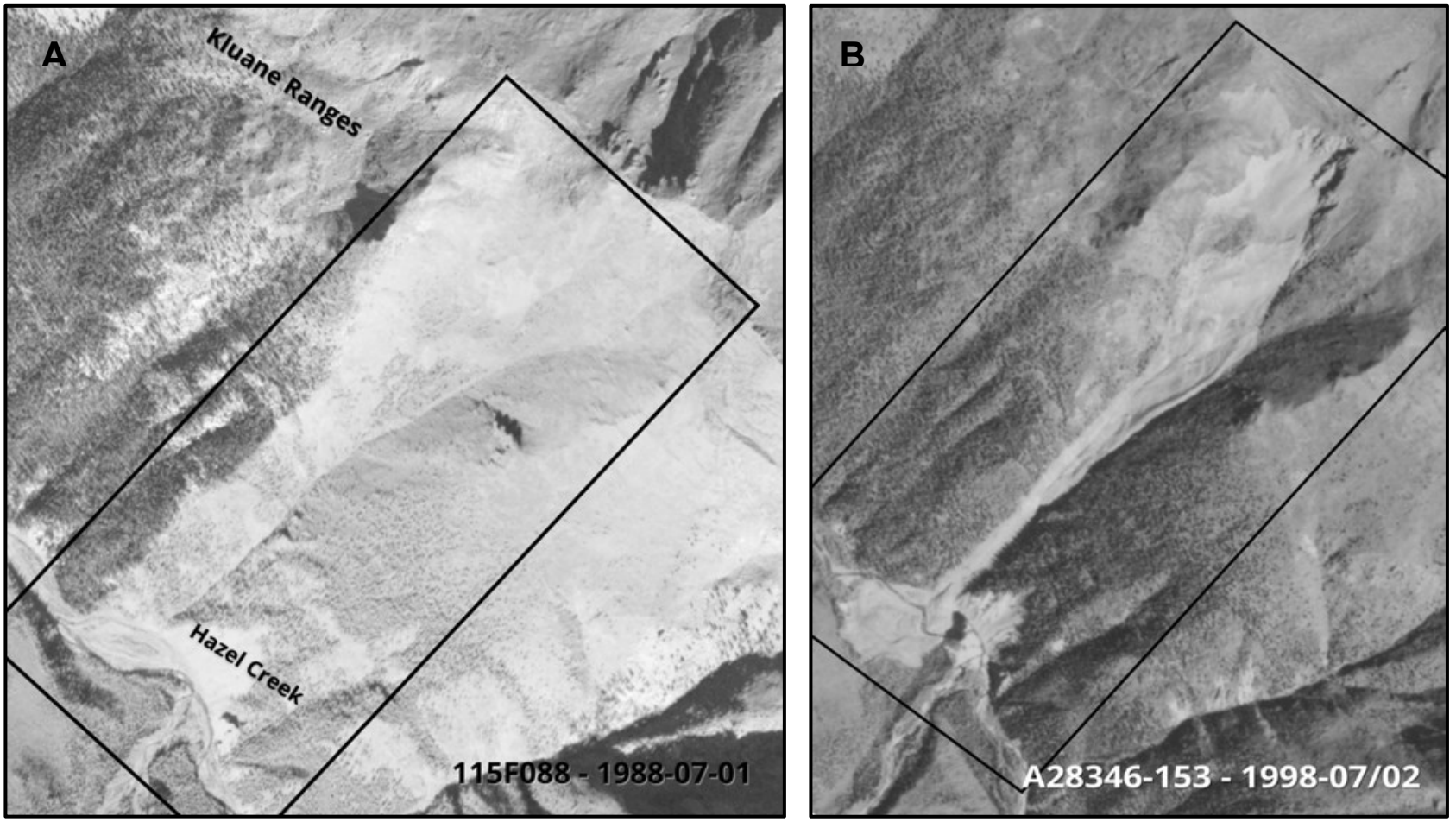

Figure 2.2. Air photos of the Generc landslide area bracketing the timing to between 1988-1998. A) Aerial image 115F088 of the area before the event in 1988 (Yukon Geological Survey Air Photo Library, 1988). B) Aerial image #153 from flight path A28346 after the event (National Air Photo Library, 1998). The landslide is highlighted by the black boxes. ©YukonGovernment ©NationalAirPhotoLibrary.

2.3. Field Work

Field work to evaluate landslides and collect samples was conducted in two parts: a week-long reconnaissance trip with Dr. Brent Ward and Kristen Kennedy in May 2019 and a 12-day excursion with Brent Ward, Crey Ackerson, and Kristen Kennedy in June 2019. Landslides were evaluated for geochronometric suitability and once selected, viable boulders, if present, were described and sampled for TCN analysis. Additional geochronological samples were collected, such as macrofossils for radiocarbon analysis and extant trees for dendrochronology. Standard equipment was used to conduct field work: a Suunto Compass, a laser rangefinder, a gas-powered circular saw and battery-powered handsaw, hand-held GPS, Nikon camera, and a rock hammer and chisel. Field observations such as shielding profiles were measured and input into the CRONUS Washington's Wrapper 2.0, skyline 2.0 program. Additional field measurements included were all recorded or estimated for further evaluation: boulder morphology, snow cover, erosion rates, and spatial orientations of samples (*i.e.*, strikes and dips of boulder surfaces and locations of boulders on the deposit).

Stratigraphic sections were examined for woody materials and other macrofossils for radiocarbon dating; these ages helped provide age constraint on landslide events. Samples were prepared and cleaned at Simon Fraser University before they were sent to the Keck Carbon Cycle Laboratory at the University of California for processing. These radiocarbon ages were then converted to calendar years using Oxcal 4.4.4 software to allow for comparison to TCN ages.

Dendrochronological samples were collected on the Generc landslide. Trees found around the outer margins of the landslide were scarred and leaning which allowed for the determination of the age of impact. The samples collected were dried, sanded and rings were counted under a binocular microscope.

2.4. Terrestrial cosmogenic nuclide exposure dating

The primary dating method applied in this project was terrestrial cosmogenic nuclide (TCN) dating. The measured concentrations of these nuclides permit the calculation of the duration that the sampled rock surface was exposed to cosmic radiation, *i.e.*, exposure dating (Gosse & Phillips, 2001). TCN dating is a relatively recent

and complex dating method. Cosmic rays were first discovered in 1912 by Victor Hess; cosmic radiation and its impact on terrestrial materials was not fully explored until the 1980s due to the lack of instrumentation that could measure such low concentrations consistently, such as high-resolution gas mass spectrometry for noble gases or accelerator mass spectrometry for the radioactive TCNs (Gosse & Philips, 2001). With recent advancements in analytical techniques and our knowledge of the factors that control the *in-situ* production of TCN in minerals on Earth, the concentration of TCNs can act as a clock to determine how long a surface has been exposed to or shielded from incoming cosmic radiation. In general, a higher TCN concentration in a sample corresponds to a longer exposure duration, although many factors, including shielding, erosion, and radioactive decay need to be considered.

In-situ cosmogenic nuclides are produced in rocks by the bombardment of primary and secondary cosmic radiation (Gosse & Klein, 2015). The secondary radiation is the result of primary radiation interacting with upper atmosphere nuclei such as nitrogen. Primary radiation exists in the form of galactic cosmic radiation, and it is expelled from stellar events such as supernovae (Gosse and Phillips, 2001). It consists mostly of high energy particles such as protons, as well as alpha-particles, heavier nuclei, and electrons in lesser amounts (Smart & Shea, 1985; Gosse & Klein, 2015). These particles are accelerated through space and may be deflected by magnetic fields until they decay or interact with mass. On Earth, the initial interaction occurs in the upper atmosphere where they initiate a cascade (cosmic ray shower) of atomic and subatomic particles from spallation and capture by particles that transfer energy to initiate more atomic reactions at deeper depths (Gosse & Klein, 2015). Figure 2.3 depicts the multitude of reaction products yielded by these interactions with particles such as fast neutrons, as they collide with secondary particles in the atmosphere. The average energy of the cosmic ray flux diminishes with each interaction as the secondaries continue to interact at deeper depths in the atmosphere, hydrosphere, cryosphere, and lithosphere. Muons, about 200 times more massive than an electron, interact weakly through those layers and can produce measurable concentrations of TCN at 300 m below the Earth's surface (*e.g.*, Soukup, 2018).

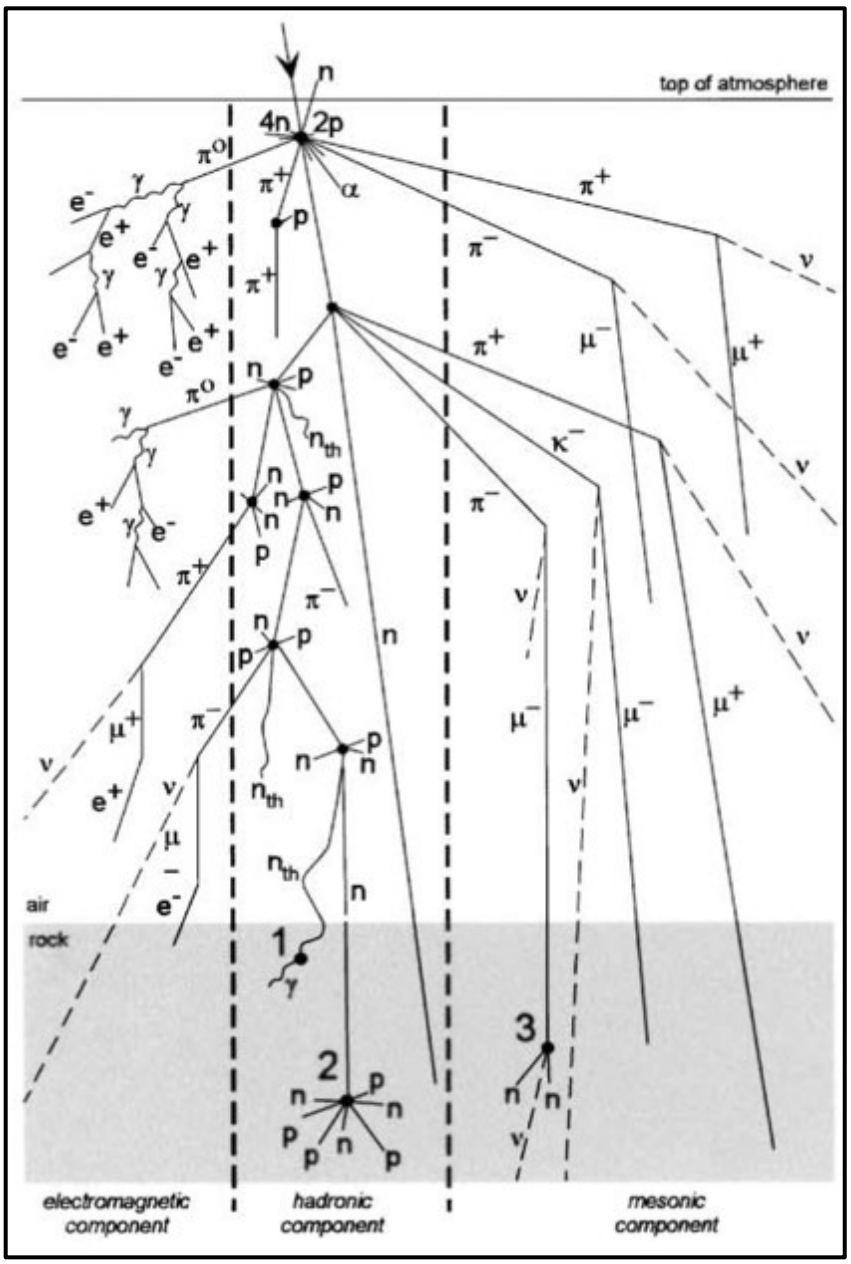

Figure 2.3. Schematic representation of the "cosmic shower", a cascade of atomic interactions that occurs in Earth's upper atmosphere due to primary GCR (typically a fast neutron, n) interacting with upper atmospheric particles. These interactions can be broken down into electromagnetic hadronic, and mesonic components. Secondary particle production can be seen depicted in the atmosphere as well as in rock. Spallogenic interactions can be seen below the rock-air interface where a fast neutron spallates a quartz mineral, in this case, resulting in the release of 3 n^o and 4 p^+ (2). Other in-situ interactions are indicated by the numbers: (1) thermal neutron capture such as $^{35}Cl(n_{th}, gamma)^{36}Cl$; (2) spallation such as $^{28}Si(n,p2n)^{26}Al$, and (3) fast muonic interactions. Modified from Gosse and Phillips, 2001.

TCNs, such as ^{10}Be and ^{36}Cl, are produced *in-situ* in exposed minerals when high energy cosmic rays interact with the Earth's surface or atmosphere (Gosse & Klein,

2015). They have their own associated production rates and pathways that depend on: 1) the energy of incoming cosmic radiation, 2) the type of interaction that occurs, and 3) the mineral chemistry (Gosse & Klein, 2015). The production rates of TCNs have been determined to vary both temporally and spatially based on the strength of the geomagnetic field as well as atmospheric pressure (Lal, 1991). To be useful for geochronology, the TCNs need to meet several criteria:

1) be produced with a sufficiently high production rate so they are measurable,

2) should not be made through a non-cosmogenic pathway (or if so, the probability of their production is slow in the selected mineral),

3) they are either stable (noble gases such as ^{3}He, ^{21}Ne, ^{38}Ar) or have a sufficiently long half-life that they are useful at the geological timescale of interest,

4) the abundance of isobars is sufficiently low and can be mitigated with the chemistry or mass spectrometry methods (e.g. Boron-10 is an isobar of ^{10}Be).

Quartz is the preferred mineral for ^{10}Be due to its common abundance and stoichiometric composition. The process is well understood; silicon and oxygen nuclei can yield ^{10}Be from spallation and muonic processes at ~4 atoms g^{-1} year^{-1} at sea level high latitude (the reference location from which we scale production rates at other sites). ^{36}Cl can be produced in minerals such as feldspars and pyroxenes and other minerals bearing K, Ca, Ti, and Fe for which the spallation production rate is reasonably well known (Marrero *et al.,* 2016a). It requires a slightly more complex consideration than ^{10}Be, in that native chlorine in some minerals (mostly ^{35}Cl) can skew results by producing ^{36}Cl from thermal neutron capture, so chlorine-bearing minerals (hornblende, chlorite) or rocks are usually avoided for exposure dating. Either ^{10}Be or ^{36}Cl measured on the upper surfaces of large boulders on landslide deposits can provide ages.

2.4.2. Inheritance

Samples that have been continually exposed at or below a rock surface and many metres below, accumulate cosmogenic nuclides at a known rate during those exposure periods. In the case of a rock inside a cliff prior to landsliding, the rock will

have a pre-depositional concentration that depends on how deep the future samples were below the surface. This will dictate the amount of TCN inheritance (Hilger *et al.*, 2019). Secondary cosmic rays (primarily fast neutrons and muons) produce in-situ cosmogenic nuclides below a rock's surface at a decreasing rate due to rapid attenuation of the radiation energy with depth; any production deeper than 3 m will be <1% of that which is produced at surface, so inheritance from a more deeply shielded rock will be inconsequential (Willenbring-Staiger, 2005) unless the landslide is on the order of decades instead of hundreds of years or longer. Exposed surfaces, and therefore incoming cosmic radiation, are constantly affected by that radiation (Fig. 2.4 a). Rock volumes that experience greater exposure (higher production rates) are denoted by the more intense red (Fig. 2.4 a). If that slope surface were to fail (Figure 2.4 b), there would be a spectrum of rock samples with varying inherited TCN concentrations depending on their previous placement in the slope. This is even more complicated if the slope fails more frequently (erosion rate of the cliff) and the spatial distribution of the failures (incorporating surfaces with different TCN concentrations). It is important to consider the inherited TCNs because if ignored, the calculated exposure age will be greater than the actual age. Therefore, it is best to sample more than one boulder ($\geq$3) at a site to account for and exclude any outliers (*e.g.* beyond >2σ uncertainty of the mean age of the other samples).

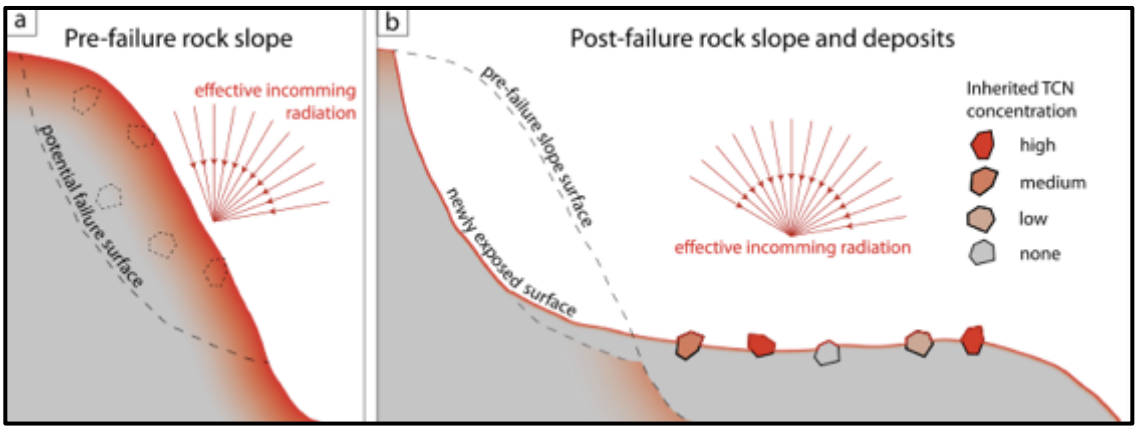

Figure 2.4. Slope areas in red exposed to effective incoming secondary radiation. A) Shows the pre-failure rock slope surface. Here, the intensity of the red colour represents the amount of exposure that area is exposed to. A brighter red means that the surface has a higher accumulated TCN concentration. The failure plane and resulting failure surface are represented by the dashed line. B) Depicts the post-failure surface and deposit. Modified from Hilger et al. (2019).

2.4.3. ^{36}Cl versus ^{10}Be Dating

^{36}Cl and ^{10}Be are two terrestrially produced nuclides that have very different production pathways; therefore, these unique nuclides can be used for different chronological studies and age ranges. ^{10}Be produced in quartz minerals by the spallation of ^{16}O into ^{10}Be is shown in equation 2.1 ^{10}Be in quartz has a half-life of 1.387x10^{6} yr (Chmeleff *et al.,* 2010; Korschinek *et al.,* 2010). This is one method of production, in the use of TCNs for cosmogenic dating, the sum of all the production pathways of the nuclide is used for final counts.

$$^{16}_{8}O\ (n, 4p3n)\ ^{10}_{4}Be \qquad \textit{Eq. 2.1}$$

Fundamentally, *in-situ* ^{10}Be at the Earth's surface can be used to determine the duration of exposure a sample has been exposed to cosmic radiation (T; annum, a). Using equation 2.2, the ratio of the isotopic concentration (N; atoms g^{-1}) and the nuclide production rate at the surface sampled (P_0; g^{-1} a^{-1}) can be used to determine the exposure age (Morris *et al.,* 2002). Depending on factors such as elevation, latitude, and depth below the rock surface, P_0 will vary (Morris *et al.,* 2002).

$$T = \frac{N}{P_0} \qquad \textit{Eq. 2.2}$$

^{36}Cl is a radioactive isotope of Cl and in exposed rock, it is produced from the spallation of the nuclei of more massive atoms such as stable ^{39}K, ^{40}Ca, ^{48}Ti, and ^{56}Fe. Spallation is when a fast neutron (n) produces ^{36}Cl from a collision interaction in a similar way to the production of ^{10}Be from O and Si. While Si and O are in stoichiometric abundance in quartz and so do not have to be measured, the four common target elements for ^{36}Cl must be measured by ICP to determine the total production rate in a sample. There is also thermal neutron capture by ^{35}Cl to produce ^{36}Cl (equation 2.3), so it is essential to determine the abundance of stable ^{35}Cl isotopes in the sample material analyzed. Muons also produce ^{10}Be and ^{36}Cl but at a boulder surface, this is at a much lower rate than spallation and thermal neutron capture. They are nevertheless included in the computation of total production rate.

$$^{35}_{17}Cl\ \{n_{th}, \gamma\}^{36}_{17}Cl \qquad \textit{Eq. 2.3}$$

2.4.4. Sample Selection

As with most geochronological methods, one of the cornerstones of terrestrial cosmogenic nuclide dating involves the appropriate selection of sample media. Depending on the nuclide that is to be extracted, several variables must be considered when choosing a field sample or site, but unlike most radiometric dating techniques, this method also depends on erosion history and cover by materials such as forests, ash, snow, or water. Large-scale deep-seated rock failures (>1 km^3) were sampled as they were less likely to be impacted by inheritance or post-depositional displacement and could be seismically triggered by a large enough event (which is important to this regional study).

Boulder Selection

Boulders larger than 1 m tall, with preferably flat, exposed surfaces, were selected for several reasons. The larger the boulder, the less likely we were to sample a surface that had inherited nuclides pre-failure. The sampled face would be less likely to have inheritance as there would only be a 1 in 6 chance the surface was previously exposed on the slope. If a surface were previously exposed pre-failure, then the other faces in this case would have been more shielded and would have a smaller chance of acquiring pre-failure inheritance. These larger boulders are also less likely to be impacted by thick snow or ash cover as wind would blow off the cover which would partially shield the surface from cosmic radiation and reduce the TCN production rate. Boulders with a flat surface also have simpler geometry to calculate the cosmic ray flux. Samples were collected using a gas-powered diamond-blade cutoff saw. Parallel cuts 3 cm apart and 2-3 cm deep were cut and removed with a hammer and chisel so 'bars' of rock could be removed. As the attenuation of ^{10}Be-producing fast neutrons decreases exponentially with depth (*e*-folding length of 150 g cm^{-2}), care was taken not to saw too deeply into sampled surfaces so average thicknesses of the bars were around 2-3 cm thick (Gosse & Philips, 2001; Willenbring-Staiger, 2005). Lithology and sample thicknesses (nearest 0.5 cm) were recorded from collected sample surfaces (Table 2.1; Heyman *et al.,* 2016).

A collection of field sample photos can be found in Appendix A. These highlight the requirements for proper boulder selection. If the boulder's surface appeared too eroded, *i.e.* too smooth, that was indicative of a diminishing surface that could potentially skew nuclide counts and may provide an under estimate age. If there was spalling of

rocks off the surface, or thick loess cover, these factors could also potentially alter production rates and nuclide counts.

Table 2.1 Summary of field samples collected during the 2019 field season.

Field ID	Lab ID (CRISDal#)	Nuclide of Interest	Lithology	Av. Sample Thickness (cm)
NW-SM-OLS-01	5376	^{36}Cl	Metabasite	2.95
NW-SM-OLS-02	5377		Metabasite	3.0
NW-SM-OLS-03	5378		Metabasite	3.0
NW-SM-OLS-04	5379		Metabasite	3.0
NW-SM-01	5380		Metabasite	4.0
NW-SM-02	5381		Metabasite	2.0
NW-SM-03	5382		Metabasite	2.5
NW-SM-04	5383		Metabasite	3.0
NW-A-01	3907	^{10}Be	Gneiss	2.75-3
NW-A-02	3908		Gneiss	2.75
NW-A-03	3909		Gneiss	3-3.5
NW-A-04	3910		Gneiss	2.5
NW-GC-01	3911		Granodiorite	3.2
NW-GC-02	3912		Granodiorite	2.0
NW-GC-03	3913		Granodiorite	2.6
NW-GLS-01	4109		Granodiorite	3.2
NW-GLS-02	4110		Granodiorite	2.0
NW-GLS-03	4111		Granodiorite	2.6

2.4.5. Mineral Separation and Chemical Pre-treatment

All physical and chemical preparations were conducted at the Cosmic Ray Isotope Sciences at Dalhousie (CRISDal) Lab. A total of 18 samples underwent purification for TCN dating: 8 ^{36}Cl samples, and 10 ^{10}Be samples (Table 2.1). The first step towards utilizing a particular nuclide for age-dating requires the isolation of the target mineral; the one that the nuclide is found in. ^{10}Be is produced in Quartz and ^{36}Cl can be produced in several minerals: feldspar (for K, Ca), magnetite or olivine (for Fe),

or carbonates which target the Ca-produced ^{36}Cl (Gosse & Phillips, 2001). Prior to any laboratory procedures, a thorough record of the field sample was documented in the lab (mass, mineral abundance, microscopy notes); a representative subsample was archived in case whole rock chemistry was required or a thin section was needed. The following pre-treatment procedures are applied specifically to ^{10}Be samples, but certain steps may be omitted from ^{36}Cl preparation; therefore, the following steps pertain to a ^{10}Be sample unless stated otherwise. The physical pre-treatment follows the CRISDal Lab standard operating procedures (SOP) for sample pre-treatment. Many of the instruments for mineral separation (Sturtevant Jaw Crusher, Bico disc pulverizer, sieve shaker, Frantz electromagnetic separator, and heavy liquids) use protocols similar to the USGS Open-File Report 2016-1022 (Strong & Driscoll, 2016). Additional methods, including froth floatation, partial digestion, air abrasion, and acids that do not digest quartz, are described in the CRISDal Lab SOPs. The following were just some of the techniques employed throughout the laboratory portion of this thesis to isolate the minerals of interest.

Jaw Crusher and Pulverizer

In the Crystal Isolation Facility in the Department of Earth and Environmental Sciences at Dalhousie, the boulder sample was cleaned of any sediment or lichens and was inserted into the Jaw Crusher where it was reduced to manageable sizes (1-cm diameter); these were then placed into the chute of the Pulverizer with a pair of disks (one spinning) with spacing that can be adjusted. The sample was comminuted to incrementally smaller sizes until it was within a range suitable for analysis, then it was sieved. For ^{10}Be samples, this was 150 – 250 μm and 250 – 355 μm. The larger grain sizes were used for ^{10}Be because during subsequent chemical processes, the surface of the quartz grain needed to be digested to allow for the complete removal of any atmospheric ^{10}Be. For the ^{36}Cl samples, smaller sizes in the 150 – 250 μm were preferred to concentrate small feldspars, olivines, and magnetites.

Froth Floatation

Froth flotation involved the separation of hydrophobic versus hydrophilic minerals such as the quartz (hydrophilic) from feldspars (hydrophobic) (Wang & Liu, 2021). This involved soaking the crushed sample in 1% hydrofluoric acid for several hours to allow for as much disaggregation of the grains as possible; it also facilitated the separation of

the sink portions from the hydrophobic float. For the ^{10}Be samples, the quartz-rich sink portions for the 150-250 and 250-355 μm were selected for further chemistry. For ^{36}Cl studies, the feldspars were desired; thereby the float was used further whereas the sink was not.

Frantz Magnetic Separation & Hand Picking

The Frantz Magnetic Separator separated non-magnetic, paramagnetic and magnetic minerals. Prior to running samples through the machine, a simple horseshoe magnet was used to remove highly magnetic minerals (*e.g.*, magnetites) in both the ^{10}Be and ^{36}Cl samples to avoid clogging the Frantz. Grains were then fed through a hopper funnel connected to the Frantz, directing the grains into a two-channeled chute with an adjustable vibration setting depending on the strength of the magnetic field and the magnetic properties of the grains (Strong & Driscoll, 2016). Adjusting the current controls the strength of the external magnet; thus, different currents separated different magnetic minerals. By re-running a sample through increasingly higher currents, magnetic, paramagnetic, and even diamagnetic minerals could be removed for further analysis.

For ^{10}Be, magnetic minerals were preferentially selected out at currents of 1.65 A or less, therefore, remaining sediment that was not magnetically separated was used for further mineral separation to concentrate the quartz.

For ^{36}Cl samples, magnetite was the preferred mineral for analysis and was used for the ^{36}Cl targets. These were selected by handpicking out the grains using a standard horseshoe magnet (non-rare earth mineral magnet). Feldspar and olivine were also desired and could be separated from other minerals.

Heavy Liquid Separation

This step was used before chemical methods of mineral separation. Using the basic principle that different minerals have different densities, physical separation can be achieved to help concentrate a mineral of choice. Heavy liquids of known density, typically Lithium meta-tungstate (LMT, densities ranging from 2.85 g cm^3 and lower), can help separate minerals over the course of a few minutes and is a relatively quick and cost-efficient way of bulk mineral separation (Strong & Driscoll, 2016). However, recovery of the LMT is time consuming. Care was used to thoroughly rinse the grains to remove any of the lithium meta-tungstate from the sample.

Aqua Regia (for ^{10}Be only)

Samples were immersed in aqua regia (3 HCl : 1 HNO_3 reagent-grade concentrated acids) to help separate the constituents of multi-mineralogical grains, and to weaken micas and other minerals. This acid-sand mixture was then left covered on a hotplate to boil around 150 – 250 °C for 2 hours or more and was stirred every 15 minutes. Once the acid was decanted and neutralized using sodium hydroxide, the samples were dried pending further purification of the quartz.

This step was not applied to the ^{36}Cl analysis as the HCl in the mixture would contribute Cl to the sample and impact the ^{36}Cl measurements. For pre-treatment leaching, samples were placed in weak HNO_3 (a mixture of water with 2M HNO_3) to remove any trace meteoric Cl (<1%).

Hydrofluoric Etching

Depending on the mineral purity of the sample, the sample may have needed to be digested in 1 HF:1 H_2O or 2 HF:1 H_2O deionized water over multiple rounds of boiling. This would preferentially soften aluminosilicates that were difficult to remove based on density, electrostatic, or magnetic properties. Following etching, the acid was decanted, and the acid-sand mixture was neutralized. Following this treatment, only Type-1 (18.2 MOhm) deionized water was used to clean and neutralize the samples as this prevented the introduction of contaminants.

Sand Abrasion

Following hydrofluoric etching, 30-g of sample targeted for ^{10}Be in quartz were placed into custom designed stainless-steel abraders where 80 psi compressed air was injected through a tilted multiholed manifold that optimized grain to grain contact of sand-sized grains. Softer pre-etch feldspars and other minerals were pulverized and escaped the chamber through holes with 100 or 75 µm mesh, and while some quartz was lost, the method only takes about 30 minutes to take a sample with 40% quartz to 98% quartz. This also aided in the removal of any residual meteoric ^{10}Be on the quartz. It also served as a means of disaggregating the quartz sample for additional acid treatments. This method was utilized on the ^{10}Be samples; the quartz-rich product required ultrasonic cleaning afterwards to remove coatings from the still and pulverized minerals.

Ultrasonic Separation

During this step, Teflon bottles were loaded with the sample (mass depended on bottle size and sample size, ultrasonic tank size) and partially filled with HF/HNO_3. The bottles were placed in a tank to heat over 6 hours or overnight. Samples were then rinsed, and the wastewater neutralized. The ultrasonic vibrations and acid soak were an additional means to help purify the quartz further and soften minerals that are more easily digested.

Hexafluorosilicic Acid Treatment

If pure enough quartz sample still had not been achieved (commonly in the case of samples beginning with less than 5% quartz), as determined microscopically or with measurements of the major cations by inductively coupled plasma-optical emission spectrometry (ICP-OES), samples were soaked in hexafluorosilicic acid-filled bottles and left for multiple days or weeks to roll on steel (hotdog) rollers. They were then thoroughly rinsed multiple times in deionized water (the acid is known to produce elevated concentrations of ^{10}Be) and reassessed for purity.

ICP-OES

Inductively coupled plasma-optical emission spectrometry (ICP-OES) at CRISDal Lab was utilized to test the mineral purity and evaluate the concentration of major elements that could interfere with the ^{10}Be target chemistry (an example of these results can be found in Appendix B) (Gaines, 2011). If Al abundance in the quartz concentrate exceeded 100 µg/g, more mineral purification was conducted. Typically, the high Al content indicated the unwanted presence of feldspar. In case the Al test was negative, major elements that could have a concentration great enough to impact the ion chromatography were measured. This step was not completed for ^{36}Cl because the sample was just screened optically for feldspar, magnetite, or olivine. Once the quartz was considered sufficiently pure, the sample underwent three or more repetitions of acid digestion in HF and HNO_3 with rinses between each step to remove 35% of the quartz (a minimum required to remove meteoric ^{10}Be; Nishiizumi *et al.,* 1991).

2.4.6. Nuclide Extraction & Carrier Addition

Once the mineral had been sufficiently purified, AMS targets were prepared: BeO or $AgCl_3$. This required the addition of isotopically enriched carriers (^{9}Be for ^{10}Be, and $^{35+37}Cl$ for ^{36}Cl) so that the target had sufficient mass to be sputtered in the Cs source and so that there was sufficient stable isotope to measure (accelerator mass spectrometry (AMS) measures the ratio of the radionuclide to the stable nuclide).

Column chemistry was required to separate the Be or Cl from unwanted ions based on their charge and ionic radii. For ^{10}Be, once the quartz and carrier mixture were digested the sample was eluted through an anion exchange column and then a cation exchange column. This was conducted by Guang Yang due to Dalhousie University and CRISDal Lab Covid restrictions. The ^{10}Be samples were precipitated into a $Be(OH)_2$ gel using Matheson ultimate grade ammonia gas before conversion by calcining in a Bunsen burner into the BeO target. Niobium powder was then added to the BeO and packed into cathodes at the ratio of Nb:BeO optimal for the AMS lab (in this case, CAMS-LLNL).

For ^{36}Cl, when the sample was dissolved, the solid phase was rinsed so that no sample was left in the solid residuum. The final goal for producing a pure $AgCl_3$ target was achieved with a combination of column chemistry, multiple (average five) precipitations in $BaSO_4$ to remove the isobaric sulfur (^{36}S) from the samples, and an AgI reaction to produce the $AgCl_3$ precipitate. AMS target pucks were prepared at PRIME lab where the samples were analyzed for $^{36}Cl/Cl$.

Process blanks (using the carrier without mineral mass but with all other reagents and processes) were run in parallel with each sample batch (up to 8 samples) and converted to atoms to subtract from the measured number of atoms measured for each ^{10}Be and ^{36}Cl sample.

2.4.7. Isotope Isolation

The next phase of TCN analysis involved the utilization of the different isotopic masses of Be and Cl to isolate the nuclides of interest using accelerator mass spectrometry: ^{9}Be was separated from ^{10}Be and $^{35,37}Cl$ are separated from ^{36}Cl. The stable isotopes were measured separately (*e.g.* with an off-axis Faraday cup) but the rare cosmogenic radionuclide was measured by a gas-filled detector which counts

electrical signals that were interpreted to be ^{10}Be or ^{36}Cl nuclides. The ^{10}Be and ^{36}Cl samples were measured at Lawrence Livermore National Laboratory Center for AMS and PRIME Lab, respectively. Because I had a first-hand experience exploring the AMS at A.E. Lalonde AMS Laboratory at the University of Ottawa, I will be referring to that AMS in the following description (Fig. 2.5).

Accelerator Mass Spectrometry

All unknown sample targets were loaded into a wheel with known standards where a potential difference was created using a positive Cesium sputter source and a negatively charged BeO^- target sample. These were run with known $^{10}Be/^{9}Be$ standards that were later used to normalize the data. For example, a normalizing standard with an accepted $^{10}Be/^{9}Be$ of 2.81×10^{-12} may measure only 90% or 60% of that value at some other accelerator, so the measured sample target ratios were divided by that amount to compensate (normalize) with the accepted standard.

A Cesium sputter source was used to propel molecule ions from the target through the rest of the beam. The negatively charged molecules of $^{10}Be^{16}O^-$ (mass=26) were electrostatically repulsed from the negative cesium source through various devices designed to magnetically separate m=26 molecules from lighter or heavier particles and electronically steer the beam of particles toward the high voltage accelerator (*e.g.*, 3MV for A.E. Lalonde laboratory) and ultimately through the detector. Magnets placed in angled bends require the particle to have precisely the right mass and charge to bend the beam of $^{10}Be^{16}O$ through the beam line. Three magnets are placed throughout the Lalonde line: an injection magnet, an analyzing magnet, and a switching magnet. Isotopes bend depending on their mass and charge; larger isotopes are not bent as much as smaller isotopes. The strength of the magnetic field and manipulation of the beam line were configured through the control room and was isotope-specific, utilizing the basic physical principles of magnetic and electrostatic fields and force. Electrostatic analyzers are placed throughout the line; in the gas filled tank where most electron stripping occurs, molecules were accelerated to unstable conditions due the loss of their electrons, thereby removing them from the beam. There are two ways that electrons can be stripped from unwanted molecules: one requires the use of gas with known properties and is contained with a known pressure so that only the mass of the incoming beam can be varied, and two, a mylar foil that acts as a physical barrier to the atom beam.

Once the beam had been directed past the low energy and high energy (post-AMS) end of the spectrometer, isobutane gas in the detector was used to slow down the transmission of the beam where ^{10}Be ions were successfully separated from isobaric ^{10}B ions. The number of counts of ^{10}Be ions detected was proportional to the number of ^{10}Be atoms in the sample target. However, because transmission of ^{9}BeO and ^{10}BeO through the accelerator can vary, the AMS measures the ratio of ^{10}Be/^{9}Be for minutes to hours, which depends on the lab and nature of the experiment. Because we know how much ^{9}Be was added to the quartz as carrier, we multiplied the number of ^{9}Be atoms added by the AMS measured ratio to compute the number of ^{10}Be atoms per gram of quartz digested.

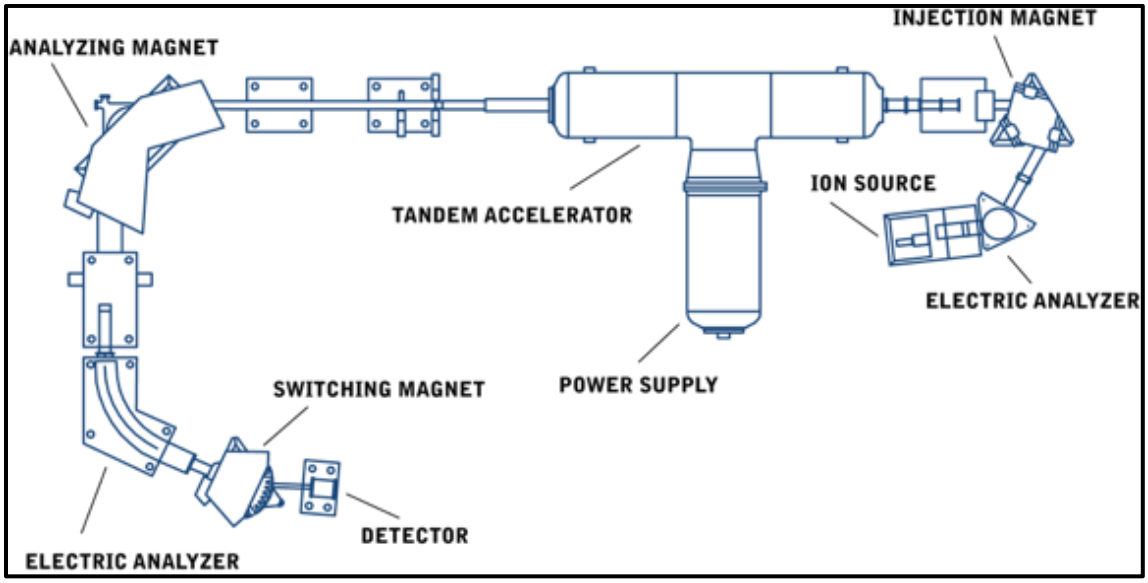

Figure 2.5. Schematic of the tandem accelerator at University of Ottawa's A.E. Lalonde AMS Laboratory. Retrieved from A.E. Lalonde.

2.4.8. ^{36}Cl Analysis

Samples undergoing ^{36}Cl analysis required a different target preparation compared to ^{10}Be analysis and no column chemistry was used. Due to the lack of feldspars in the Sheep Mountain samples, magnetite and other Fe-bearing minerals were isolated and combined with the feldspars. Samples were sent to SGS Canada Inc. for analytical measurements (*i.e.* by XRF, ICP-MS) to determine:

1) the concentration of the four common spallogenic target atoms, K, Ca, Ti, and Fe in an aliquot of the final sample that was digested;

2) the concentration of all major and selected minor elements in an aliquot of the pre-leached sample, including loss on ignition (LOI) for the measurement of quantitative water that can moderate the availability of thermal neutrons for thermal neutron capture production of ^{36}Cl, or CO_2 in the case of carbonates;

3) and the concentration of minor and trace elements that can lead to the production of ^{36}Cl by radiogenic or nucleogenic pathways (including thermal neutron producers).

These measurements are required for practically any calculation of the cosmogenic ^{36}Cl production rate, because unlike quartz, most of the minerals used do not have chemical formulas with simple stoichiometric abundances. A benefit of ^{36}Cl therefore was its ability to be useful for dating practically any rock type if there is sufficient K, Ca, Ti, or Fe to make enough ^{36}Cl for the precision required.

^{36}Cl Chemical Pretreatment and Treatment

The following is summarized from the CRISDal "Chemical procedure for the extraction of ^{36}Cl from silicate minerals", 2007. ^{36}Cl is primarily produced from the spallation of atoms larger that itself (*i.e.* K, Ca, Fe). Therefore, preparing the chlorine samples involved isolating feldspar and magnetite within the Sheep Mountain samples and to remove as much ^{35}Cl-bearing minerals as possible (*i.e.* hornblendes, micas, salt). It also involved several pre-leaching and leaching phases following physical separation of the ^{36}Cl-bearing minerals. Three aliquots were collected for further elemental measurements. Two blanks were added for analytical comparison: a "process blank" (5367) which received a carrier and all reagents, but no mineral sample, and a "blank blank" (5368), which received the carrier, but no sample nor other reagents except AgCl for the production of a $AgCl_3$ target. The treatment workflow is:

1) sample pretreatment and isolation of aliquot 1 for calculating radiation (*i.e.* U, Th), whole rock measurements. This aliquot was used to determine how much nucleogenic and radiogenic particles were present that could lead to the production of ^{36}Cl. Aliquot 2 was for the major elements and selected minor elements in the whole rock (pre-leached sample).
2) several leaching sequences of varying concentrations of HNO_3 and deionized water to remove any external, elemental impurities.

3) the recovery of two more aliquots for analysis. Aliquot 3 was used for determining the spallogenic target elemental abundances (K, Ca, Ti, Fe).

4) addition of $^{35}Cl^-$ carrier (ID: 20120620, 0.796 mg/ml) and the dissolution of the sample in varying cocktails of HNO_3 and HF.

5) separation from the dissolution solid residuum.

6) the first precipitation of AgCl using 10% $AgNO_3$.

7) repeated sulphur removal to reduce ^{36}S isobaric concentration, through the addition of NH_3 solution and $BaNO_3$.

8) the second precipitation of AgCl.

9) drying and pressing of target puck for shipment to PRIME Lab.

2.5. Radiocarbon Dating

The second geochronological technique used in this thesis was radiocarbon dating, which was combined with TCN dating at Sheep Mountain. Radiocarbon dating is based on the incorporation of radioactive ^{14}C into living organisms, along with ^{12}C and ^{13}C (Libby, 1954). The abundance of ^{14}C in the atmosphere relative to the other C-isotopes, ^{12}C or ^{13}C, is reasonably well known for today, although it has varied substantially over year to kiloyear timescales. An important assumption is that while alive, the organism's carbon isotope ratios were in equilibrium with the atmosphere. Upon death, this uptake stops, and radioactive decay changes the equilibrium; by measuring the ratio of $^{14}C/^{13}C$ in the fossil and comparing that with the expected $^{14}C/^{13}C$ in the atmosphere at the time of death, it is possible to determine how much decay (*i.e.* duration of death) that would explain the difference in the two ratios.

^{14}C is produced in the atmosphere when a ^{14}N captures a cosmogenic secondary thermal neutron producing a radioactive ^{14}C isotope (Equation 2.4).

$$^{14}_{7}N\{n, ^{1}_{1}H^{+}\}^{14}_{6}C \qquad \textit{Eq. 2.4}$$

This meteoric ^{14}C (as opposed to *in-situ* ^{14}C) is then incorporated into biological matter, either through photosynthesis in plants or animals eating plants, where it

Eq. 2.5

remains in a steady state with the atmosphere. When the organism dies, there is no longer a steady state exchange with the atmosphere, and beta decay of ^{14}C, where ^{14}C is converted to ^{14}N (Equation 2.5), exponentially reduces the abundance of ^{14}C in the sample.

$$^{14}_{6}C\{^{1}_{1}H^{+}\}^{14}_{7}N$$

In the field, organics such as twigs and wood (Fig. 2.6), were observed and sampled in sections stratigraphically above and below the landslide event. Submitted samples (see below) were carefully selected as modern roots were present and some penetrated the organic samples; this could skew results towards a younger age, thereby introducing error in the chronology.

The samples were submitted to the Keck Carbon Cycle AMS Facility in the Earth System Science Department at UC Irvine for analysis and are shown below. Sample NW-SMNRC-W-01 is shown in Figure 2.6. Photos of all radiocarbon samples submitted are found in Appendix C.

1) NW-SM-RC-01(twig)
2) NW-SM-RC-01 (twig 2)

} Southern exposure

3) NW-SMNRC-W-01 (wood)
4) NW-SMNRC-W2-01 (wood)

} Northern exposure

A radiocarbon age and uncertainty were provided, which then was calibrated to account for the changes in the ^{14}C abundance in the atmosphere over a wide range of timescales, as a function of ocean circulation, solar effects, and geomagnetic field effects (the latter two controlling the production of the secondary thermal neutrons and the former controlling the temporary storage of ^{14}C in the ocean. The calibration software OxCal 4.4.4 was used for the calibration and to determine a more realistic age uncertainty than the AMS-based uncertainty reported by the AMS lab (Bronk Ramsey, 2009; Reimer *et al.,* 2020).

Figure 2.6. Radiocarbon sample NW-SMNRC-W-01, wood collected from the Northern Roadcut Exposure site.

2.6. Dendrochronology

Dendrochronology is using tree rings as which have a yearly resolution and can be used to date geomorphic events. Tree rings can be used to determine minimum ages of the surfaces on which trees are growing (Lawrence, 1946; Luckman, 1998; Koch, 2009; Koch *et al.*, 2014), accurately date events that damage or kill trees, and indicate sequential periods of movement. The precision of dendrochronology is annual or better. Dendrochronology utilizes the number of tree rings to ascertain how long that tree has been growing, for example, on surficial landslide deposits. Trees that are impacted by or grow on landslide material can record these events as irregularities in the thickness or geometry of one or more tree rings, possibly even at a sub-seasonal precision. This is seen in the case of leaning coniferous trees that exhibit thicker ring growth on their down-slope side due to a landslide, or other directional force (Fig 2.7) (Malik & Wistuba, 2012).

In the Kluane Lake region, tree assemblages primarily consist of white spruce, trembling aspen, and balsam poplar (Wang & Geurts, 1991). These boreal forests do not typically live long enough to help chronologically date surfaces as far back in time as the other, more absolute dating methods such as TCN dating, but they still can provide an accurate range within a historical context.

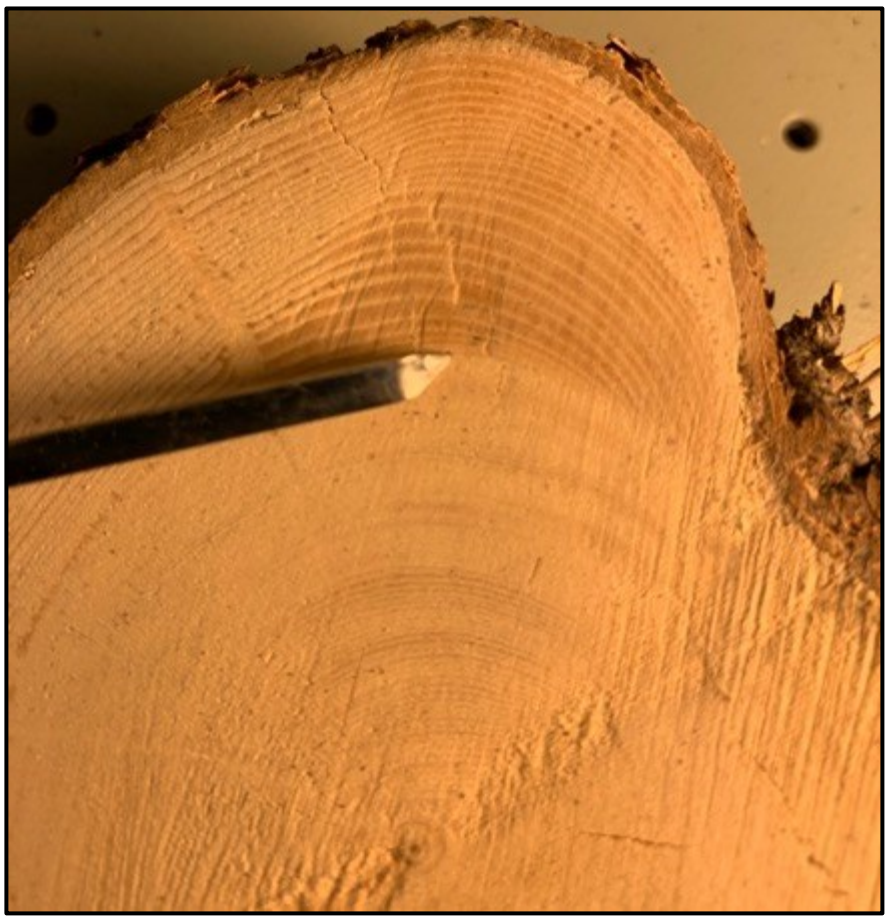

Figure 2.7. Sample NW-GNRC-LT-04. Tree rings were counted from the most recent ring to the beginning of the reaction wood. This was interpreted to be the point where the spruce was tilted, and thicker ring started forming on the lower side of the trunk.

Mass movement can also be recorded by the presence of tree scars. A prominent tree scar could potentially represent an impact event from a landslide (Fig. 2.8), a tree falling on it, or animal activity. Sampling from several trees may provide context and statistical precision for when the mass movement occurred. Walking around the perimeter of the landslide toe is important for dendrochronology as the presence of both leaning, pistol-grip, and scarred trees can help date the event. This will be described in Chapter 3.

Figure 2.8. Tree sample NW-GNRC-TS-02. This tree was sampled due to the evidence of an apparent impact scar (arrowed). This could be due to a boulder striking the tree during a landslide or other major impact. Pickaxe is 60 cm long.

Trunk discs were collected from living trees around the landslide deposit using a hand saw. Samples were then sent back to Simon Fraser University where they were sanded with incrementally finer sandpaper so the rings could be accurately counted; photos of these samples are found in Appendix D. Repetitive cycles of light and dark rings were counted as one season: a lighter, larger ring denoting stages of early growth (spring/early summer), and thinner, darker rings denoting late wood growth (late summer/fall) (Studhalter *et al.,* 1963; Hughes, 2002).

2.7. Tephrochronology - White River Tephra

The identification of the White River Tephra (WRT) throughout the study area assisted in relative age dating. This silty-sand ash layer originated from a Plinian-type eruption, producing northern and eastern lobes that spread from Alaska through to western Northwest Territories; roughly 150 km from the study area (Fig. 2.9) (Lerbekmo, 2008). Recent data have shown that some of this volcanic ash from the eastern WRT may have extended to Europe and Greenland where it can be correlated to the AD860

ash (Jensen *et al.,* 2014). The northern lobe has been dated to be ~1605-1805 cal years BP and the eastern lobe is 1170-1097 cal yr BP (Jensen *et al.,* 2014). These ages were calculated using volcanic stratospheric sulfur injections and aerosol optical depth measurements (Toohey & Sigl, 2017). The larger eastern lobe primarily covers the study area, but there is evidence of tephra from the northern lobe at Generc, although not directly observed in this study (Turner *et al.,* 2013). In the field, the ash layer has a “salt and pepper” appearance due to its primarily rhyodacitic and pumiceous glass composition with mafic minerals (Lerbekmo, 2008). Along the Alaska Highway, deposits can range from 0.02 - 0.8 m and grain sizes can be ~0.1 – 0.6 cm (Lerbekmo, 2008) (Fig. 2.10). Determining the presence of WRT on landslide deposits indicated a minimum age; this assisted with the relative age dating of the Sheep Mountain landslide as WRT was stratigraphically at the top of the deposit.

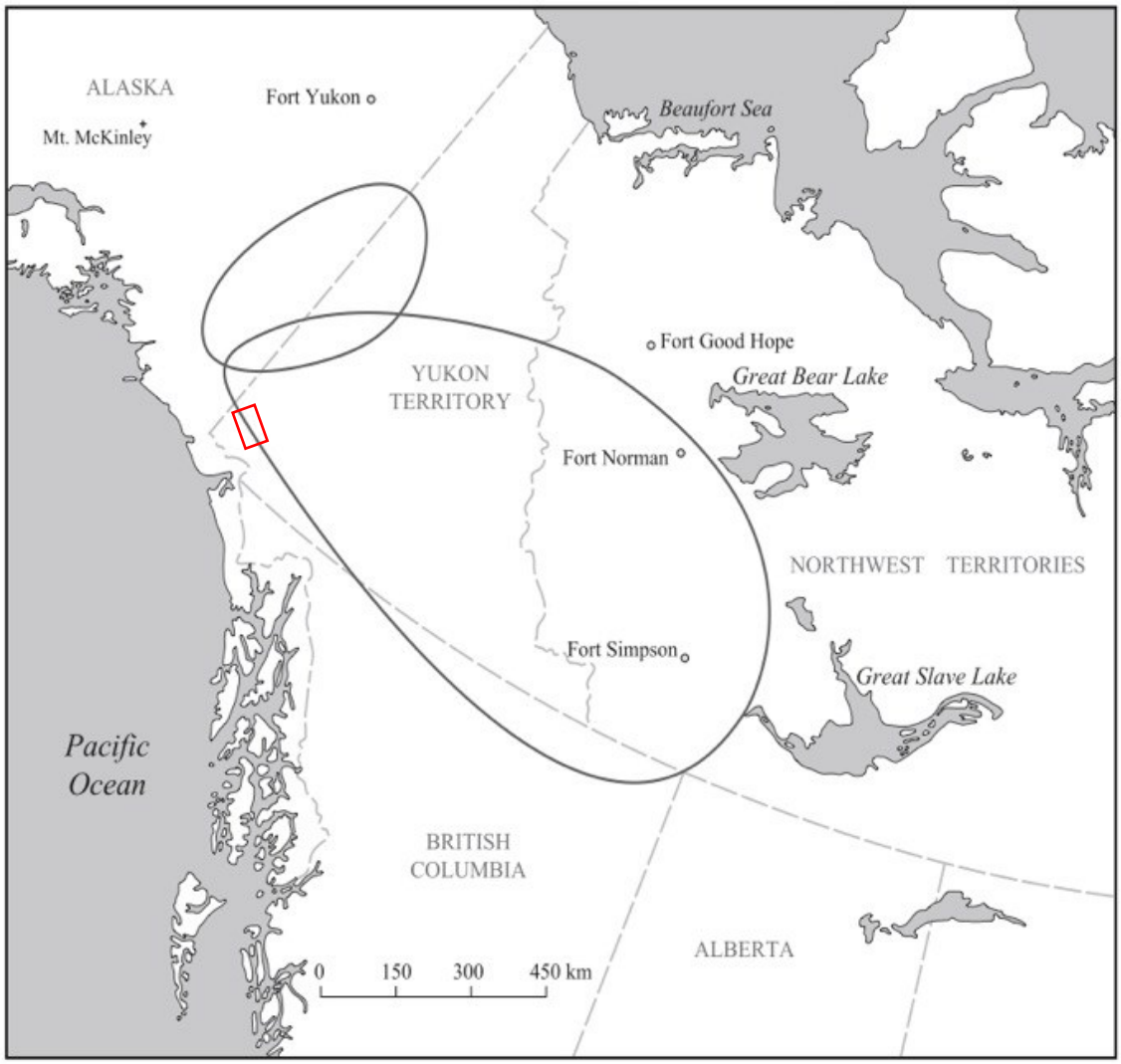

Figure 2.9. Extent of the northern (left) and eastern (right) WRT lobes. Study area shown is shown in the red square. Modified from Lerbekmo (2008).

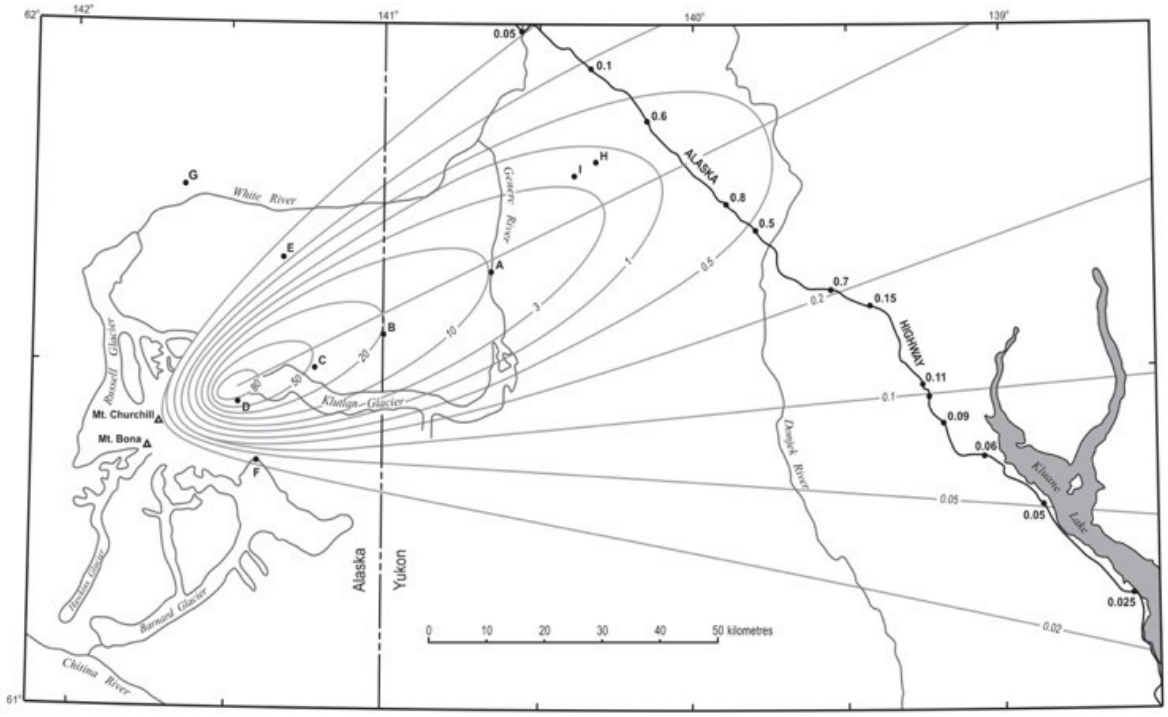

Figure 2.10. Isopachs indicating thicknesses of the eastern WRT lobe across the Alaskan-Yukon border. Letters A-I indicate areas where ash thickness was determined. Modified from Lerbekmo (2008). Around the study area near Kluane Lake, tephra thicknesses ranged from 0 – 0.5 cm.

2.8. Conclusion

TCN exposure dating has been instrumental to Quaternary reconstructions in a multitude of academic studies and in particular, landslide dating (Hewitt *et al.,* 2011; Sturzenegger *et al.,* 2015; Hilger *et al.,* 2018, Böhme *et al.,* 2019). In this thesis, most importantly is the application of TCNs to exposure dating of landslides around the Kluane Lake region. Combining the ages from TCN dating with those from radiocarbon dating will provide a stronger chronological constraint on the Sheep Mountain event. Mass wasting events, such as the Generc landslide which was too young to be dated through these alternate methods, provided the opportunity to utilize dendrochronology on the toe deposits. Using these dating methods, the chronology of landslides around the Kluane Lake region can be better understood. Age calculations at each site are further explored in Chapter 3 along with more detailed descriptions of the landslides and the uncertainty in each age.

Chapter 3. Landslide deposit chronology, Kluane Lake Region, Yukon

3.2. Introduction

Canada's largest mountains in southwestern Yukon are prone to large-scale rock slides and rock avalanches owing to over-steepened slopes from uplift and glacial erosion, proximity to active faults, and paraglacial conditioning (Ballantyne, 2002). Within this well-known, geomorphologically active region (Northern Climate Exchange, 2011; Koch *et al.,* 2014), the Kluane Lake region is a UNESCO World Heritage site (Parks Canada, 2019) and is experiencing rapid change through highway corridor modifications and expansion of fibre-optic networks. However, only a few of the most accessible large landslides have been investigated, and even fewer have been dated or assessed for triggering mechanisms. In the Kluane Lake region, it is necessary to evaluate the extent, timing, and cause of mass wasting events with sufficient runout or volume to affect people or property directly (burial) or indirectly (damming, floods, tsunamis). Assessing the nature of these hazards can contribute to the evaluation of risk in the area, as well as improving maintenance of existing infrastructure and developing building codes for future development.

3.2.2. Objectives

This study contributes to the evaluation and dating of selected landslides in the Kluane Lake region. Specifically, the objectives of this study are to use multiple geochronological techniques on five rock avalanches/rock slides throughout the Kluane Lake region to help refine their genesis and link them to known earthquakes or periods of Holocene climate change, *i.e.*, warmer and wetter conditions, or periods with potential permafrost thaw. The long-term goals of this study are to provide chronological and landslide characterization data that will contribute to future regional paleoseismology and landslide hazard assessments in the Kluane Lake region and Alaska-Yukon-northern British Columbia region.

3.3. Study Area

The Kluane Lake area is situated in southwest Yukon near the Alaska-Yukon border (Fig. 3.1). The area is a major transportation corridor and is subject to numerous mass-wasting events such as rock slides, rock avalanches, and debris flows (Clague, 1981). A variety of triggers have been proposed: over-steepened terrains due to glaciations, the thawing of permafrost, debuttressing of slopes due to relieved glacial stresses, and/or proximity to active fault lines (Hickman *et al.,* 1978; Lanphere, 1978; Haeussler *et al.,* 2004; Doser, 2014).

Sediments deposited from the recent glaciation, *i.e.*, the McConnell Glaciation (*ca.* 25-10 ka), also provided surficial material which can be remobilized as shallow-seated landslides (Bond, 2004). Surficial materials in the area are blanketed by the widespread White River Tephra (WRTe,1170-1097 cal yr BP (Jensen *et al.,* 2014)). The WRT directly observed in the study area during the 2019 field season primarily originates from the eastern lobe of a Plinian eruption in southeastern Alaska (Lerbekmo *et al.*, 1975; Lerbekmo, 2008). Although the northwestern part of the study area was likely affected by the northern lobe (Lerbekmo, 2008).

The study area is situated near the eastern portion of the Denali Fault System (DFS) (Fig. 3.1). The southernmost portion of Kluane Lake is near the junction between the Eastern Denali and Duke River faults. The Denali Fault is an active, intracontinental, dextral strike-slip and thrust fault system that extends southeast from Alaska, through Yukon, and into northwestern British Columbia (Hickman *et al.,* 1978; Lanphere, 1978; Haeussler *et al.,* 2004; Doser, 2014; Cobbett *et al.*, 2017). Its activity is largely attributed to the accretion of the Yakutat Terrane into the North American plate at a rate of ~50 mm/yr, and some of the resulting strain is accommodated on the Denali fault system and related faults in the St. Elias Mountains (Clague 1979; Mazzotti *et al.,* 2002; Hyndman *et al.*, 2005; Christeson *et al.,* 2010). In southwestern Yukon, strain manifests prominently as displacements along strike-slip faults between the St. Elias Mountains and the Shakwak Trench, southwest of Kluane Lake.

A limited number of paleoseismic interpretations for the region have been made from trench exposures, lake core data, and bluff observations adjacent to the Denali fault (Blais-Stevens *et al.,* 2020). Additionally, colluvial wedges in trenches and other scarp

measurements have been used to determine fault kinematics and slip rates in an attempt to understand changes in deformation rates over time (*e.g.* Seitz *et al.,* 2008). Some of these trenches have been re-excavated and re-examined by Natural Resources Canada (NRCan), which led the discovery of additional seismic events (Blais-Stevens *et al.,* 2020).

The Kluane Lake region is topographically susceptible to large landslides, which is evident along the Alaska Highway. The five landslides examined in this project are: (1) Sheep Mountain, (2) Aishihik, (3) Gladstone-1, (4) Gladstone-2, and (5) Generc (Fig. 3.1). Given the knowledge gap in both the unknown nature and age of landslide deposits in the study area, the focus of this thesis will be to contribute critical information about large scale rock slides in the Kluane region. Since there are several triggering factors which could account for the initiation of mass wasting events in the study area, we selected several rock slides based on their proximity to active faults, their large volume, the presence of viable boulders for the TCN method, and their accessibility to try and ascertain which mechanism was in action. While some events are not within the immediate vicinity of the lake, for the sake of simplicity the study area is referred to as the Kluane Lake area (KLA).

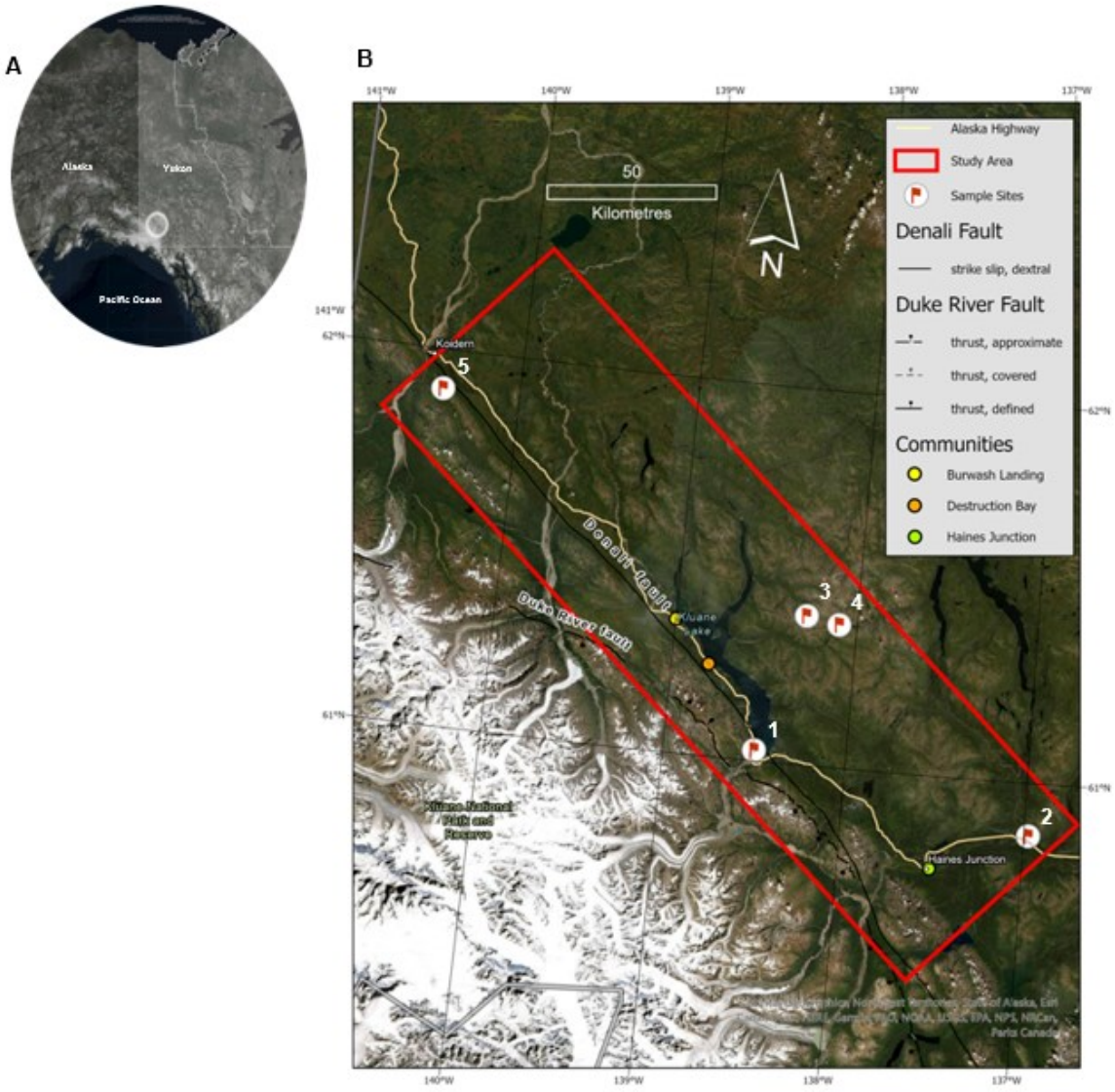

Figure 3.1. An overview of the Kluane Lake study area using Arcpro. (A) A worldview image of the KLA in southwest Yukon, the study area is shown in the highlighted circle. (B) A closer image of the study site and selected landslides in the red rectangle (1 - Sheep Mountain; 2 - Aishihik; 3 – Gladstone-1; 4 – Gladstone-2; 5 – Generc).

3.4. Geochronometric methods

Several dating techniques were used in this project to provide a chronologic framework: terrestrial cosmogenic nuclide (TCN) exposure dating, radiocarbon dating, dendrochronology, and tephrochronology. Eighteen terrestrial cosmogenic samples were collected from the flat tops of large boulders on four targeted landslide deposits. They were prepared into targets of BeO and $AgCl_3$ at the Cosmic Ray Isotopes Sciences Lab at Dalhousie University (CRISDal) and later analysed at Lawrence Livermore Nuclide Laboratory in California and PRIME Lab in Indiana, respectively. The exposure ages were calculated using the online calculators formerly known as the CRONUS-Earth online calculators (Balco *et al.*, 2008). Four samples for radiocarbon dating consisting of twigs and wood were analyzed at Keck Carbon Cycle AMS Facility and calibrated using University of Oxford's OxCal 4.4.4 program (Bronk Ramsey, 2009; Reimer *et al.,* 2020). Dendrochronological samples were prepared and measured at Simon Fraser University.

3.4.2. Terrestrial Cosmogenic Nuclide (TCN) Dating

Boulders for TCN dating were sampled at four landslides. TCN dating was chosen because of its wide application for dating landslides (*e.g.* in Canada: Sturzenegger *et al.*, 2015; in glaciated regions: Hilger *et al.,* 2019; and in tectonically active regions: Hewitt *et al.* 2011), the relative ease of finding suitable sample media, as well as my and my collaborator's previous experience with the technique. When possible, a sampling transect on the landslide deposits was performed to obtain as broad a dateable section as possible. For example, at the Sheep Mountain event, four samples were collected from each of the two proposed phases to determine if there were any statistical differences in their ages. A transect was also performed at Aishihik where two separate landslide ridges were sampled to determine any age differences. Two nuclides of interest were isolated from boulders collected from the four sites: ^{10}Be in quartz from the Aishihik and Gladstone areas, and ^{36}Cl in feldspars and magnetite from the Sheep Mountain event. The difference in choice was solely based on quartz abundance. We prefer ^{10}Be in quartz in areas with long periods of snow cover because snow modulates the thermal neutron production of ^{36}Cl in complex ways (Dunai *et al.,* 2014; Delunel *et al.*, 2014). However, there are many recent studies that suggest the two isotopes yield equivalent ages on the same landform (*e.g.*, Margold *et al.,* 2019) when

the thermal neutron-production component of ^{36}Cl is minimized by using minerals with low ^{35}Cl abundance.

As with most geochronological methods, sample selection is an essential part of TCN dating. Field observations for interpreting the exposure ages included topographic shielding gradients measured using a compass and inclinometer. Despite using a stringent sampling strategy to sample the highest and flattest boulders in the deposits, additional observations were recorded to evaluate uncertainty associated with boulder morphology and position (neutron loss, self-shielding, evidence of erosion, potential for shielding by snow, moss and trees), erosion rates of the boulder and landslide deposit, and spatial orientations of samples (i.e strikes and dips of sampled boulder surfaces). Multiple exposure ages (minimum of three boulders) from each landslide deposit were obtained to assess the possibility of TCN inheritance (Hilger *et al*., 2019), frost-heave of the boulder, exhumation of the deposit, and/or post-slide rockfall onto the deposit. All calculated ages had an internal (total precision) and external (random and systematic) error calculated with 1σ precision (kyr). The reduced field, chemical, and AMS ^{10}Be data were interpreted as ages using online calculators formerly known as the CRONUS-Earth online calculators (Balco *et al.*, 2008), specifically (Version 3.0 CRONUS Calculator on the University of Washington server) and production rates were scaled using the Lifton-Sato-Dunai (LSD) method (Lifton *et al.,* 2014). Similarly, the ^{36}Cl data were interpreted as exposure ages using the KU CRONUS-Earth ^{36}Cl exposure age calculator (Version 2.0, Marrero *et al*., 2016a) after being summarized in a ^{36}Cl data reduction sheet provided by S. Marrero and J. Gosse, with production rates according to Marrero *et al.* (2016b) as modified by Marrero *et al.* (2021) and using the 'Sato' scaling option. The shielding and erosion corrected ages are provided in Table 3.1 with 1σ uncertainties.

3.4.3. Radiocarbon Dating

Radiocarbon dating is the most common dating technique utilized in late Quaternary studies since its advent in the late 1940s (Libby, 1954; Clague *et al.*, 1982). Organic samples extracted from within the Sheep Mountain landslide deposits, such as woody material, were collected in 2019. Samples were kept cold in the field and were frozen once back at Simon Fraser University to avoid the growth of mold and fungus. Modern root growth was a potential contaminant, producing younger ages than the deposit. Thus, it was important to remove as many modern roots as possible. Samples

were prepared at Simon Fraser University for further processing at Keck Carbon Cycle facility in California. There, samples were treated with 1N HCl:1N NaOH at 75°C in a typical acid-base-acid procedure prior to combustion (Berglund & Ralska-Jasiewiczowa, 1986; Olsson, 1986). Samples were then run through Keck-CCAMS facility's 500 kV compact AMS unit. Radiocarbon concentrations were provided as fractions of the modern (Fm) standard, $D^{14}C$, and assigned a conventional radiocarbon age following the conventions of Stuiver and Polach (1977) (Table 3.2). The ^{14}C ages were then converted to calibrated years using a probabilistic method against the IntCal 20 curve within 2σ error (OxCal v4.4.4; Reimer *et al.,* 2020). While it is possible that some of the dated material was dead (no longer exchanging with the atmosphere) prior to the landslide event, the reproducibility of different samples from a given landslide, and their agreement with TCN exposure ages suggest this was not a major effect in the study sites.

3.4.4. Dendrochronology

Dendrochronology is the study of annual rings in trees. Tree ring records are essential proxies in fields such as paleoclimatology, archaeology, and geomorphology (Bradley, 1985; Torbenson *et al.,* 2016). Dendrochronological samples were collected at the Generc landslide deposit because of the relatively young age of the event based on vegetation type and cover. This dating method was also employed because TCN concentrations may have been too low for high precision ages and radiocarbon ages would have been post-bomb pulse (Day & Fan, 1986; Reimer *et al.,* 2004). Samples were collected from spruce by traversing the perimeter of the toe of the deposit to determine if any trees had been impacted by the event (Fig. 3.2). The extent of the deposit was determined by a change in vegetation from a younger, less mature growth (*e.g.,* alders) to a more established growth (*e.g.,* conifers) (Geertsema & Pojar, 2007). Evidence of impact, such as leaning (sample ID ending in LT), or scarred trees (sample ID ending in TS) were sampled using a handsaw. Disks were then sanded using incrementally finer sandpaper at Simon Fraser University following the method of Dukpa and Tenzin from Ugyen Wangchuck Institute for Conservation and Environmental Research (UWICER, 2017).

Figure 3.2. Landslide outline of the toe deposit, Generc. Tree disks were collected at three sites: GNRC-TS-03, GNRC-TS-02, GNRC-LT-04. The light green deciduous vegetation indicates the extent of the landslide and the related downstream disruption.

Rings were counted using a binocular microscope to determine the age of tilting/scarring. One year of growth consisted of a lighter ring with larger cells representing growth in spring and summer and a darker, denser zone of smaller cells representing growth in fall (Filion *et al.,* 1986) (Fig. 3.3). Leaning trees around the periphery of the deposit were sampled if it appeared that they were impacted and tilted during the emplacement of the landslide. Timing can be determined by the initiation of thicker, dark rings, known as compression wood, as the tree tries to right itself. If the impact abrades the bark, a scar forms; rings then start to grow over the scar, and by counting back to the start of this process, an age can be determined. Trees can be tilted and scarred by other processes such as windthrow, windstorms, permafrost growth and degradation, and animals; therefore, multiple samples need to be taken. These ages are analyzed in the following section (Table 3.3). The number of rings counted is approximate within one or two years due to some degradation and pitting caused by mold which made them more difficult to discern. The error in age approximation also carried over to the year of impact estimate and was off within a year or two.

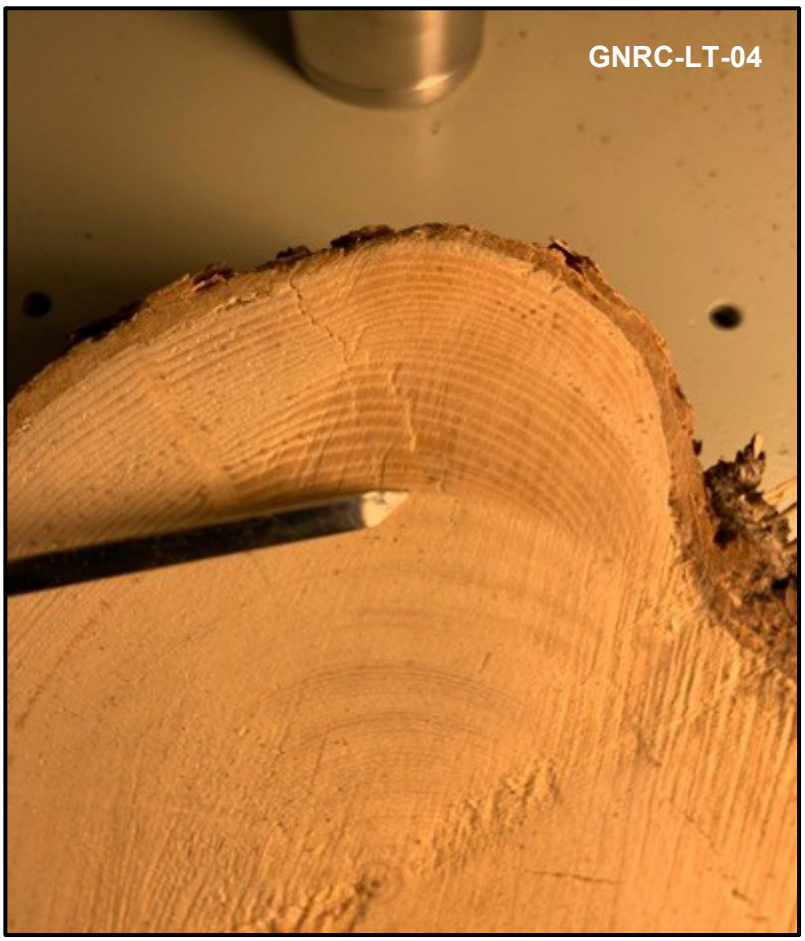

Figure 3.3. Sample GNRC-LT-04. Eccentric growth is prominently displayed as increasing ring thickness on this side of the tree. These darker rings are called compression wood. The tip of the metal poker points to the initiation of this preferential growth and was most likely around the time that this tree began to tilt. Two different coloured rings denote one growth cycle.

3.5. Previous Work and Landslide Descriptions

Five landslides were analyzed for this project: Sheep Mountain, Aishihik, Gladstone-1, Gladstone-2, & Generc. Each site was selected through literature review, air photo analysis, desktop mapping, and ground truthing. Detailed description of each site and any exposures examined at these locations are described in the following sections.

3.5.2. Sheep Mountain Rock Avalanche

The Sheep Mountain rock avalanche (61.03° N, -138.50° W) occurred sometime in the late Holocene when exposed metavolcanic rocks along the western –

northwestern face of Sheep Mountain collapsed (Clague, 1981) (Site 1 - Fig. 3.1). This was based on the relative freshness (*i.e.*, by the relative degree of surface roughness) of the event as compared to an older landslide which would be more eroded by soil and hydrological transport (McCalpin, 1984; Garriss, 2019). The landslide has an approximate volume of ~5-10x10^6 m^3 and is classified as a rock avalanche based on size and degree of fragmentation of the blocks on the deposit. Rock avalanches undergo rapid fragmentation and experience longer runouts than would be expected of events with comparable volume, but are composed of granular material (Hungr *et al.,* 2014; Brideau & Roberts, 2022). Clague (1981) suggested it formed in two distinct phases. Clague conducted radiocarbon analyses on a pith from a dead tree trunk rooted in the younger phase (490 $\pm$ 50 ^{14}C yr BP – 563-456 cal yr BP) where the toe pushes into Kluane Lake as well as from wood from underneath the older deposit (1950 $\pm$ 50 ^{14}C yr BP – 1992-1741 cal yr BP). This provided a preliminary minimum and maximum age bracket of the Sheep Mountain slide that was narrowed down in this project.

To verify the ages and interpretation of two events, we used ^{36}Cl boulder exposure ages and radiocarbon dated wood above and below the landslide. The boulders sampled are shown with respect to the approximate outlines of the proposed younger and older phases (Fig. 3.4). Two exposures were described and sampled for radiocarbon analysis: the Northern Road Cut (NRC) and Soldier's Pass (Figs. 3.6 and 3.7 respectively). Photos taken from a helicopter and drone provided high resolution imagery to better delineate the potential source area of the event and the features of the landslide.

The debris field consisted of large, unweathered boulders that are scattered across the ~3 km^2 deposit. The outer edges of the slide appeared to be more subdued with a smoother appearance and more loess cover on and between the blocks than in the medial portion; therefore, it was presumed to be older (Clague, 1981). The outer portion also contained more vegetation, suggesting an older surface. Forest growth flanked the northern and southern borders of the event, which also helped to define the morphology of the toe. The primary lithology present at this site were fine-grained metavolcanics with secondary, green mineral production along slickenlines.

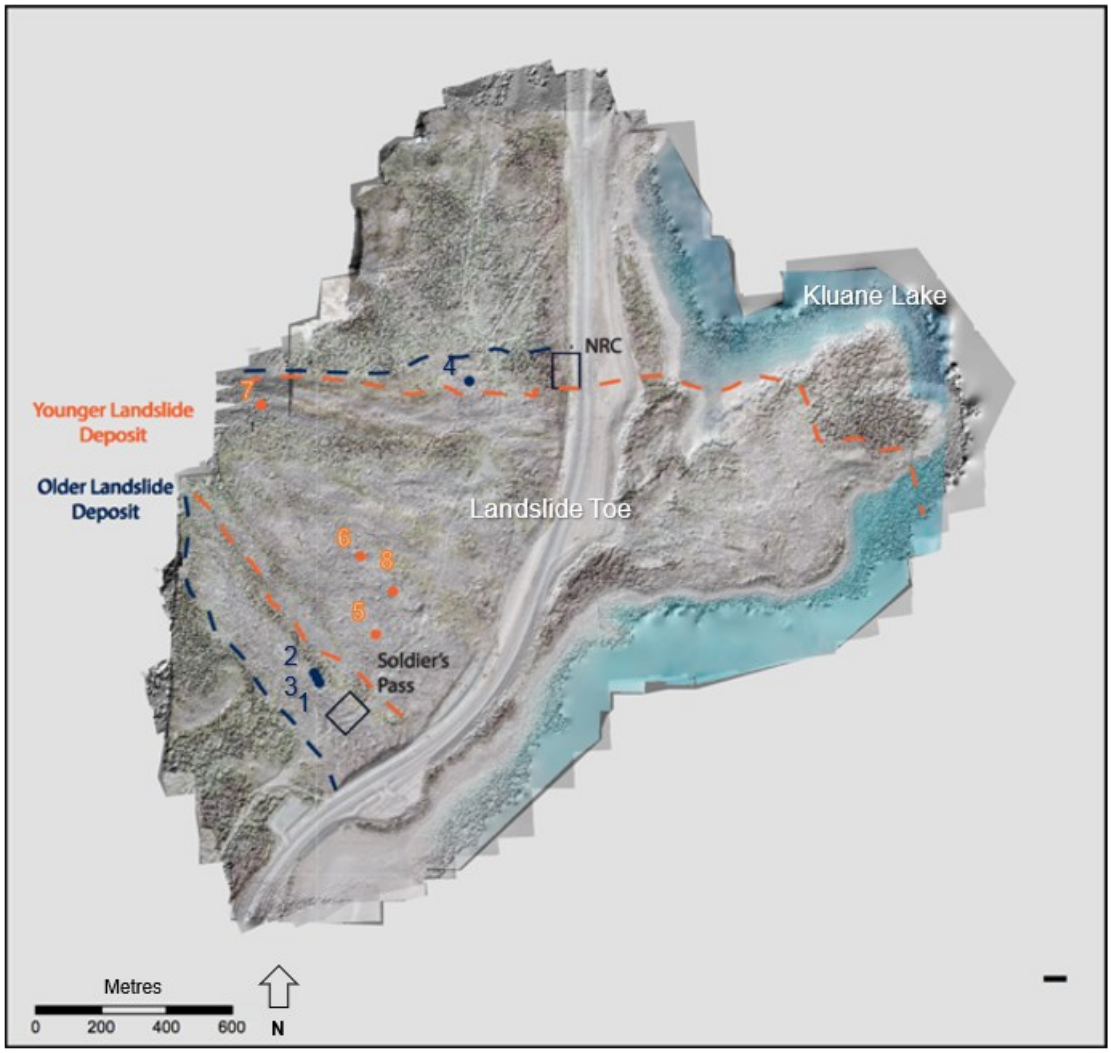

Figure 3.4. Orthographic imagery overlying DEMs from the toe of the Sheep Mountain Landslide. The two proposed phases are outlined, the older deposit (blue) and the younger deposit (orange). Circles denote locations where boulders were sampled for TCN dating. Numbers correspond to samples: (1) SM-OLS-01, (2) SM-OLS-02, (3) SM-OLS-03, (4) SM-OLS-04, (5) SM-01, (6) SM-02, (7) SM-03, (8) SM-04. Boxes indicate radiocarbon sampling sites (NRC – Northern Road Cut).

The likely source area is roughly 730 m above and 2.2 km from Kluane Lake (Fig. 3.5 A) (Clague, 1981). Once out of the confines of the more steeply sloped valley walls (~20°), boulders fanned out on shallower slopes at the base of Sheep Mountain, averaging an 11° slope from the lake to the entrance of the feeder gully. A portion of the slide enters nearby Kluane Lake 700 m north of where Slim's River delta enters the lake (Fig. 3.5 C). Parts of the deposit form alternating small-scale ridges and troughs ranging from 3-10 m high that run parallel to the transport direction. These ridges and troughs were not as pronounced on the portion that entered the lake, where it is more hummocky. Sparse vegetation, primarily conifers, grow between the blocks of the

deposits, mainly within the troughs. Blocks ranged from <1 to 5 m and were very angular with some fragmentation on their surfaces (Fig. 3.5 D). There did not appear to be any trends in block sizes on the surface of the deposit, but they were substantially larger than the more comminuted lithic fragments underlying the deposit exposed in road cuts

on the northern and southern margins of the slide. There did not appear to be any obvious continuous motion or creep of the boulders.

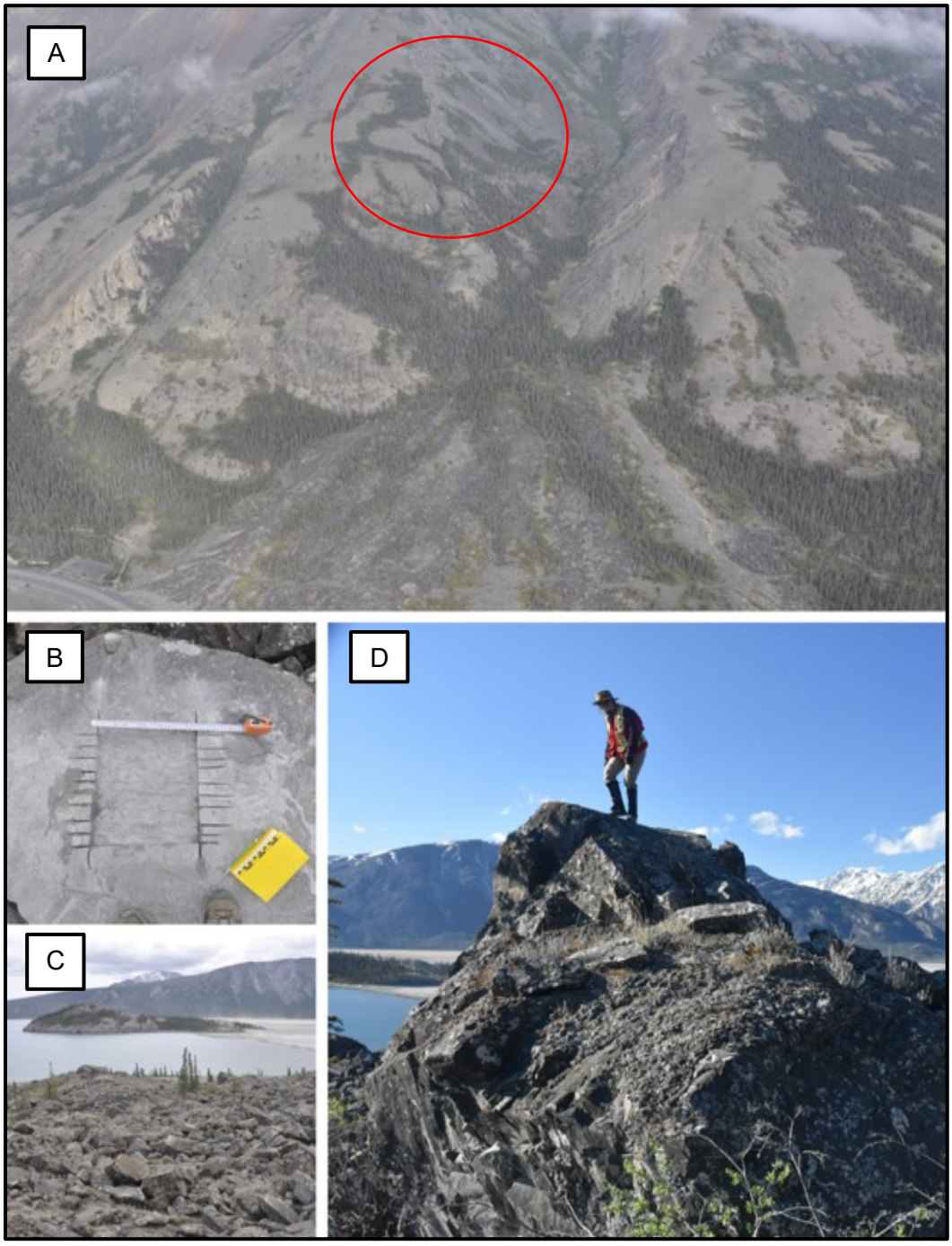

Figure 3.5. Sheep Mountain Landslide. (A) Helicopter view of the Sheep Mountain landslide, looking NW. The area circled in red is the proposed failure scarp (B) A typical TCN boulder sample site. (C) Large blocks on the surface of the slide, viewing east towards Kluane Lake. To the right, the fringes of the Slim's River delta are visible as it enters the lake. (D) Boulders at this site were larger than any other sampled landslide (sample NW-SM-03).

Northern Road Cut

This steep exposure had two primary units visible: a lower gravel/diamicton unit with organic layers and lenses and an upper blocky unit with large clasts. The underlying deposits were roughly up to 8 m thick, but this varied laterally, thinning towards the northern end of the exposure. The upper blocky unit was ~2-4 m and varied laterally with an irregular lower boundary and thinning towards the outer margins of the landslide (Fig. 3.6 B).

Lower Unit – (Proposed Alluvial Fan with Debris Flow Deposits and Organics)

This unit is poorly sorted to unsorted and matrix supported with a matrix of silty sand. Clasts are 5-20 cm in diameter, comprise 10-15% of the unit, and are rounded to subangular. Bands of weak paleosols, roughly a few decametres thick appeared as lenses within these deposits (black dashed lines, Fig. 3.6 B). The lower paleosol appears much more consolidated and darker. Moving towards the centre of the exposure, the thickness of the overall unit increases, and in places some of the beds within the unit are lenticular. Towards the northern outer margin of the exposure, organic beds converge and are better preserved, most likely due to the decreasing erosive strength of the overlying colluvial unit. Organic layers near the top of the unit provided suitable woody material for radiocarbon dating (Samples: NW-SMNRC-W-01, NW-SMNRC-W2-01) (Table 3.2). Burrows were also found in this unit and were trending out-of-slope towards the road. This was comparable to the previous description by Koch *et al.* (2014). This unit was previously described as three debris flows that were interspersed with organic deposits (peat, woody material, and modern roots); organics suggested periods of quiescence along the fan that were later inundated by debris flows (Clague, 1981; Koch *et al.,* 2014). Radiocarbon ages of soils between the lowermost and second lowermost units returned a result of 2,025 ± 20 ^{14}C yr BP, ages from *in-situ* roots between the middle and uppermost units returned a result of 1,910 ± 20 ^{14}C yr BP, and ages from a branch between the uppermost debris flow unit and rock avalanche unit returned a result of 1,920 ± 20 ^{14}C yr BP (Koch *et al*., 2014).

Upper Unit – Landslide Deposit

The upper unit is up to 5 m thick, clast supported and consists of blocky, angular clasts ranging from 1 to 70 cm with metavolcanic clasts that have reddish hues closer to the top and greener hues towards the base of the unit. The lower contact is sharp and

irregular. Overall unit thickness increases to the south. Overlying this unit are modern organic-rich loess and soil. Clasts in the unit are smaller than those in the colluvial unit at Soldier's Pass. White River Tephra is observed near the top of the exposure (found near the organic site 3, Fig. 3.6 B) A wavy band of shrubby vegetation growth is present 2-4 m below the top of the exposure which may be indicative of finer grained zones within this unit, material conducive for plant growth (green dashed line, Fig. 3.6 B). Plant growth is denser near the outer margins of the exposure.

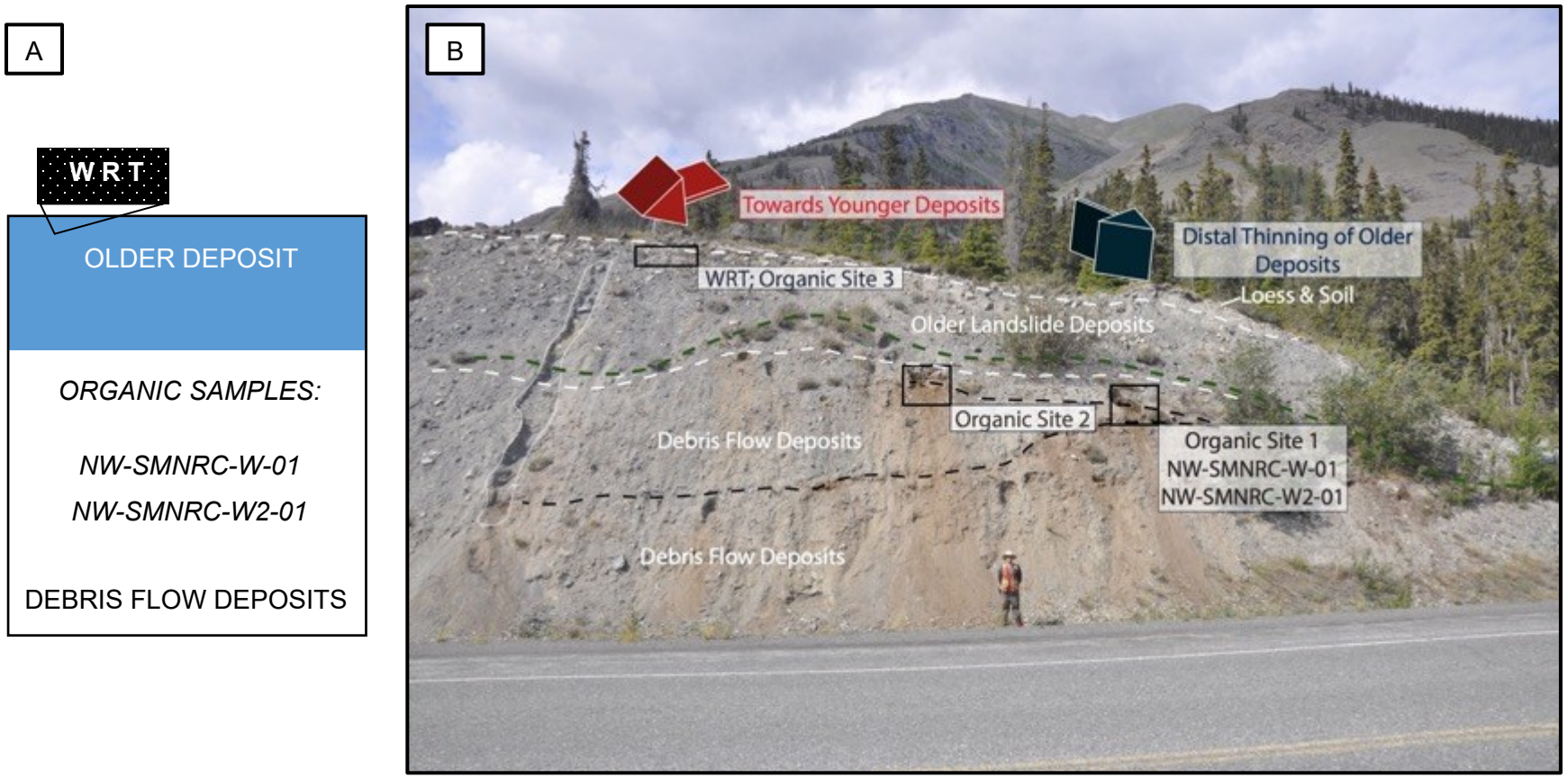

Figure 3.6. The Northern Roadcut exposure. (A) a simplified schematic cross section of the exposure. Organics sampled here include NW-SMNRC-W0-01 and NW-SMNRC-W2-01. These were underlying the older phase of the landslide and interfingering the debris flow/fan deposits. These were presumed to be buried forest deposits. (B) A more detailed outline of the exposure. The black dashed line represents organic layers mixed in with debris flow deposits. The dashed green line represents a vegetation line found across the exposure; the growth of vegetation can be indicative of the material type/size of the substrate on which it grows as it requires a more porous, loosely consolidated environment for roots to permeate. WRT was found near the top of section (near organic site 3). Thick blankets of modern loess and soil are found overlying the older deposit, further implying that this unit has been present for some time. Human for scale (189 cm).

Soldier's Pass Section

Approximately 800 m southwest of the northern roadcut, this trail-cut section (2.6 x 2.0 x 1.2 m) was analyzed to determine the minimum limiting age of the proposed older phase (Fig. 3.7). Looking southeast, this exposure is oriented toward 170° and contained two units: a lower unit which consisted of clast-supported blocks and an upper unit that was a highly variable zone of loess, peat, and angular, unconsolidated clasts. The upper unit was approximately 2 m thick, and the lower unit was >1 m at this site, but thickened upslope to the west.

The lower unit consisted of angular clasts ranging from ~30 cm to 2 m and were of a similar metavolcanic composition as the blocks on the surface. Blocks were generally smaller in size than those exposed at surface. The upper unit consisted of alternating beds of silt, peat, soil, and poorly sorted, angular deposits ranging from 10 – 50 cm thick. These beds were sometimes planar but had mostly wavy contacts; they also gently dipped downslope towards Kluane Lake. Peat layers in this mixed zone are also darker brown towards the base of the exposure and become lighter up the exposure. Brown sandy silt resembled the modern-day loess found overlying adjacent boulders. Angular clasts in the mixed zone were more rounded and smaller (~1-20 cm) than the underlying unit. The unit was matrix-supported with a sandy matrix and contained lithology like the surrounding metavolcanic blocks. An isolated patch (~20 cm long, 1-2 cm thick) of White River Tephra was observed ~30 cm from the surface of the exposure (solid black line, Fig. 3.7 B). Its distinctive sandy texture and salt and pepper colouration made it stand out against the browner, finer-grained mixed zone sediments. Smaller blebs of WRT were also detected to above the primary tephra. The lower boundary of this unit was undulatory. A thicker bed of more fibrous peat can be found overlying the older phase unit, where organic samples NW-SM-RC-01, NW-SM-RC-02 were collected, and then becomes more fibrous up the section (green circle, Fig. 3.7 B).

The presence of peat intermixed with colluvium/slope wash suggests that there may have been organic growth that was mixed with colluvium from the slopes to the west. At this site, there is evidence that underlying organics were mixed with slope wash as there is peaty material and what appears to be oxidized soils between the colluvium in the mixed zone.

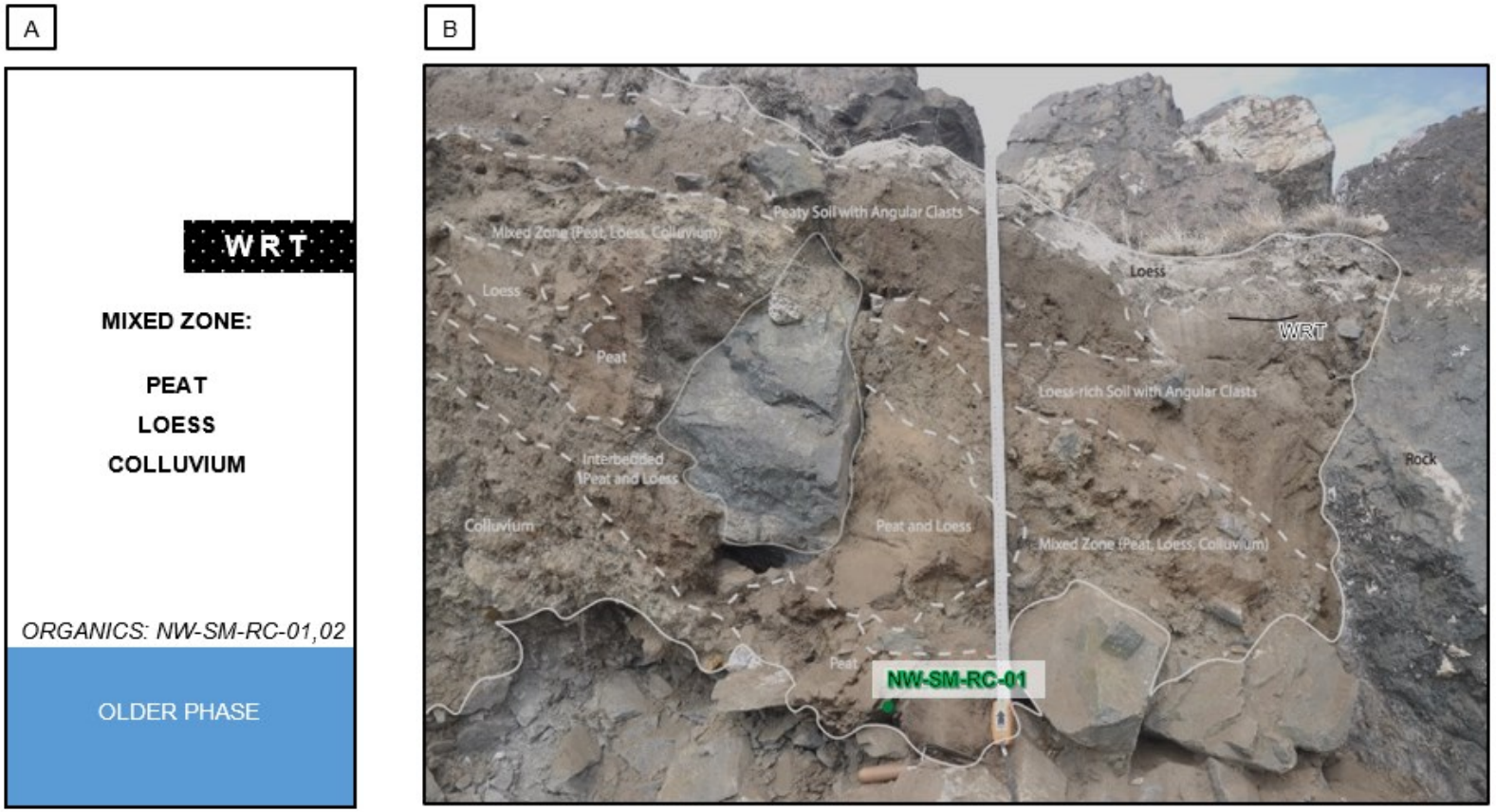

Figure 3.7. Soldier's Pass Section looking WNW. (A) A simplified cross section of the sediments found at the section. (B) View of exposure showing the interfingered nature of the sediments overlying the older colluvial deposits. The mixed zone contains varying layers of loess, peat, and colluvium. Organics were sampled as close to the interface between the older phase and mixed zone. WRT denotes the area where diffuse White River Tephra was found; the presence of WRT overlying the lower unit substantiates the age estimates put forth by Clague (1981) that the older phase is at least 1950±50 ^{14}C yr BP old. Organics (twigs) were also collected for radiocarbon dating (ID: NW-SM-RC-01/2, Table 3.2)

3.5.3. Aishihik Rock Avalanche

The Aishihik landslide (60.86° N, -136.97° W) is located in the eastern portion of the study area. (Site 2 – Fig. 3.1). This landslide has an estimated volume of $22x10^6$ m^3 and covers approximately 5.3 km^2 and is classified as a rock avalanche due to its large volume and high degree of fragmentation (Hungr *et al.,* 2001; Brideau *et al.,* 2005) (Fig. 3.8). The debris field is hummocky and overlies glaciolacustrine deposits (Huscroft *et al.,* 2004). A lobate toe deposit extends a kilometre into the valley bottom with an average slope of 4° and is ~0.75 km wide. Two prominent ridges run parallel to the transport direction, have a ~10 m difference in elevation between them, and are separated by a central depression that extends approximately 300 m. These two ridges, the east and west ridge, have coniferous trees that grew between the blocks (Fig 3.8). The source is located on an unnamed mountain on the northern side of the Takhini Valley, east of the Aishihik River, and ranges between 250 – 300 m in elevation above the base of the slope. The main failure slope has an average slope of 37° (Huscroft *et al.,* 2004). There did not appear to be any difference in landslide or boulder morphology between these two ridges. We are aware that rock avalanche events can produce levee-type ridges along their periphery, so the presence of these ridges does not necessarily indicate multiple depositional events. Aishihik provided an ideal site for TCN dating as this rock slide consists of primarily large, angular, quartz-rich gneissic blocks sourced from the Kluane metamorphic assemblage (Huscroft *et al.,* 2004) (Figs 3.9 A, 3.9 C).

Glacial Lake Champagne paleoshorelines occur to the north (Figure 3.8); this lake reached its largest extent sometime between 13.66 and 9.50 kyr ago (Hughes *et al.,* 1989; Barnes, 1997; Gilbert & Desloges, 2005), and was dammed against the slopes of the mountain by glaciers (Brideau *et al.,* 2005). The landslide postdates the incursion of the glacial lake. Brideau *et al.* (2005) proposed that this failure was triggered by preferentially degraded rock masses in the head scarp caused by intersecting fault sets; this structural weakness could have been enhanced by glacial debuttressing and slope undercutting.

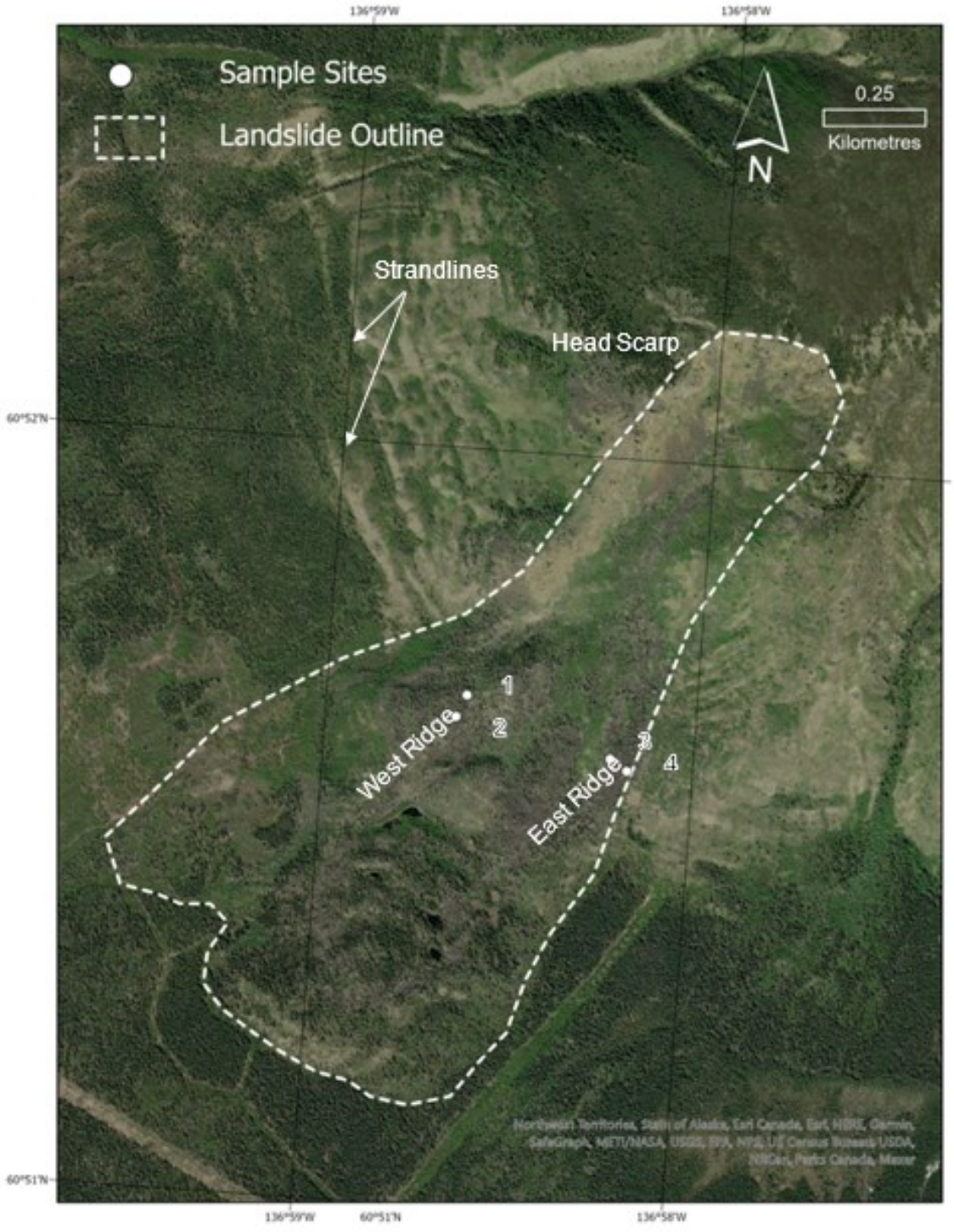

Figure 3.8. Arcpro imagery of the Aishihik landslide. Four samples were obtained from two ridges on the landslide deposit, two on the west 1 (A-01, A-02) and two on the east ridge (A-03, A-04). Paleoshorelines are prominent to the NNW of the event and are from Glacial Lake Champagne (Gilbert & Desloges, 2005).

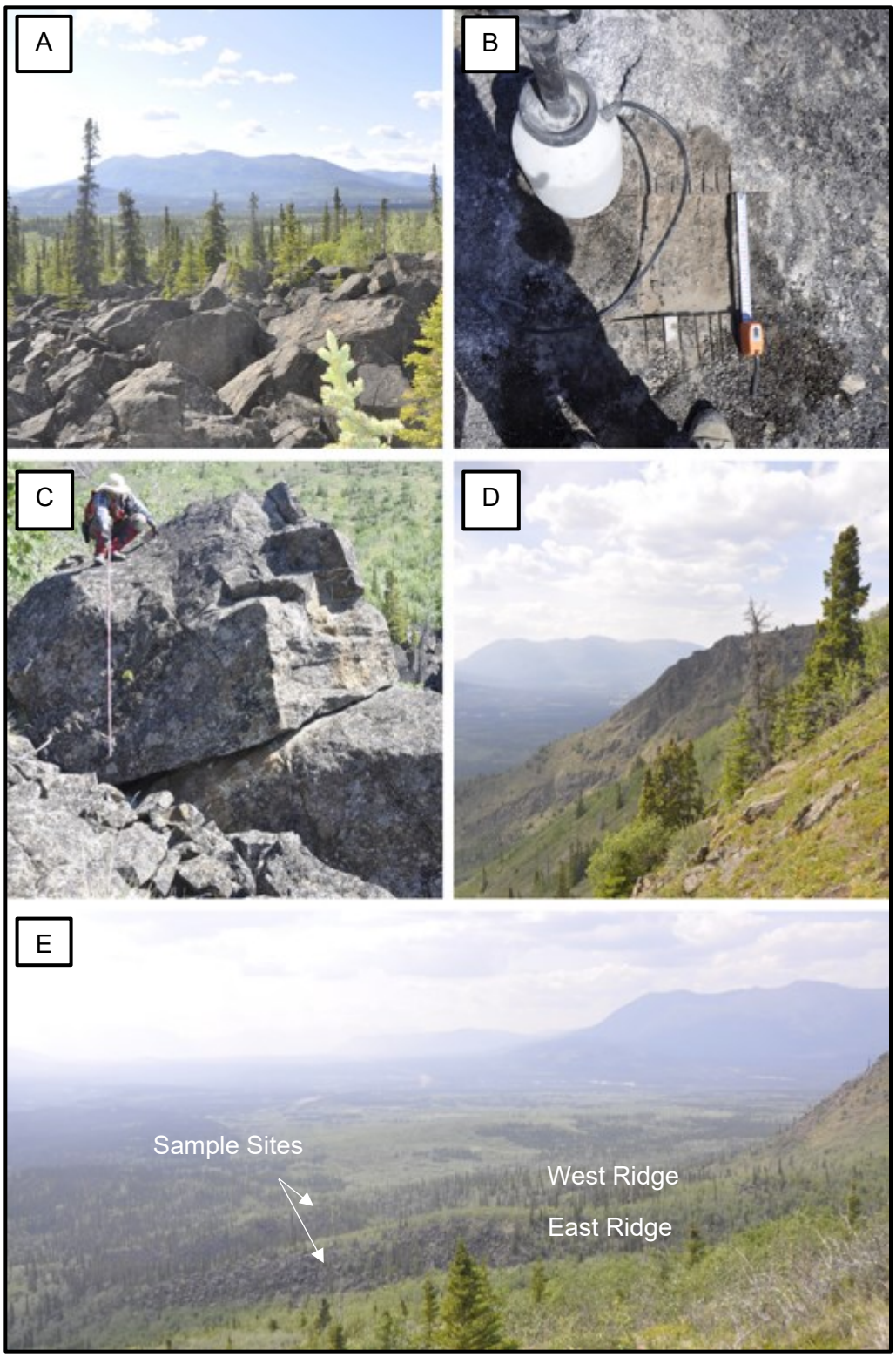

Figure 3.9. Aishihik Landslide. (A) Gneissic boulders on the landslide surface; sparse vegetation occurs on the landslide. (B) An example of a TCN sample taken from a landslide block. (C) Some blocks found within this failure were up to 3 metres tall (Sample NW-A-03). (D) Approximate position of the proposed source zone, looking NW. (E) The two lateral ridges present at this site separated by a depletion zone.

3.5.4. Gladstone Area

Two landslides in the Gladstone area were investigated and sampled to the north of Kluane Lake in the Ruby Ranges; Gladstone-1 (61.4° N, -138.3° W) and Gladstone-2 (61.4°, -138.1°W) (Sites 3 and 4 – Fig. 3.1). Both failures consisted of Bt-Hbl granodiorite, the prominent lithology of the Ruby Range Batholith (Cairnes, 1915). Both events occurred in glacially carved valleys: Gladstone-1 initiated in a cirque valley and Gladstone-2 initiated on the steep slopes of the Gladstone Lakes meltwater corridor. Based on the area of the landslide and the empirical relationship derived by Guzzetti *et al.* (2009), Gladstone-1 has an approximate volume of 1.4×10^7 m^3 and Gladstone-2 has an approximate volume of 5.0×10^6 m^3.

Gladstone-1 Rock Slide

The furthest north of all sampled sites, this NNW-facing rock slide has an approximate area of 0.5 km^2 originating from a head scarp ~0.5 km in elevation above the toe and slopes ~25-30° down towards the centre of the cirque (Fig. 3.10 A). The debris field then changes to a gentler slope (5-6°), as it progresses downslope, roughly 0.85 km from the failure source. The arcuate head scarp is visible on the southeast portion of the cirque wall (Figure 3.10 A) and is also visible in satellite imagery. There was no evidence of channelized material, and the deposit of the toe consists of hummocky blocks (Fig. 3.10 B). Block sizes ranged from 0.5 up to roughly 3 m and were angular with prominent weathering along boulder faces. There did not appear to be any size differences of boulders on the deposit or tree growth on the deposit itself. Some moss coverage was present which could potentially increase weathering rates due to increased acidity, but this is most likely negligible at this site. Based on surficial geology maps of the area, the landslide terminates above MIS 2 – Gladstone tills deposited in the valley bottoms (Cronmiller *et al.*, 2019).

Boulders were selected near the toe of the deposit in this cirque so as not to be significantly shielded by the surrounding cliffs. Sampled boulders did not appear to have experienced post-depositional shifting through permafrost processes. Additionally, the lack of fresh faces on the boulders suggests that they have been stationary for some time without significant spallation (Fig 3.10 C). There were thick organics in lower boggy lowland that had accumulated around blocks; this would cause partial shielding from

cosmic radiation. Therefore, samples were taken in an exposed portion of the slide deposit a few metres further upslope from the terminus of the deposit, where the potential for snow cover shielding would also be lower.

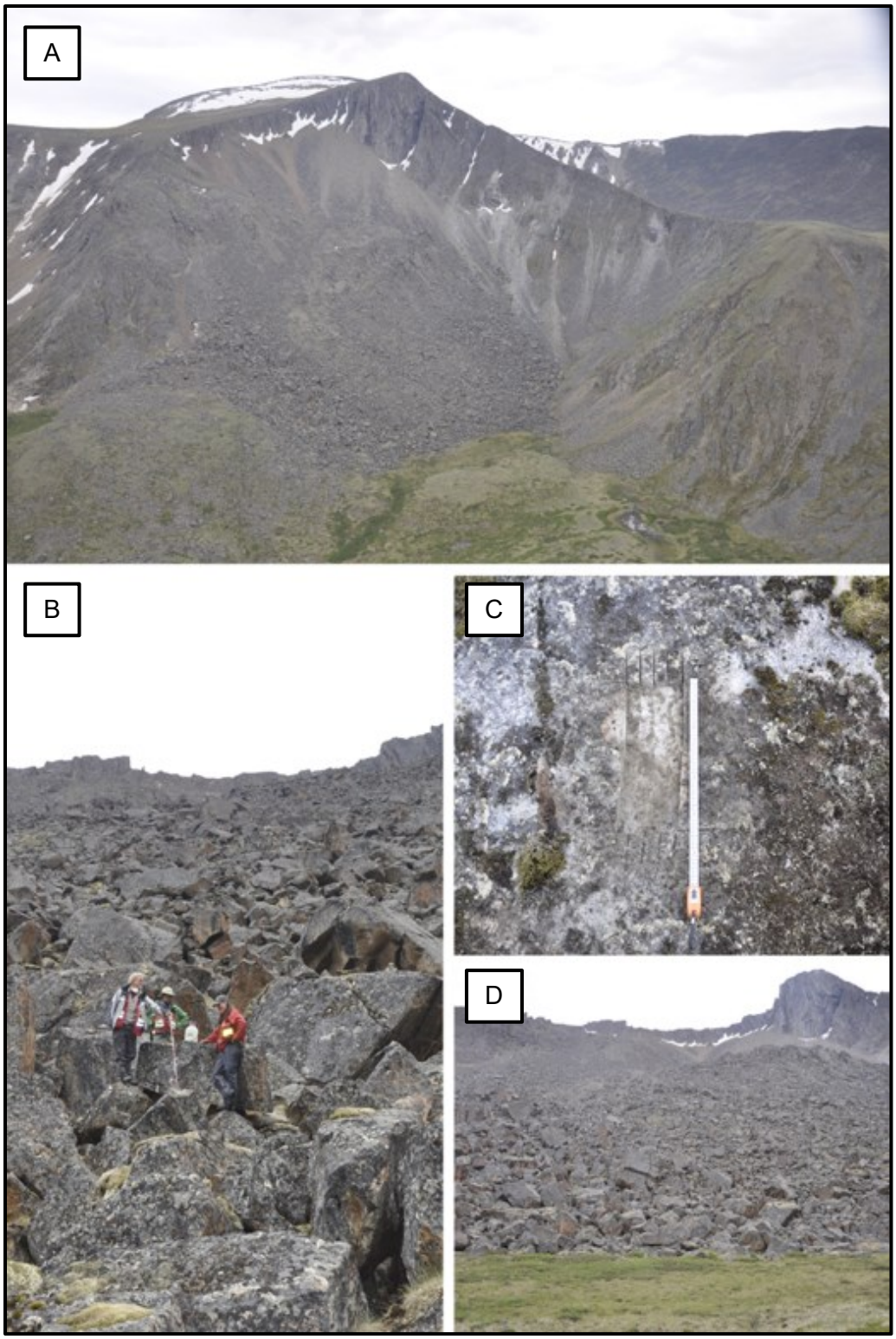

Figure 3.10. Gladstone-1 rock slide. (A) Oblique aerial view of the NNW-facing head scarp and deposit. This rock slide terminated in bog-like vegetation in the cirque. (B) One of the boulders sampled for TCN dating (NW-GC-02); Boulders had a homogenous size distribution and ranged from half a metre to a few metres tall. (C) Another typical sampling surface for a TCN-dated boulder. (D) Boggy, mossy terrain is present at the base of the slide.

Gladstone-2 Rock Avalanche

This deposit was sampled by Kristen Kennedy, Derek Cronmiller, and Sydney van Loon of the YGS in 2020. Approximately 10 km ESE of Gladstone-1, this is a south-facing rock avalanche on a meltwater-excavated slope. This event has a similar lack of vegetation as Gladstone-1 (Fig. 3.11). It has a flatter, more spread-like morphology as it is not as topographically constrained as Gladstone-1. The head scarp is roughly 400 m in elevation and is less arcuate than Gladstone-1. The deposit covers ~0.25 km^2 and abuts Gladstone Lake. The debris field slopes ~18° from the lake towards the base of the slope before the slope steeply climbs to 30°. The debris field extends roughly 0.3 km from the base of the slope to the lake and with a width of approximately 0.5 km perpendicular to the slope. Parallel to the fall line the deposit has a primary central ridge that slopes downwards towards the northeastern (~10 m drop in elevation, ~5° slope) and southwestern (15 m drop in elevation, ~2° slope) margins of the event.

Boulders were comparable in size to those at Gladstone-1, ranging from 0.5 to 1.5 m and had similar angularity with distinct weathering (Fig. 3.11). The most abundant lithology at this site were granodiorites, as observed at Gladstone-1. These rocks also have distinct lichen growth on their upper and side faces (Fig. 3.11 E).

Based on evidence from the field, it is possible that many of the boulders on this deposit have shifted as there appears to be some subsidence that may have occurred after emplacement. There was evidence of post-depositional movement on the landslide. Some rockfall is occurring from the head scarp. Zones of relatively lichen free, fresh-looking blocks indicate some deep-seated movement. Dry raveling, the downslope rolling, bouncing, or sliding of individual particles down a slope, is evident at the toe of the deposit and suggests that ongoing creep may be occurring (Gabet, 2003). This would skew TCN results toward younger ages if the sampled boulder surface was not always exposed or had shifted. Sampled boulders were in areas that did not appear to have secondary movement. Boulders were taken within 50 m of each other and therefore had similar topographic shielding (Fig. 1.33).

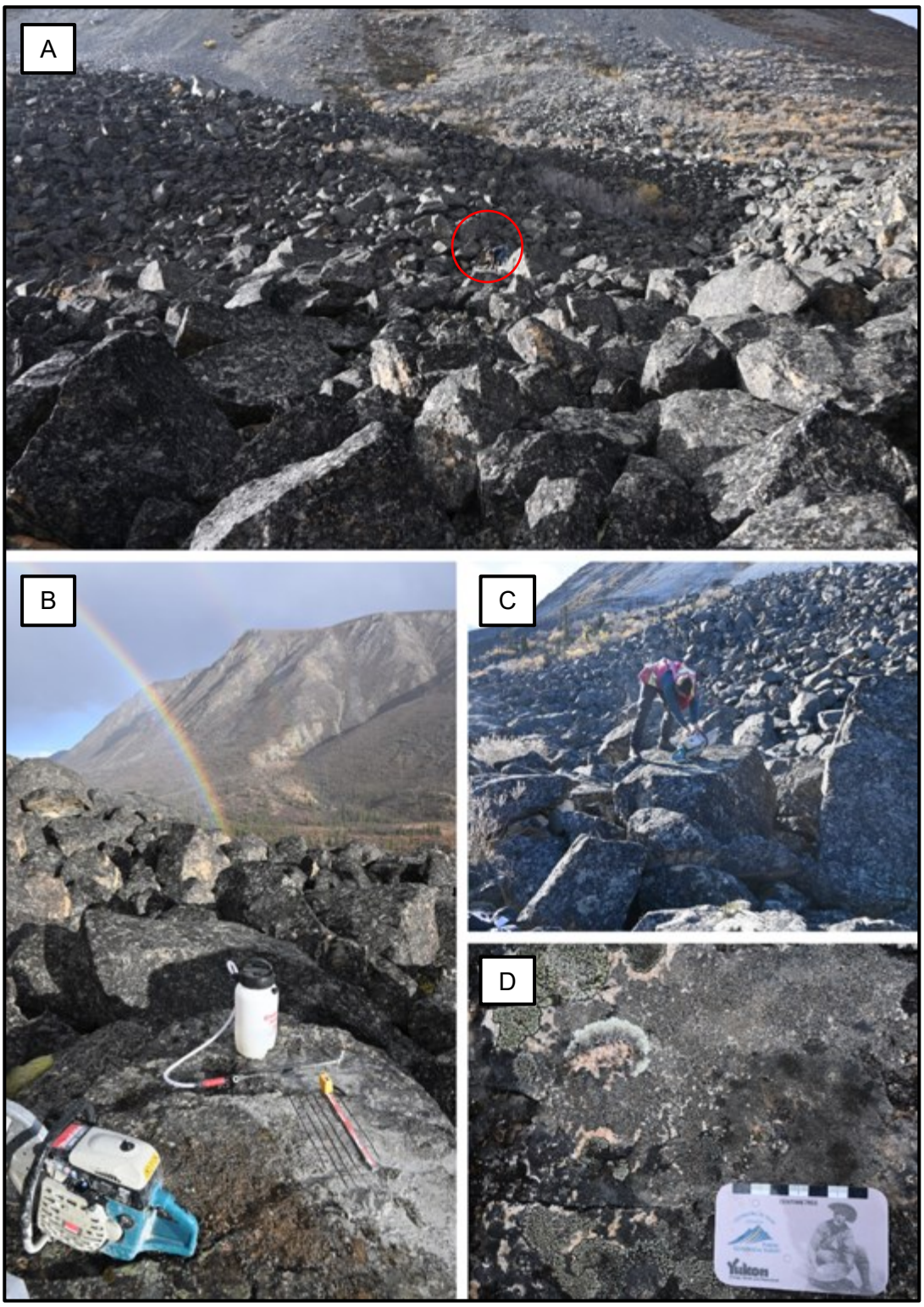

Figure 3.11. Gladstone-2 rock avalanche. (A) Blocks sampled here are of similar sizes to those observed at Gladstone-1. Person for scale in the red circle (B) & (C) A typical sampling site for a Quaternary geologist. (D) Lichen cover can skew cosmogenic ages due to increased acidic degradation. Photos courtesy of Kristen Kennedy (2021).

3.5.5. Generc Rock Slide

This site is located on the SSW-facing side of the Kluane Ranges near White River (61°53'20.34"N, 140°26'37.57"W) (Site 5 – Fig. 3.1) (Fig. 3.12). This deposit covers approximately 0.26 km^2 initiating from a head scarp ~640 m up the steep valley wall (Fig. 3.13). Based on an empirical relationship between landslide area and volume, the estimated volume of the event is $1.3x10^6$ m^3 (Guzzetti *et al.,* 2009). The average slope from the head scarp to the toe is 12° and the event terminated roughly 260 m away from the base of the slope with large boulders only travelling 150 m away. The debris field is lobate in aerial imagery and spreads over ~0.1 km^2 of the valley bottom with a perimeter of roughly 0.95 km^2.

On aerial photographs and satellite imagery, this site seemed ideal for TCN dating due to the presence of what appeared to be large boulders. However, when we arrived, we discovered that many of these 'boulders' were molards. We also inferred that in this case, these were molards which resulted from the degradation of ice-rich sediment due to the extensive permafrost in the area (Fig. 3.13; Morino *et al.,* 2019). Some of these molards reach up to 3 m in height (see helicopter for scale in Fig. 3.13). Boulders that were not molards are up to 1.5 m and are volcanic with calcareous veins and preserved slickenlines. Along the southern perimeter of the deposit, there is evidence of impacts, *e.g.* tree scars, and leaning trees (Fig. 3.13). Scars observed appeared circular with a yellow coating on the wood and were roughly 20 cm in diameter. There is an abrupt change in vegetation type around the perimeter of the event; a transition from lighter, more leafy species within the event to darker, more coniferous trees surrounding the area.

We did not sample for TCN dating because there was a lack of suitable material; as well, the deposit appeared far too young for a suitable analysis. This was evident by new growth on the deposit as well as what appeared to be rafted, upside-down conifers that were not in growth positions (Fig. 3.13). The presence of preserved fragile twigs on the rafted conifers also suggested that the event was recent. Evidence of tree scarring and leaning trees was observed around the southern perimeter of the event which may be indicative of a finer phase extending past the larger boulder deposits.

Figure 3.12. Generc rock slide as it appeared in 2010. Landslide morphology appears similar to what was observed during the 2019 field season. Exposed bedrock is observed in the feeder gully as it enters the valley bottom. The modern river now bisects the toe of the deposit. Alders were growing on the deposit and were surrounded by conifers on the perimeter; this helped delineate the extent of the landslide. A distinct change in vegetation type from younger deciduous growth on the deposit to more mature conifer growth around the landslide was evident in air photos as well as in the field. Image courtesy of Google Earth.

Figure 3.13. The Generc rock slide. (A) Taking field observations of dendrochronological Sample NW-GNRC-TS-02 (pick axe for scale is ~0.9 m) (B) A cross section of sample NW-GNRC-LT-04. (C) View of the Generc rock slide from the helicopter looking North, upslope towards the head scarp. (D) Evidence of landslide rafted debris. (E) One of the large molards on the landslide (approximately 6 m wide).

3.6. Results – Age Calculations

3.6.2. Sheep Mountain

By using a multi-dating method, such as radiocarbon dating, TCN, and tephrochronology, the age of the Sheep Mountain landslide is tightly constrained (Tables 3.1, 3.2). Samples were collected from what was proposed as two phases of a landslide: an older phase, samples “NW-OLS-SM”, and a younger phase, samples “NW-SM” (Fig. 3.4). Expanded datasets used in TCN analysis (*i.e.* scaling factors, sample prep information, AMS results, *etc.*) can be found in Appendix B. Radiocarbon samples collected at the two exposures resulted in age ranges of 2080 –1980^{14}C cal yr BP and 2106 – 1924 cal yr BP for the older phase (Table 3.2). Ages above and below tightly constrained the older phase at ~2.0 cal kyr BP.

The means of the ^{36}Cl boulder ages are 2.8 $\pm$ 0.9 kyr BP for the “OLS-SM” samples and 2.6 $\pm$ 1.1 kyr BP for the “SM” samples (Table 3.1). Within 1σ precision of the ^{36}Cl dating method, the age estimates for the two phases overlap. This raises the possibility that the proposed two events are: (1) separated by considerable time (Clague, 1981), (2) could be two phases of the same landslide, or (3) two events much more closely spaced in time than previously thought. A comparison of the radiocarbon and TCN results for these two sampled events shows significant overlap between the radiocarbon ages and the ^{36}Cl ages as well as the ^{36}Cl results between both phases. (Figs. 3.14, 3.15). However, the difference between the ^{36}Cl and radiocarbon ages indicates an issue with ^{36}Cl for this site as the radiocarbon ages most closely bracket the older phase. The ^{36}Cl ages, and associated scatter, may be due to potential inheritance despite stringent sampling methods; inheritance would skew a sample to appear older.

The younger White River Tephra (1170-1097 cal yr BP; Jensen *et al.,* 2014) was only found in exposures overlying the older phase of the event as well as around the periphery of the landslide. However, the “younger” phase was not rigorously examined for the tephra, *i.e.* in the medial portion of the debris field where the proposed younger phase overrode the older phase. Since the ^{36}Cl ages for the two events have significant overlap, it is statistically reasonable to assume that the two events were relatively contemporaneous, and that the younger phase was not younger than the tephra. The error associated with the ^{36}Cl AMS results was low; therefore, the lack of tephra on the

younger phase is most likely due to poor preservation combined with limited investigations. The difference in morphology of the two events may reflect that there is finer material incorporated into the ridges on the side of the landslide. That incorporation then allowed the preservation of the WRT on the outer portions of the landslide as opposed to the medial portions where preservation was poor.

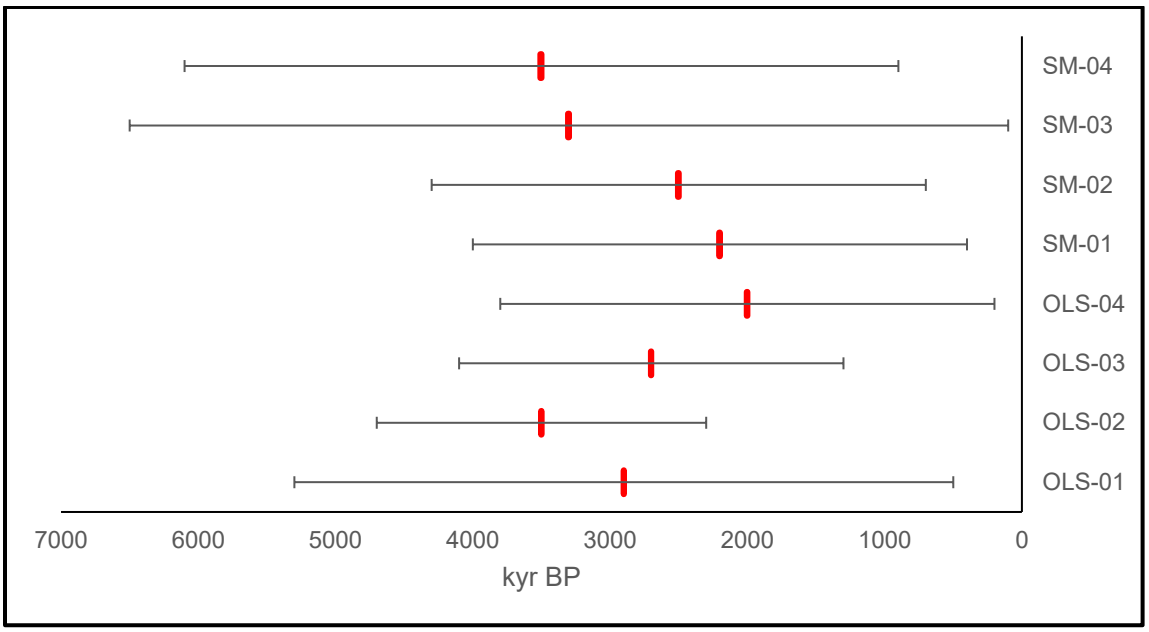

Figure 3.14. ^{36}Cl age results for the Sheep Mountain samples. Samples with ID "OLS" were collected from the older phase and samples with ID "SM" were collected from the younger phase. Error bars are 2σ.

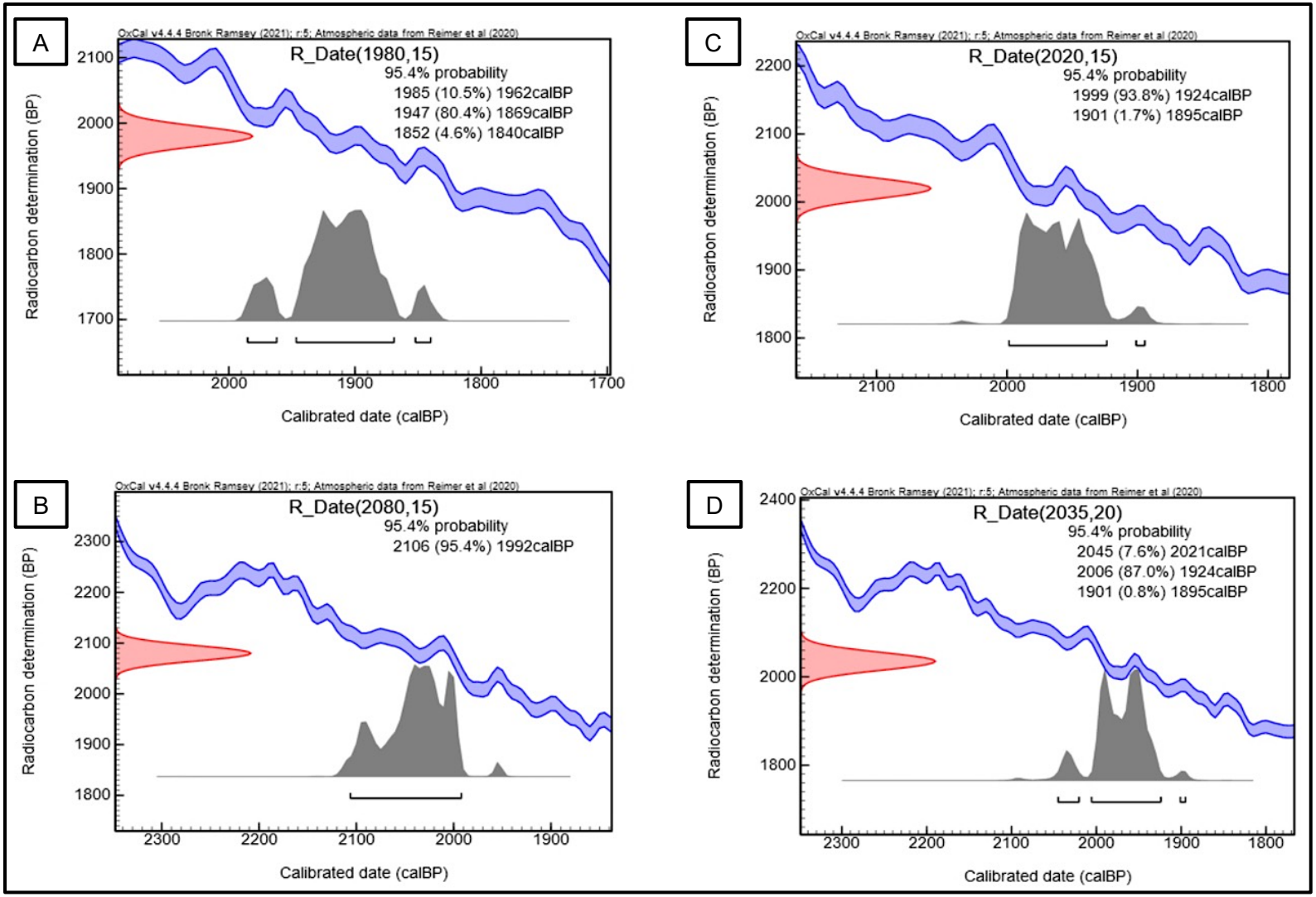

Figure 3.15. OxCal 4.4.4 IntCal20 calibration curves for radiocarbon samples (A) NW-SMNRC-W-01, (B) NW-SMNRC-W2-01, (C) NW-SM-RC-01, and (D) NW-SM-RC-02 within 2σ precision. The taller the grey histogram, the more likely that calibrated (calBP) age result is. The red histogram indicates the radiocarbon concentration in radiocarbon years "before present" (BP). The blue lines are radiocarbon measurements using known ages (± one standard deviation).

3.6.3. Aishihik

The average of the four ages is 5.7 $\pm$ 0.2 kyr BP (Table 3.1). The west ridge had an average age of 6.2 kyr BP and the east ridge had an average age of 5.4 kyr BP (Table 3.1). Running the data through the online exposure age calculator (version 3; Balco, 2017), the two younger ages from the east ridge were designated outliers and were originally pruned. This code assigns more weight to a younger age estimate being an outlier because most processes (*i.e.*, erosion, snow cover, shielding, toppling, *etc.)* lead to a boulder appearing younger. Geomorphologically, there was no evidence to substantiate the pruning of these two ages, so the mean age was calculated using all four samples. There is significant overlap between the two calculated ages and the discrepancy between the two ridge ages (*i.e.*, the East Ridge appearing older) could be due to inheritance. Therefore, it is within reason that the ridges, perhaps levees, of the Aishihik landslide were deposited at a same time, within the resolution of ^{10}Be dating.

3.6.4. Gladstone 1 & 2

Gladstone-1 occurred around 10.5 $\pm$ 0.3 kyr BP (Table 3.1). Gladstone-2 occurred at 11.2 $\pm$ 0.3 kyr BP if the younger outlier (sample NW-GLS-01) is omitted. This boulder may be from a rockfall ~5 kyr after the landslide or there could have been secondary movement causing rotation. There was field evidence of movement on the deposits, and although care was taken not to sample in these areas, a factor yet unknown caused this boulder to reveal a younger age.

Table 3.1. Ages of three landslides utilizing TCN dating from 8 ^{36}Cl samples and 10 ^{10}Be samples (Sheep Mountain, Aishihik, Gladstone-1 & 2).

Event Name	Analyzed Nuclide	Sample ID	Sample Location (latitude, longitude)	Elevation (m)	Midpoint Boulder Height (m)	Age Calculation (kyr)	Internal Error Total 1σ Precision (kyr)	External Error Total 1σ Random & Systematic (kyr)
Sheep Mountain	^{36}Cl	NW-SM-OLS-01	61.02713, -138.50537	843	0.6	2.9	1.2	1.2
		NW-SM-OLS-02	61.02725, -138.50543	844	1.5	3.5	0.6	0.6
		NW-SM-OLS-03	61.02717, -138.5054	843	0.65	2.7	0.7	0.7
		NW-SM-OLS-04	61.03117, -138.50119	838	1.0	2.0	0.9	0.9
		NW-SM-01	61.02772, -138.50417	830	1.75	2.2	0.9	0.9
		NW-SM-02	61.02884, -138.50412	849	4.4	2.5	0.7	0.7
		NW-SM-03	61.03392, -138.50572	917	1.2	3.3	1.6	1.6
		NW-SM-04	61.02826, -138.50348	836	2.7	2.5	1.3	1.3

Event Name	Analyzed Nuclide	Sample ID	Sample Location (latitude, longitude)	Elevation (m)	Midpoint Boulder Height (m)	Age Calculation (ka)	Internal Error Total 1σ Precision (kyr)	External Error Total 1σ Random & Systematic (kyr)
Aishihik	^{10}Be	NW-A-01	60.86126, -136.97704	816	1.75	6.0	0.2	0.4
		NW-A-02	60.86077, -136.97748	805	1.1	6.4	0.2	0.4
		NW-A-03	60.86008, -136.97044	841	1.8	5.5	0.2	0.4
		NW-A-04	60.85984, -136.96965	833	3.5	5.3	0.2	0.4
Gladstone-1	^{10}Be	NW-GC-01	61.40007, -138.28436	1572	1.5	10.8	0.3	0.7
		NW-GC-02	61.40001, -138.28406	1581	1.1	10.3	0.3	0.7
		NW-GC-03	61.40044, -138.28352	1577	1	10.4	0.3	0.7
Gladstone-2	^{10}Be	NW-GLS-01	61.381396, -138.093153	n/a	1.4	5.6	0.2	0.4
		NW-GLS-02	61.380973, -138.093210	n/a	0.5	11.9	0.3	0.8
		NW-GLS-03	61.381088, -138.093067	n/a	1.5	10.5	0.3	0.7

UCIAMS #	Sample name (Exposure Site)	^{14}C age (BP)	±	Calibrated Ages (cal BP)	Previous Radiocarbon Ages (Clague, 1981; Koch *et al.* 2014)	
233890	NW-SMNRC-W-01 wood (Northern Roadcut)	1980	15	1947 – 1869 (80.4%) 1985-1962 (10.5%) 1852-1840 (4.6%)	**490 ± 50 ^{14}C yr BP**	**563 - 456 cal yr BP**
					Pith on top of the younger rock avalanche deposit	
233892	NW-SMNRC-W2-01 wood (Northern Roadcut)	2080	15	2106 – 1992 (95.4%)		
233891	NW-SM-RC-01 twig (Soldier's Pass)	2020	15	1999 – 1924 (93.8%) 1901-1895 (1.7%)	**1950 ± 50, ^{14}C yr BP**	**1992-1741 cal yr BP**
					Underlying the older rock avalanche deposit	
233893	NW-SM-RC-02 twig (Soldier's Pass)	2035	20	2006 – 1924 (87.0%) 2045-2021 (7.6%) 1902-1895 (0.8%)	**1910 ± 20 ^{14}C yr BP**	**1881-1742 cal yr BP**
					Branch between the uppermost debris flow unit and the rock avalanche unit	

Table 3.2. Radiocarbon ages for the Sheep Mountain event. Samples were analyzed at Keck Carbon Cycle AMS Facility. The probabilistic method was used to calibrate ^{14}C to the IntCal 20 curve within 2σ error (OxCal 4.4.4). The relative likelihood of the most likely age range is shown in the brackets as percentages.

3.6.5. Generc

Air photo analysis allowed relative constraint of the age of this landslide. Photographs taken in 1988 (NTS 115F088) (Fig. 3.16 A) show no evidence of the landslide. The 1998 aerial photograph, however, shows the outline of the landslide as it appears today (Air Photo A28346-153, National Air Photo Library) (Fig. 3.16 B). Photographic evidence, in conjunction with the ages obtained from dendrochronology, further constrain the age of the event to around the mid to late 1990s CE. Historical landslides like these can be easily correlated to seismic data; various government agencies' paleoseismic databases extend back to the late 1800s in the area. Potential seismic events will be postulated in Section 3.6.1.

Human error is the primary means of introducing error when counting tree rings in dendrochronology; false tree rings may be considered, or rings may be missed entirely. False or missing rings are reduced by utilizing the entire tree disk and counting along several radii. However, mold on some the samples created pits and degraded the rings. This made it more difficult to differentiate them and could potentially result in a miscount of one or two rings depending on the thickness of the rings and the degree of degradation. This was most prominently a concern in sample NW-GNRC-TS-02 where several rings were severely disrupted and difficult to separate out in counting (Table 3.3). The margin of error considered in this study was ± one year; two rings, one light and one dark. Based on the samples counted and the aerial photographic record, it is likely that the landslide occurred in 1996-1997. Sample TS-02 was most likely impacted by some other event such as animal (porcupine), insect infestation, or wind throw from another tree (Margolis *et al.,* 2007; Daniels *et al.,* 2017).

Table 3.3. Summary of the dendrochronological data from the Generc event.

Event Name	Sample ID	Year of Sample Collection	Number of Rings	Error (± yr)	Year of Impact/Event	Additional Notes
Generc	NW-GNRC-TS-02	2019	~73[a]	1	~1946[b]	Scar was facing ~036°, towards the landslide initiation zone. The rings were thinner post impact suggesting that the tree was not thriving, but alive.
	NW-GNRC-TS-03	2019	~23[a]	1	1996[b]	Another tree scar also facing ~NE,
	NW-GNRC-LT-04	2019	22	1	1997	

[a] *Age is approximate to ±1 year due to some degradation and pitting of the rings caused by mold which made them more difficult to discern*

[b] *Age is also approximate to ±1 year due to errors carrying over from the previous column*

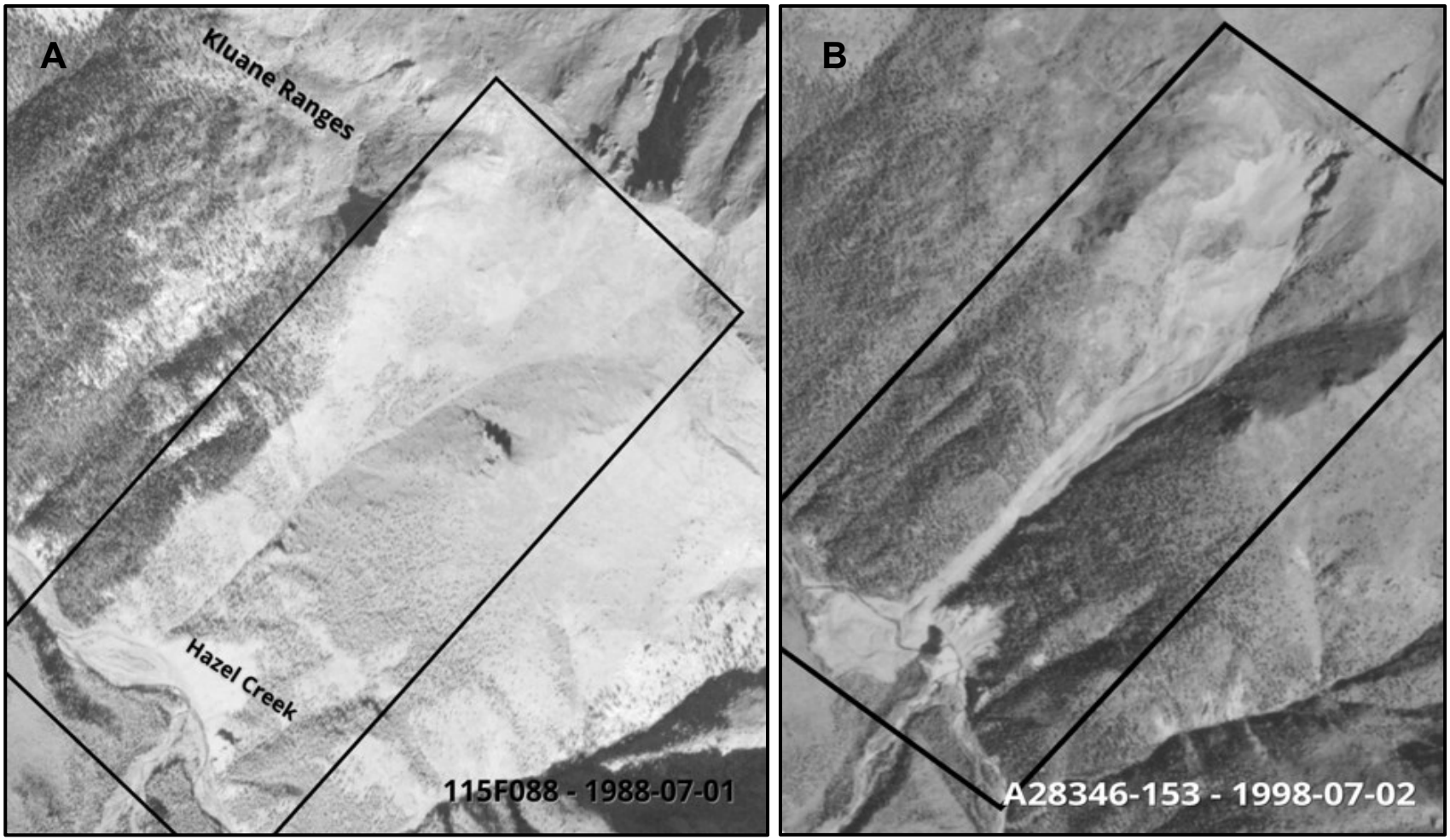

Figure 3.16. Air photos obtained from the Yukon Geological Survey and taken 10 years apart depict the Generc event occurring sometime between 1988 (A) and 1998 (B). The outline of the event is shown in the black boxes. The modern Generc landslide as of 2019 appears very similar to the 1998 aerial photo. ©YukonGovernment ©NationalAirPhotoLibrary.

3.7. Discussion

The results have improved knowledge of geomorphology and chronology of five large landslides in the Kluane Lake area. The new TCN exposure ages, radiocarbon ages and dendrochronology place all the events in the last 11 kyr, highlighting that the area has undergone large-scale mass wasting processes in the past. Many more landslides need to be studied and dated before we can establish a landslide frequency and a probability for similar magnitudes of rock slides and rock avalanches. However, using the available chronology, we can determine if any of the deposits can be linked to past earthquake or major climate events in the late Holocene and begin to establish any common first-order causes.

3.7.2. Comparison with Regional Paleoclimate

Increasing temperatures in glaciated terrains can lead to glacial recession with subsequent unloading and debutressing of valley walls, increased water content reducing slope material shear strength, and permafrost degradation (Gruber *et al.,* 2015; Patton *et al.,* 2021). Focussing on the latter, as permafrost is ultimately a hydrological feature, permafrost thaw can increase water percolation into pre-existing fractures and faults and weaken slopes in a changing climate. These processes are conditioned by thermal regimes of annual and long-term variability, and impact active layer dynamics, the distribution of ice, and the thermodynamic state of the permafrost (Lafrenière & Lamoureux, 2019). In a recent permafrost series of papers from the Arctic Institute, it was stated that a 3°C increase in global temperatures could thaw 30-85% of the upper permafrost layers across the Arctic region (Bykova, 2020; 2021). Since one third of the world's permafrost is found in mountainous regions, it can be deduced that periods of local warming in Yukon may have resulted in permafrost thaw on these steep terrains (*cf.* Gruber *et al.* 2015).

Present mean July temperatures at the Otter Falls Station (61°02' N, 137°03' W) are 13.1°C (Environment Canada, 2022). Examining paleoclimatic reconstructions can help identify trends of Holocene warming where landsliding may have been more prevalent due to permafrost degradation and glacial debutressing. All study sites in this thesis lie within either zones of extensive or sporadic discontinuous, or high-temperature,

permafrost, therefore, these sites are sensitive to changes in temperature (Jorgensen & Osterkamp, 2005; Bonnaventure *et al.,* 2012; Liu, 2020).

Paleolimnology, or the study of lake sediment cores, has been utilized in many Quaternary studies to determine the paleoclimate of Yukon (Cwynar, 1982; Fisher *et al.,* 2004; Anderson *et al.,* 2005; Bunbury & Gajewski, 2009; Kurek *et al.,* 2009; Bunbury & Gajewski, 2012; Rainville & Gajewski, 2013; among others). Lake sediment cores from these studies were analyzed (Fig. 3.17) to determine if there were any periods of Holocene warming in the region that may have contributed to permafrost degradation or warmer, wetter conditions that could increase slope failure. These sediment cores were from Jenny Lake, Upper Fly Lake in SW Yukon and Moose Lake, and Hudson Lake in Alaska.

General warming trends can be identified from both pollen and chironomid assemblages found in lake sediment cores (Fig. 3.18). A vertical red bar was drawn through these figures to depict approximate estimations of when mean July temperatures, T_{July} (°C) were increasing. Warmer Holocene temperatures would have accelerated initial deglaciation and once the glaciers had receded, warmer and wetter conditions would have further weakened exposed bedrock on the slopes. Lakes sampled closer to the Kluane Lake region, such as Upper Fly and Jenny Lake, were weighted heavier in the determination of Holocene and Late Pleistocene temperatures. Comparing the data between the lake sediment cores, there appear to be six general periods of Holocene warming (*i.e.* potential periods of permafrost thawing).

The chronologies reveal that there may be some climatological influences on the Gladstone events. Climates in the study area were ~4-6°C warmer (based on chironomid-inferred T_{July}) following the termination of the Younger Dryas (YD). The YD occurred between 12.9 and 11.2 ka ago at Upper Fly Lake, and within error, Gladstone-1 (orange circle, Fig. 3.18) and Gladstone-2 (yellow circle, Fig. 3.18) occurred shortly following its termination (Bunbury & Gajewski, 2009). Glacial debuttressing combined with the rapid warming resulting in permafrost thaw within these valleys may also have conditioned the slopes following deglaciation. As GLS-1 occurred in a cirque wall, during the last glaciation, the exposed ridge likely would have contained permafrost; therefore, the warming period could have thawed that permafrost, conditioning the slope since the joints would have become potential planes of weakness. Additionally, glacial erosion

oversteepened the slope, and as the glacier melted, it was no longer buttressing the slope, allowing release along fractures or joints. However, the main conditioning that deglaciation in the gladstone-1 area would accomplish is erosion and oversteepening of the slope. However, as the paleoclimatic records were obtained approximately 40 km south of the gladstone area and are at a lower elevation than the Kluane Plateau, these paleoclimatic comparisons are a best guess and do not exhibit a distinct triggering mechanism at this time.

The Aishihik landslide (green circle, Fig. 3.18) appears to be correlated with warming and peak summer temperatures as seen in both Moose Lake and Hudson Lake around 5,500 cal BP (Clegg *et al.*, 2010; Clegg *et al.,* 2011). One possible explanation for the failure is that warmer and wetter conditions would have resulted in increasing pore water pressures in the fractures and joints in the head scarp. The failure plane would have developed from pre-existing faults and joints in the rock. As slow movement occurred, areas of solid rock, rock bridges, would fracture; as the failure surfaces become more continuous, movement rates would increase, fracturing more rock bridges. Eventually once enough rock bridges have fractured, catastrophic failure would occur. In this case, there may not have been a trigger, it was just time for this rock slide to fail; this is why even with modern landslides, it is difficult to determine what the exact triggering mechanism is.

General warming over the thousand years leading up to the Sheep Mountain landslide may have conditioned the slopes and contributed to the failure at Sheep Mountain (blue circle, Fig. 3.18). However, the Sheep Mountain failure may be attributed to another mechanism, paleoseismicity.

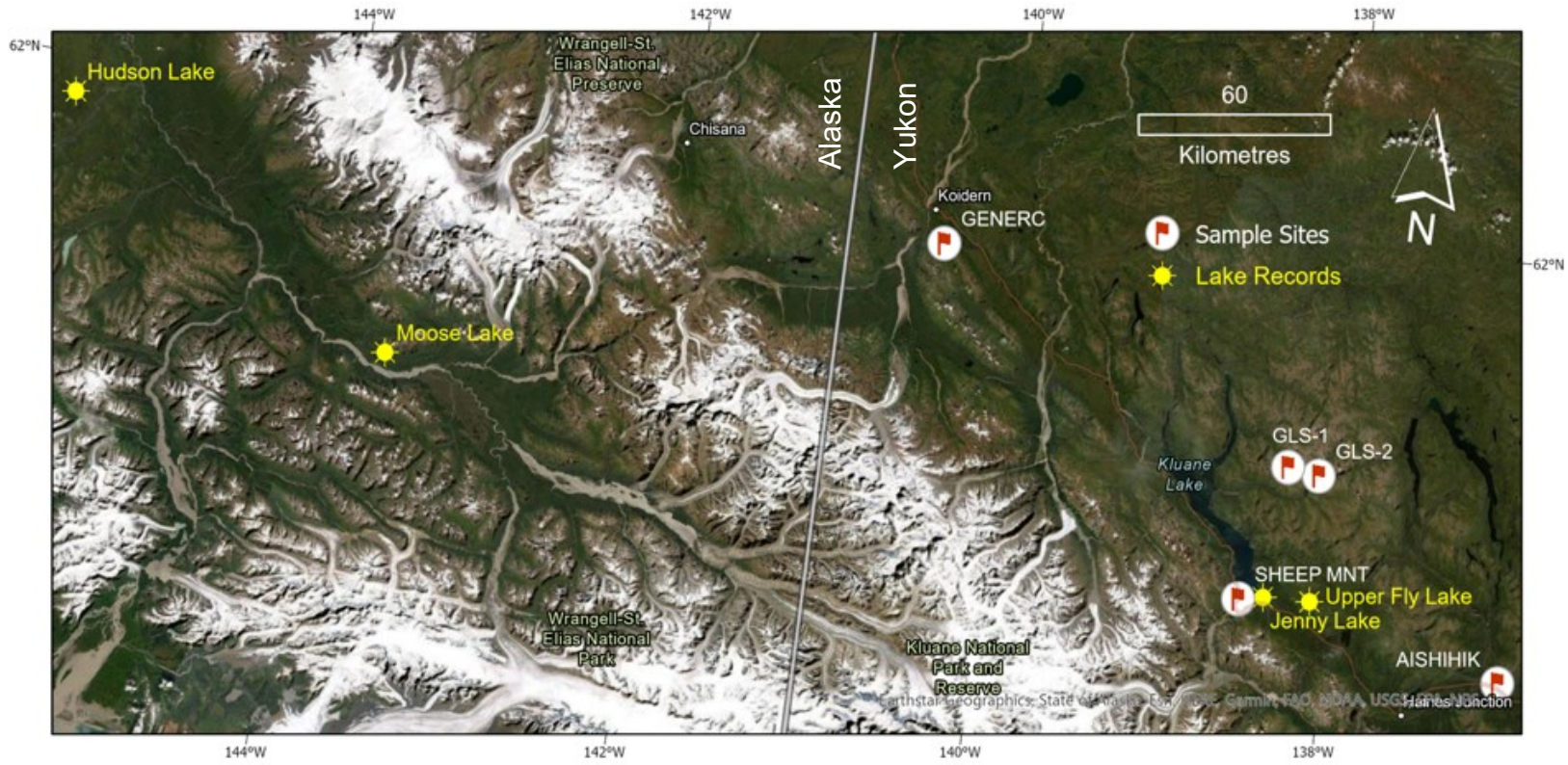

Figure 3.17. Previously examined lake sediment cores from lakes around the Kluane Lake area; these sites were used in this study for paleoclimatic comparisons.

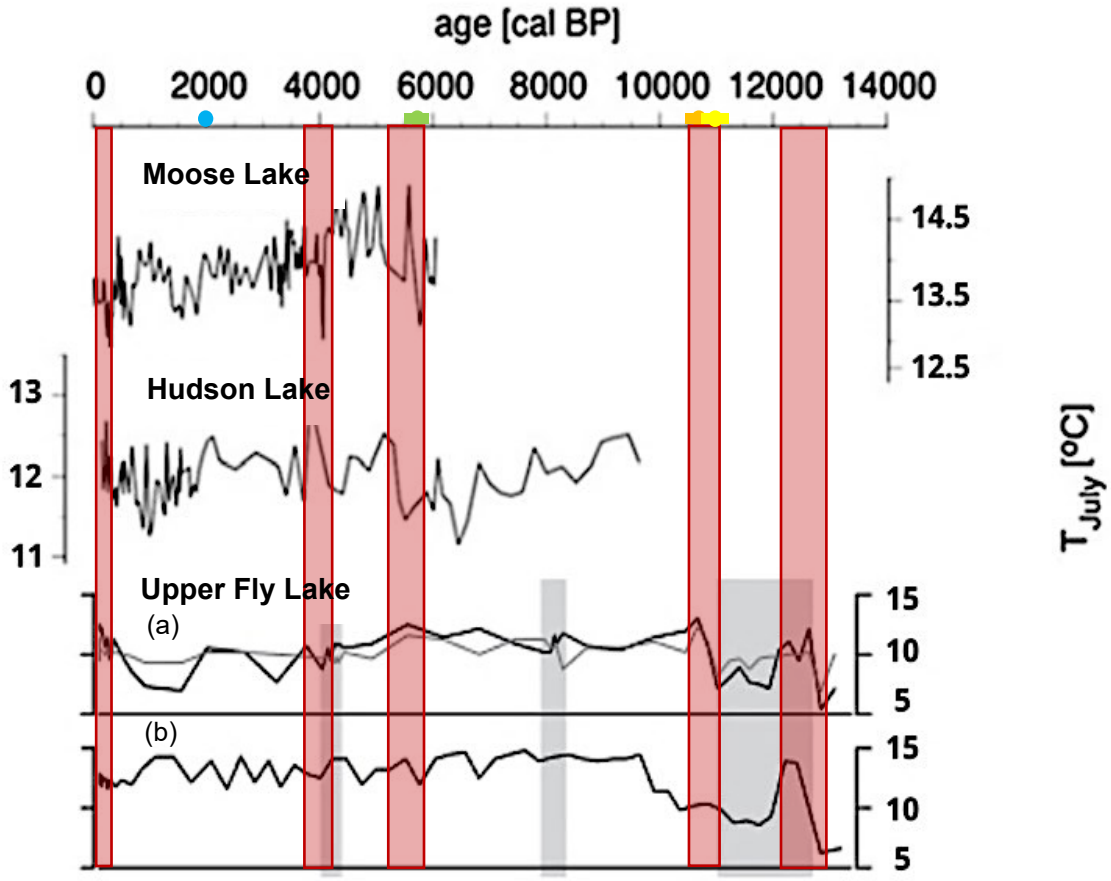

Figure 3.18. Mean July temperatures, TJuly (°C) ascertained from lake sediment cores around Yukon from 14,000 to 0 cal BP. Three lakes were used to compare Holocene and Late Pleistocene climates: Moose Lake, Hudson Lake, and Upper Fly Lake. Upper Fly Lake (a) Pollen-inferred and (b) chironomid-inferred paleoclimate reconstructions. Red vertical bars were drawn to temporally correlate periods of Holocene warming. The coloured dots and bars correspond to ages obtained from dated landslide events: Sheep Mountain (blue), Aishihik (green), Gladstone-1 (orange), Gladstone-2 (yellow). Modified from Bunbury & Gajewski (2009) & Clegg et al. (2011).

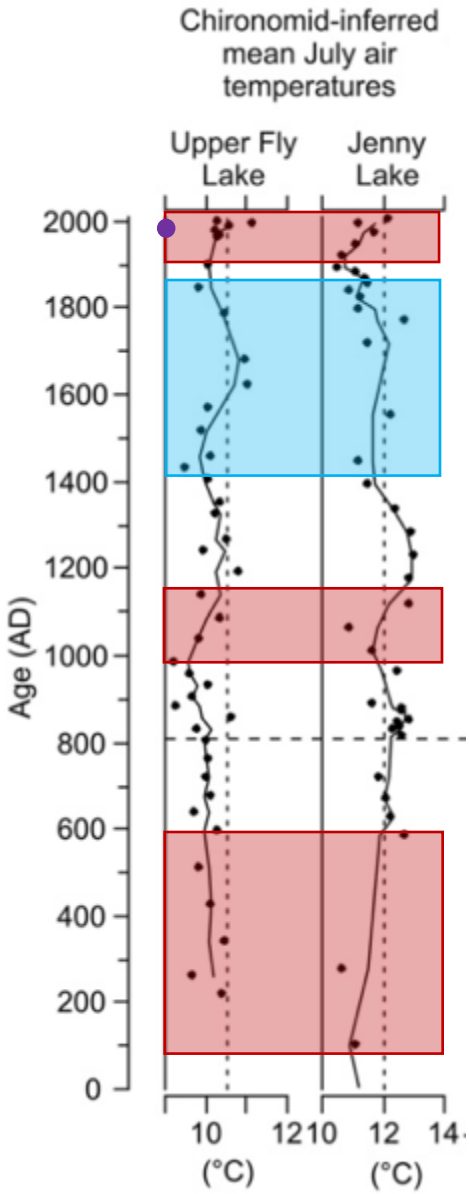

Figure 3.19. Chironomid-inferred mean July temperatures for Upper Fly Lake and Jenny Lake. The red boxes denote areas of climatic warming, and the blue box represents the timing of the Little Ice Age in SW Yukon. The horizontal dashed line represents the timing of White River Tephra deposition. The Generc landslide (~1998 AD/CE) is shown by the purple dot. (Modified from Bunbury & Gajewski, 2012).

Finally, Generc also appears to have occurred shortly following a warming period of ~0.5 – 1.5°C around 1900-2000 AD/CE (purple circle, Fig. 3.19). Molards containing permafrost were observed within the landslide deposit.

Using modern climatological records from Beaver Creek YTG (62°22' N, 140°52' W) within the years of 1995, 1996, and 1997, total precipitation values averaged 399.0, 321.6 and 478.6 mm respectively (Fig. 3.20; Environment Canada, 2022). Compared to the average from 1988-2010 recorded at Beaver Creek (298.6mm), increased precipitation could have conditioned the slope for failure in this time interval. The mean July temperature over the three years at Beaver Creek was 12.1°C which is comparable to the average recorded between 1988 and 2010 (14.1°C).

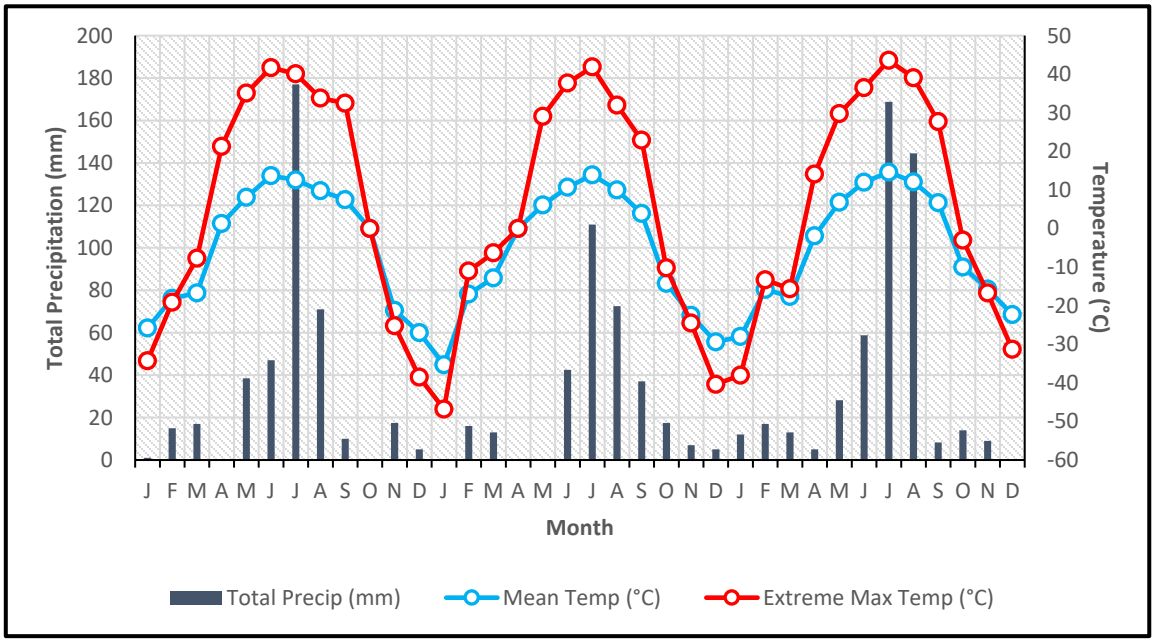

Figure 3.20. Monthly climate records for 1995, 1996, and 1997 from the Beaver Creek weather station. Data courtesy of Environment Canada (2022).

3.7.3. The Effects of Regional Paleoseismicity & Seismicity

The study area is located within a region of notably high seismic activity, owing to its proximity to both the Duke River and Denali faults. Understanding rock slide triggering mechanisms in the Kluane Lake region requires paleoseismic records. Organizations such as the United States Geological Survey (USGS) and Natural Resources Canada (NRCan) have investigated movement along the Denali Fault System, in particular the Yukon segment of the Denali fault; they analyzed trench walls, lake core data, and surface displacements, such as laterally displaced mounds, near the Denali fault (Seitz *et al.* 2008; Blais-Stevens *et al.,* 2020). Historical seismic catalogues are also utilized in

this discussion, but only apply to more recent landslides, *e.g.* Generc. The first part of this discussion will examine the primary paleoseismic study conducted in this study area.

An initial study examining paleoseismicity near Kluane Lake was presented by Seitz *et al.,* (2008) in a poster at San Diego AGU. This was a joint effort between the USGS and YGS to examine Holocene movement along the Denali fault, 280 km southeast of the Denali-Totschunda fault intersection. Large, elongate mounds, surface expressions of the fault, were identified during aerial reconnaissance. These features ranged from 10-50 m wide, 20-70 m long and up to 10 m high (Seitz *et al.,* 2008). These were presumed to be tectonic pushups and equal offsets of 20-30 m within these mounds were observed at several sites (Seitz *et al.,* 2008; Haeussler *et al.,* 2017). A minimum slip rate of 1.7-2.5 mm/yr was determined since these features formed after deglaciation (~10-12 ka). This minimum slip rate is greater than previously documented (<1 mm/yr) and based on the size and displacement of these mounds, it was presumed that they accommodated several large paloeseismic events. Three cross-fault trenches were excavated along a 2-km-long segment of the Denali fault near Duke River (61°21’54.36” N, 139°07’59.34” W). Twelve AMS radiocarbon ages provided chronological constraints for three paleoseimic events: Event 1 - 300 - 1,200 cal yr BP; Event 2 - ~2,200 cal yr BP; Event 3 - ~3,000 cal yr BP. A fourth event was recorded in this study, but the authors were less certain of its validity.

Blais-Stevens *et al.* (2020) re-excavated two of the three USGS trenches near Duke River, (Fig. 3.21 D,E,F) and expanded upon the work previously conducted by the USGS (Seitz *et al.*, 2008). These sites were all at or crossing the Denali fault and displayed surface expressions of Denali fault activity. Site D included the three previously excavated trenches (T1-3); these trenches exhibited evidence of co-seismic deformation, particularly the folding and faulting of strata, *e.g.* folded White River Tephra layers. The trench face at T3 was interpreted to be a negative flower structure in a strike-slip fault setting. Lake sediment core samples were from Crescent Lake (site E). This site was interpreted as a feature created 6,800–6,500 years ago by rupture of the Denali fault. Initially, a bog formed into a lake that abuts the west side of the fault, and during an earthquake, subsidence along the fault scarp resulted in the formation of a sag pond. That lake is located against the west side of the fault scarp. Silty detrital remnants from this scarp have been periodically deposited and interpreted as subsequent disturbances in this lake due to activity from the nearby fault. Site F is the Duke River bluff, a

Pleistocene glaciofluvial terrace where wood samples were collected for radiocarbon dating. Evidence of paleoseismicity at this site include strata disturbances near the fault trace, a positive flower structure associated with strike-slip displacement, and fractured pebbles within the fault zone. Although Blais-Stevens *et al.* (2020) were not able to determine the degree of slip along the fault during each earthquake, the presence of surface ruptures indicates that these were high magnitude earthquakes (~6-7 or more) (Eberhart-Phillips *et al*., 2003; Haeussler *et al.,* 2004; Matmon *et al.,* 2006). The importance of knowing the relationship between earthquake magnitude and the area of landsliding affected will be explored later in this section.

A summary of paleoseismic ages found from each site are shown in Table 3.4 as well as the potential co-seismic landslides from this thesis. It is highly likely that at least one or more of these seismic events triggered the Sheep Mountain and/or the Aishihik event. Likely seismic events 2 (~2.2 cal kyr BP – USGS trench data; 1.2 – 1.9 cal kyr BP – Crescent Lake data), and less likely event 3 (~3.0 cal kyr BP – USGS trench data; 1.7 – 5.9 cal kyr BP – Crescent Lake data), triggered the Sheep Mountain event. This is based on proximity to the Denali fault and there is less of a paleoclimatic influence at this site. Seismic events 4 (5.9 – 6.2 cal kyr BP) and 5 (6.5 – 6.8 cal kyr BP) could have triggered the Aishihik rock slide, but this is less definitive as this landslide is much farther from the fault line (~50 km) and the area is much more physiographically stable on the Kluane Plateau.

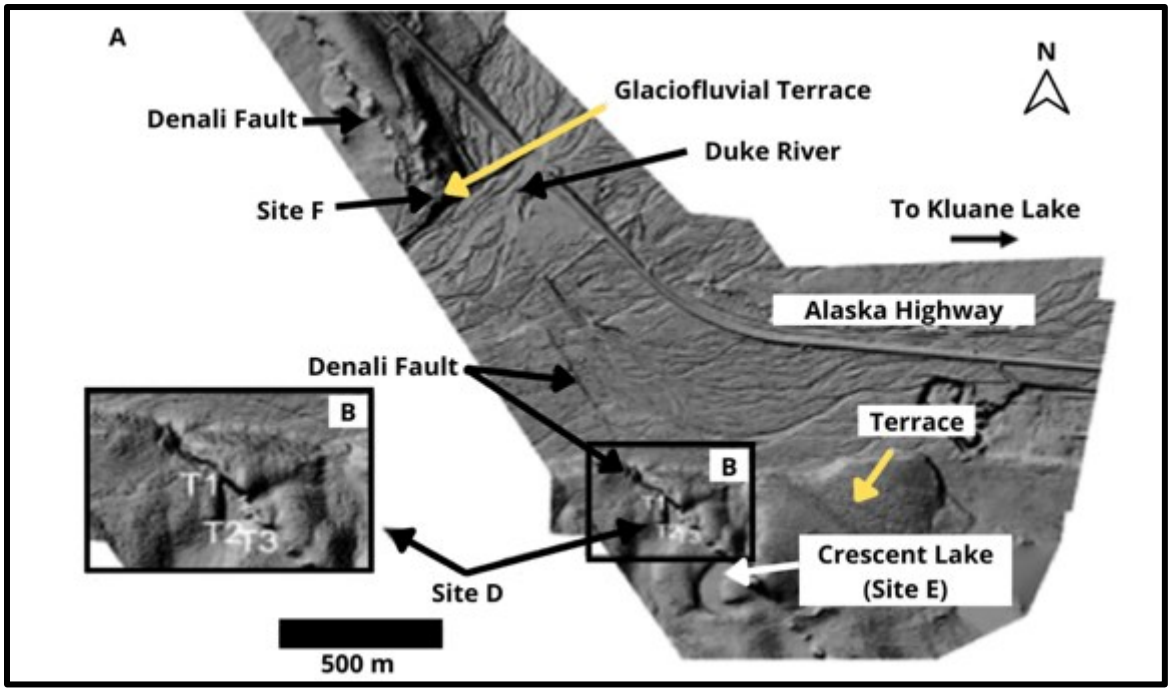

Figure 3.21. Lidar imagery of the study sites near Duke River and the eastern portion of the Denali Fault (Denali F.). Site F is the Duke River Bluff. Site D consists of three trenches dug by the USGS, only two of which were revisited by NRCan (T2, T3). Site E is Crescent Lake. (Modified from Blais-Stevens et al., 2020).

Table 3.4. Summary of paleoseismic data obtained by the USGS and NRCan in the Kluane Lake region. Unless stated otherwise, ages are given in cal yr BP. Modified from Blais-stevens et al. (2020).

Seismic Event	USGS Trench (Seitz *et al.* 2008)	Crescent Lake Sediment Cores (Blais-Stevens *et al.*, 2020)	Duke River Bluff (Blais-Stevens *et al.*, 2020)	Potential Landslide Triggered
1	300 - 1,200	Post - 1,200	300 - 1,200	N/A
2	~2,200		Not observed	
		1,200 - 1,900		Sheep Mountain
3	~3,000	1,700 - 5,900	Not observed	~2 cal kyr BP
4	6,000 - 6,200	5,900 - 6,200	Not observed	
				Aishihik
5	Not observed	6,500 - 6,800	Not observed	5.7 ± 0.4 kyr BP

Historical earthquake catalogues are also essential tools when reconstructing landslide histories during the Holocene. However, this type of information can only be applied to more recent landslides, ***e.g.*** Generc. A query of both the USGS (2022) and NRCan (2022) earthquake catalogues was conducted for the Generc rock slide as it occurred sometime in historical record (between 1988 and 1998, likely 1996-7). Earthquakes that occurred less than 100 km of the landslide with at least a magnitude of 4 were selected based on previous parameters determined by Keefer (1984). Through this search, three earthquakes occurred between 1994 and 1999 with local magnitudes (M_L) between 4.2-4.5 M_L. (Fig. 3.22). To determine if these seismic events were strong enough to initiate the Generc landslide, an empirical relationship between the magnitude of an earthquake and the area affected by land sliding is examined (Eq. 3.1).

$$\log_{10} A = M - 3.46(\pm 0.47) \qquad \textit{Eq. 3.1}$$

Keefer and Wilson (1989) analyzed data from 40 historical earthquakes with associated landslide inventories to determine the number of landslides that can be triggered given an earthquake magnitude (Keefer, 1984). From this study, it was determined that the smallest magnitude that can trigger rock sliding is ~4.0, depending on the distance to the epicentre and duration of shaking. A similar study conducted a few years later built on this relationship, with the addition of 7 earthquakes, and compared the area affected by landslides (A, km^2) to the magnitude of the seismic event (**M**) (Keefer & Wilson, 1989). Based on this equation, the magnitudes of the three earthquakes could only trigger an event between 1.3 – 4.5 km away. Therefore, the three queried earthquakes in this study were either not strong enough and/or too far away (>25 km) from Generc to have triggered it (Fig. 3.22). Holocene seismicity, however, is a conditioning factor that may have weakened the rock in the Generc area and may have contributed to its failure.

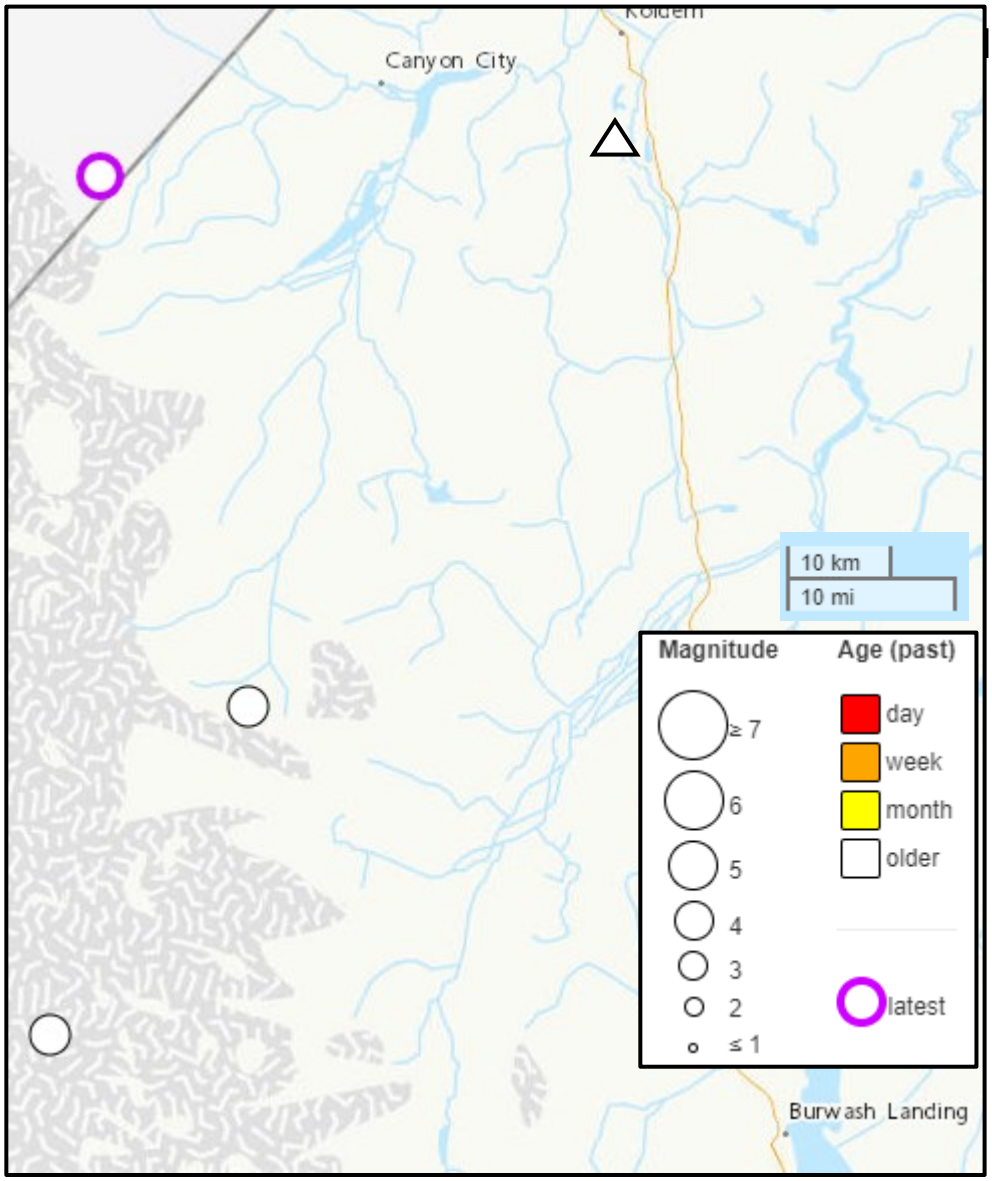

Figure 3.22. Historical earthquakes in the western portion of the study area. The Generc landslide is denoted by the white and black triangle. Each of these earthquakes occurred in the last decade of the 20th Century, and ranged from 4.2-4.5 M_L. The Alaska Highway is shown in yellow. Retrieved from NRCan, 2022.

3.8. Conclusions

Landslides in the Kluane Lake region were dated using several chronological techniques: terrestrial cosmogenic nuclide dating, radiocarbon dating, dendrochronology, and tephrochronology. Average ages for each event are:

1) Sheep Mountain – ~2.0 cal kyr BP.
2) Aishihik – 5.7 $\pm$ 0.4 kyr BP
3) Gladstone-1 – 10.5 $\pm$ 0.3 kyr BP
4) Gladstone-2 – 11.2 $\pm$ 0.3 kyr BP
5) Generc – 1996-1997 CE

Based on the ages, the paleoclimatic history of southwestern Yukon, and the proximity of these landslides to the Denali fault, it is very likely that there is at least one, if not two conditioning factors for these events: paleoclimatic, paleoseismic, or a combination of multiple factors.

Looking at the paleoseismic history of the region, it is possible that seismic event 2 (1.2 – 1.9 cal kyr BP, Blais-Stevens *et al.,* 2020) triggered the Sheep Mountain rock slide. As the Sheep Mountain landslide occurred a few km away from the Denali fault, paleoseismicity was most likely the driving factor of initiation as opposed to paleoclimatic warming, although it may have contributed. If Sheep Mountain is a coseismic landslide, the age of 2 cal kyr BP likely better constrains this seismic event. Whether or not Sheep Mountain experienced two separate events versus two phases of the same landslide is unfortunately outside the resolution of the ^{36}Cl dating method. Field observations implied two morphologically distinct zones, and the absence of WRT on the younger phase was thought to be an indicator that these were two events. However, the lack of WRT is likely due to a lack of preservation/observation as the ^{36}Cl ages indicate it is older than the WRT. Further reconnaissance of areas with soil accumulation, such as the Northern Roadcut, will help determine the presence or lack of WRT on the younger phase. These are questions that could be answered with further field observations on Sheep Mountain. In terms of inheritance, we cannot do a quantitative analysis in this case because it depends on one major effect: has there been removal of mass on this cliff prior to this event? If there was a lot of inheritance, it could be assumed that there was probably not a lot of removal, *i.e.*, if one of the ages came out to 10 kyr BP, then this slope has

probably been stable for a long time. However, since the eight dated boulders had a relatively low amount of inheritance, it could be interpreted that this cliff has been active, and that does not accommodate a big buildup of inheritance.

It is also possible that the Aishihik landslide was triggered by a past earthquake, particularly events 5 (5.9 – 6.2 cal kyr BP, Blais-Stevens *et al.,* 2020) or less likely, 6 (6.5 – 6.8 cal kyr BP, Blais-Stevens *et al.,* 2020). A structurally weakened head scarp may have been conditioned by seismic shaking, but since it is located far from the Denali fault, it is less likely. However, if more landslides near Aishihik are dated to a similar time, than a common paleoseimic trigger may be a reasonable assumption. Based on the Hanging Lake sediment core data, temperatures were also warming during this period which may have contributed to conditions more conducive for landslide initiation.

Gladstone events 1 and 2 occurred during a period of Holocene warming and were more likely initiated by permafrost thaw. Additionally, combined glacial debutressing within the valleys of the Ruby Ranges would have helped condition the slopes for an eventual failure. While there may have been some component of seismic conditioning, these landslides occurred in a more stable physiographic region and were therefore more likely to be initiated by deglacial or paraglacial factors.

Finally, as Generc was a historical event, it was determined that it was most likely not initiated by one of the modern earthquakes near the Denali fault. However, this landslide is proximal to the active fault and the bedrock here may have been continuously weakened due to ongoing seismicity. Permafrost thaw due to accelerated climatic warming in the late 20th Century may also have been a contributing factor. Additionally, increased precipitation in the three years potentially surrounding the event could have facilitated any internal failure mechanisms in the slope.

Once future studies provide more and better resolution age controls on landslides and paleoseismicity in the region, it may be possible to determine an earthquake – landslide frequency relationship, thereby increasing our understanding of landslide hazards in southwestern Yukon. More so, as climate change accelerates, the impact of a warming climate on permafrost thaw will likely increase the frequency of events in subarctic regions (Chiarle *et al.,* 2021). Further studies should examine the effects of permafrost degradation on the frequency and intensity of landslides in the

Kluane Lake region as climate warming will likely be a prominent influence in the decades to come.

Chapter 4. Summary and Future Research

This thesis has improved our understanding of the age and potential triggering factors for landslides in the Kluane Lake area, Yukon. With high, steep, glaciated mountains, the area is prone to a range of surficial and bedrock related landslides. With the area being a major highway corridor (Alaska Highway), home to several communities, and a national park, increasing the base knowledge of landslides in the area is important.

Most slope stability studies in the area focused on historical landslides such as the Mt. Steele Rock avalanche (Lipovsky *et al*., 2008), Vulcan Creek rock slide (Brideau *et al.*, 2016, 2019), and the Congdon Creek Rock Avalanche (Thurber Consultants, 1989; Everard, 1994) and other landslides such as debris floods and flows, that affected the Alaska Highway or other infrastructure (Clague, 1981; Huscroft *et al.,* 2004; Koch *et al.,* 2014; Blais-Stevens & Behnia, 2016).

Some of the pre-historic landslides in this thesis were previously examined and contributed to the background understanding of the landslides investigated in this study. For example, radiocarbon ages at Sheep Mountain helped constrain the timing of the landslide; additionally, the previous identification of two phases provided a framework for landslide chronology at Sheep Mountain (Clague, 1981). Radiocarbon ages from below the proposed older phase indicated it was younger than ~2.0 cal kyr BP. Initially these two morphologically distinct phases were thought to be separated in time by at least 1000 years, but chronologic control on the younger phase was poor. The main difference was that WRT (1170-1097 cal yr BP) was found on the older phase and not on the younger phase. Another previous study, Brideau *et al.* (2005), examined the structural properties of the failure scarp at Aishihik to postulate contributing factors to the landslide; jointing, foliations and weak rock were all determined to have contributed to the failure. Although the Aishihik landslide was presumed to have occurred sometime in the early Holocene (Huscroft *et al.,* 2004), a precise age was unknown. Both Gladstone-1 and 2 and Generc were previously identified in regional mapping exercises. However, they were not examined in the field so there was no detailed description nor estimate of their age other than the label of postglacial (Gladstone-1 and 2) or recent (Generc) (Rampton,

1979b). This thesis better constrained the ages of these landslides and attempted to determine possible triggers through correlation to potential seismic or climatic events.

The objectives of this study were to use different chronological dating techniques to obtain ages for five landslides as well as to correlate these events to potential triggers. These new ages are an important contribution to the long-term goal of providing chronological constraints to southwest Yukon's regional paleoseismicity and landslide hazard assessment. Although a significant contribution, given the number of landslides and unstable ground in the area, suggestions for future work will be given in section 4.2.

4.2. Summary of Landslides, Ages, and Triggering Mechanisms

The primary objective of this thesis was to contribute five new landslide ages to the study of landslides in southwest Yukon, these ages are summarized below: (1) Sheep Mountain – ~2.0 cal kyr BP, (2) Aishihik – 5.7 ± 0.4 kyr BP, (3) Gladstone-1 – 10.5 ± 0.3 kyr BP, and (4) Gladstone-2 – 11.2 ± 0.3 kyr BP (5) Generc 1996-97 CE (Fig. 4.1). Generc was omitted from this figure since it was a historical rock slide.

The second objective of this thesis was to correlate these landslide ages to either periods of seismicity on the Denali fault or warmer paleoclimatic conditions during the Holocene. This was achieved through an extensive literature review of paleolimnological and paleoseismological studies in Southwest Yukon. Each landslide was linked to one of these triggering mechanisms.

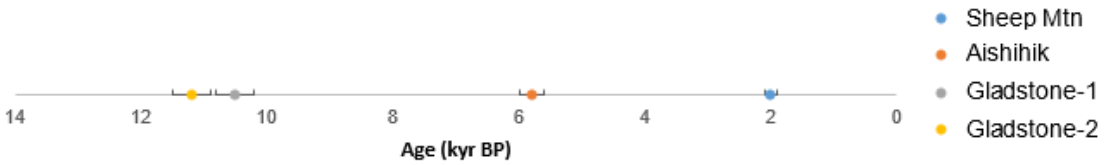

Figure 4.1. Summary timeline of four of the landslides studied in the study area. As Generc occurred in modern time, it is not on this time scale.

The 5-10x10^6 m^3 Sheep Mountain rock avalanche is in close proximity to the Denali fault with the Alaska Highway built over its deposits (Clague, 1981). Chronology

was provided by a combination of radiocarbon ages bracketing the proposed older phase as well as ^{36}Cl ages from both phases. Radiocarbon ages from a newly discovered site above the older phase yield ages nearly identical to the ages from below, *ca.* 2.0 cal kyr BP. ^{36}Cl ages from both phases are nearly identical thus it was concluded that these two phases were penecontemporaneous; the difference in morphology between the two phases is most likely due to the outer margins of the landslide eroding and incorporating finer material, causing it to appear more subdued and promoting more vegetation growth. A paleoseismic trigger was inferred likely due to the proximity of the rock slide to the Denali fault which is ~3.5 km away. There are two previously identified seismic events that can potentially account for Sheep Mountain: a paleoearthquake at ~2.2 cal kyr BP (Seitz et al. 2008) or 1.9 – 1.2 cal kyr BP (Blais-Stevens *et al.,* 2020). We think it is likely the earthquake that occurred ~2.0 cal kyr BP triggered the Sheep Mountain landslide and if this landslide is co-seismic, we propose that our ages better constrain the timing of the paleoearthquake previously documented.

The Aishihik landslide occurred *ca*. 5.7 $\pm$ 0.4 kyr BP. Two prominent ridges were sampled to obtain a transect of the rock slide; these were found to have occurred simultaneously based on ^{10}Be ages and landslide morphology. This landslide could have been triggered by a paleoseismic event that occurred between 6.2 – 6.0 cal kyr BP (Seitz *et al.* 2008) or 5.9 – 6.2 (Blais-Stevens *et al.,* 2020); but this landslide is ~50 km from the Denali fault so it is less likely seismically induced. With only one landslide, it can not be confirmed that it is co-seismic; several more landslides would have to be dated to the same time to corroborate this hypothesis. Additionally, based on lake sediment core data from Hanging Lake, landslide initiation may have occurred due to warmer and wetter temperatures during this period (Kurek *et al.*, 2009). These conditions would have thawed underlying permafrost, exacerbating already precarious slope stability conditions in this extensively faulted and fractured rock (Brideau *et al.* 2005).

Both Gladstone rock slides occurred in the Ruby Ranges; Gladstone-1 occurred in a cirque valley north of Kluane Lake and was ^{10}Be dated to 10.5 ± 0.3 kyr BP whereas Gladstone-2 occurred to the east of Gladstone-1 in a meltwater channel and was also ^{10}Be dated to 11.2 $\pm$ 0.3 kyr BP. These rock slides were most likely conditioned due to glacial debutressing in the valleys following deglaciation and by increased permafrost

thaw due to rapid warming in the early Holocene. An exact triggering mechanism is not yet determined at this time.

The Generc landslide was dated with a combination of air photo analysis, field observations, and dendrochronology. Based on tree ring analysis, the Generc rock slide most likely occurred between 1996-1997 CE. Although it was not specifically linked to a distinct seismic event, the rock slide is only 2 km southwest of the Denali fault and bedrock within the Kluane Ranges may have been fractured due to constant seismic activity in the area. Molards found on the deposit were also indicative of permafrost within the failure; permafrost thaw may have conditioned the slope prior to failure.

4.3. Future Work

4.3.2. ^{36}Cl Exposure Dating

Due to the COVID-19 pandemic, laboratory work was either postponed or cancelled for public safety reasons, affecting this research. Not only did this delay the lab analysis, but this also inhibited a proposed aspect of the ^{36}Cl dating, which involved developing a better method to measure ^{35}Cl. While ^{35}Cl was carefully removed from thesis samples using magnetic separation, studying ^{35}Cl will assist in future ^{36}Cl exposure dating.

This rare isotope is produced by cosmic ray particle interactions with exposed atoms in bombarded rocks. One production pathway is when the most abundant chlorine isotope, ^{35}Cl, captures a slow (thermal) cosmogenic neutron (n_{th}) (Eq. 4.1).

$$^{35}_{17}Cl\{n_{th,},\gamma\}^{36}_{17}Cl \qquad \textit{Eq. 4.1}$$

To quantify this n_{th} capture and resultant ^{36}Cl production, the abundance of ^{35}Cl in the rock must be known. Typically, the concentration of ^{35}Cl is determined by using an isotope dilution approach which involves spiking the sample with a carrier of known isotopic composition. Then, with enough defined variables to reduce the degrees of freedom, it is possible to estimate the concentration of ^{35}Cl using just AMS measurements. However, there are many unconstrained assumptions and challenging measurements in this approach, (Table 4.1).

Table 4.1. Summary of the known and unknown variables associated with Cl-36 exposure dating and AMS measurements. NAR = natural abundance ratio.

	^{35}Cl	^{36}Cl	^{37}Cl	$^{35/37}Cl$
Sample	**?**	**?**	**?**	NAR
Carrier	Known	Known	Known	Known
Contamination	**?**	**?**	**?**	**?**
AMS Blank	Known	**?**	Known	**?**

^{35}Cl measurements can be improved by using Cl from the Windsor Fm Pugwash Salt mine which has a low ^{36}Cl concentration and a $^{35}Cl/^{37}Cl$ natural abundance ratio of 3.087. This novel study would have measured the Cl elemental abundance in the samples using the CRISDal Lab ICP-OES to verify the AMS isotope dilution approach. ^{36}Cl is less commonly used in TCN dating as compared to ^{10}Be. By obtaining better analytical measurements, ^{36}Cl could be used more extensively and more accurately in exposure dating landslides.

4.3.3. Further analysis of Sheep Mountain

Although it is the best dated of all the landslides, one final question remains: is the lack of White River Tephra on the proposed younger phase of the landslide due to a lack of preservation or are the ^{36}Cl ages wrong? This can be answered by a more detailed field examination looking for tephra between the boulders closer to the centre of the landslide as well as the soils near the Northern Roadcut section.

4.3.4. Earthquakes and Their Impact on Landslide Distribution

We had hoped to identify more co-seismic landslides but that proved difficult. Although there are many “landslides” in the area due to the rock types present, most were not discrete events, but more long-term continuous rockfall. TCNs could be used to date numerous boulders on these episodically active landslides, but it would be very expensive and time consuming; further studies will be required to continue this research.

In this project, landslides were correlated to periods of paleoseismicity during the Holocene. This was accomplished through landslide age calculations and literature

reviews of paleoseismic research in the area (Seitz *et al.,* 2008; Blais-Stevens *et al.,* 2020). If more landslides are dated in the Kluane Lake region and their genesis is found to be linked to paleoseismicity, then features of these paleoearthquakes can be estimated (*cf.* Jibson, 2009). Such features as earthquake magnitude can be ascertained from a landslide or group of landslides in a region. Keefer's (1984, 2002) comprehensive analysis of 300 landslides triggered by historical earthquakes determined that earthquakes with a magnitude of $\geq$ 4.0 are able to trigger rock slides, and earthquakes with a magnitude of $\geq$ 6.0 can trigger rock avalanches. In a later study, the average area affected by landslides (A, in km^2) was predicted as a function of earthquake magnitude (M; a composite magnitude with surface-wave magnitudes below 7.5 and moment magnitudes above 7.5) (Eq. 4.2) (Keefer, 1984; Keefer & Wilson, 1989).

$$\log A = M - 3.46 \pm 0.47 \qquad \textit{Eq. 4.2}$$

This relationship is controlled by local geologic conditions, but as the climate warms and permafrost degradation increases, the minimum earthquake magnitude required to trigger landslides (*i.e.* $\geq$ 4.0) could be reduced. This would then impact the "area affected by landslides" variable due to a lower landslide-initiation threshold. However, landslides triggered by permafrost degradation will still occur regardless of earthquake activity and is something to consider in future studies.

More dated landslides in the Kluane Lake area and further modelling of landslide-earthquake relationships will benefit future hazard assessments in the region. The study area contains many landslide hazards that are only going to become more frequent as climate change accelerates. Understanding when and why these landslides occur will be necessary for future developments in the area. While this thesis is only the first step in chronologically constraining discrete landslide events in the Kluane Lake area, the determination of five new landslide ages and their potential triggering/conditioning mechanisms is an essential contribution to the understanding of hazards in this major transportation corridor.

References

Anderson, L., Abbott, M. B., Finney, B. P., & Burns, S. J. (2005). Regional atmospheric circulation change in the North Pacific during the Holocene inferred from lacustrine carbonate oxygen isotopes, Yukon Territory, Canada. Quaternary Research, 64(1), 21-35.

Antinao, J. L., & Gosse, J. (2009). Large rockslides in the Southern Central Andes of Chile (32-34.5°S): Tectonic control and significance for Quaternary landscape evolution. Geomorphology, 104(3–4), 117–133. https://doi.org/10.1016/j.geomorph.2008.08.008

Balco, G. (2017). Production rate calculations for cosmic-ray-muon-produced 10Be and 26Al benchmarked against geological calibration data. Quaternary Geochronology, 39, 150–173. https://doi.org/10.1016/J.QUAGEO.2017.02.001

Balco, G., Stone, J. O., Lifton, N. A., & Dunai, T. J. (2008). A complete and easily accessible means of calculating surface exposure ages or erosion rates from 10Be and 26Al measurements. Quaternary geochronology, 3(3), 174-195.

Ballantyne, C. K. (2002). Paraglacial geomorphology. Quaternary Science Reviews, 21(18-19), 1935-2017.

Barnes, S.D. (1997). The sedimentology and paleogeography of Glacial Lake Champagne, southern Yukon Territory. Unpublished M.A. thesis, Carleton University, Ontario. 109 p.

Blais-Stevens, A., & Behnia, P. (2016). Debris flow susceptibility mapping using a qualitative heuristic method and Flow-R along the Yukon Alaska Highway Corridor, Canada. Natural Hazards and Earth System Sciences, 16(2), 449-462.

Bell, R., & Glade, T. (2004). Quantitative risk analysis for landslides–Examples from Bíldudalur, NW-Iceland. Natural Hazards and Earth System Sciences, 4(1), 117-131.

Bender, A. M., & Haeussler, P. J. (2017). Eastern Denali Fault surface trace map, eastern Alaska and Yukon, Canada. U.S. Geological Survey Open-File Report 2017–1049, 1–10. https://doi.org/https://doi.org/10.3133/ofr20171049

Berglund, B. E., Ralska-Jasiewiczowa, M. (1986). Handbook of Holocene palaeoecology and palaeohydrology. International Geological Correlation Programme. Project 158B. J. Wiley. https://inis.iaea.org/search/search.aspx?orig_q=RN:19026440

Bessette-Kirton, E. K., & Coe, J. A. (2020). A 36-Year Record of Rock Avalanches in the Saint Elias Mountains of Alaska, with Implications for future hazards. Frontiers in Earth Science, 8(July), 1–23. https://doi.org/10.3389/feart.2020.00293

Blais-Stevens, A., Clague, J. J., Brahney, J., Lipovsky, P., Haeussler, P. J., & Menounos, B. (2020). Evidence For large Holocene earthquakes along the Denali Fault in Southwest Yukon, Canada. Environmental and Engineering Geoscience, XXVI(1), 1–18. https://doi.org/10.2113/eeg-2263

Blais-Stevens, A., Couture, R., Page, A., Koch, J., Clague, J. J., and Lipovsky, P. (2010) Landslide susceptibility, hazard and risk assessments along pipeline corridors in Canada. GeoCalgary2010, Proceedings of the 63rd Canadian Geotechnical Society conference; by Canadian Geotechnical Society: p. 878-885.

Böhme, M., Hermanns, R. L., Gosse, J., Hilger, P., Eiken, T., Lauknes, T. R., & Dehls, J. F. (2019). Comparison of monitoring data with paleo-slip rates: Cosmogenic nuclide dating detects acceleration of a rockslide. Geology, 47(4), 339–342. https://doi.org/10.1130/G45684.1

Bond, J., (2004). Late Wisconsinan McConnell glaciation of the Whitehorse map area (105D), Yukon. In: Yukon Exploration and Geology 2003, D.S. Emond and L.L. Lewis (eds.), Yukon Geological Survey, 73-88.

Bonnaventure, P. P., Lewkowicz, A. G., Kremer, M., & Sawada, M. C. (2012). A permafrost probability model for the southern Yukon and northern British Columbia, Canada. Permafrost and Periglacial Processes, 23(1), 52-68 https://doi.org/10.1002/ppp.1733

Boucher, G., & Fitch, T. J. (1969). Microearthquake Seismicity of the Denali Fault. Journal of Geophysical Research, 74(27), 6638–6648.

Bradley, R. S., (1985). Quaternary Paleoclimatology: Methods of Paleoclimatic Reconstruction. Chapman and Hall, London, UK. 467-468.

Brideau, M. A. (2014). Introduction: Application of Numerical Modelling Techniques to Landslides. In Landslide Science for a Safer Geoenvironment (pp. 235-236). Springer, Cham.

Brideau, M. A., & Roberts, N. J. (2022). Landslides in bedrock. In Landslide Hazards, Risks, and Disasters Chapter 3, (pp. 43-97). Elsevier. https://doi.org/10.1016/B978-0-12-818464-6.00002-0

Brideau, M. A., Shugar, D. H., Bevington, A. R., Willis, M. J., & Wong, C. (2019). Evolution of the 2014 Vulcan Creek landslide-dammed lake, Yukon, Canada, using field and remote survey techniques. Landslides, 16(10), 1823–1840. https://doi.org/10.1007/s10346-019-01199-3

Brideau, M. A., Shugar, D. H., & Wong, C. (2016). Preliminary investigation of the 2014 Vulcan Creek landslide dam, Kluane National Park and Reserve, Yukon. In Proceedings of the 69th Canadian Geotechnical Conference, Vancouver Canada, Paper (Vol. 3902).

Brideau, M. A., Stead, D., Huscroft, C., & Fecova, K. (2005). Quaternary, structural and engineering geology of the Aishihik River landslide, Cracker Creek Area (NTS 115A/15), Yukon. Yukon Exploration and Geology 2004, 83-94.

Brideau, M. A., Stead, D., Lipovsky, P., Jaboyedoff, M., Hopkinson, C., Demuth, M., ... & Delaney, K. (2009). Preliminary description and slope stability analyses of the 2008 Little Salmon Lake and 2007 Mt. Steele landslides, Yukon. Yukon exploration and geology, 110-133.

Bronk Ramsey, C. (2009). Bayesian analysis of radiocarbon dates. Radiocarbon, 51(1), 337–360.

Bruhn, R. L., Sauber, J., Cotton, M. M., Pavlis, T. L., Burgess, E., Ruppert, N., & Forster, R. R. (2012). Plate margin deformation and active tectonics along the northern edge of the Yakutat Terrane in the Saint Elias Orogen, Alaska, and Yukon, Canada. Geosphere, 8(6), 1384–1407. https://doi.org/10.1130/GES00807.1

Bunbury, J., & Gajewski, K. (2009). Postglacial climates inferred from a lake at treeline, southwest Yukon Territory, Canada. Quaternary Science Reviews, 28(3–4), 354–369. https://doi.org/10.1016/j.quascirev.2008.10.007

Bunbury, J., & Gajewski, K. (2012). Temperatures of the past 2000 years inferred from lake sediments, southwest Yukon Territory, Canada. Quaternary Research, 77(3), 355–367. https://doi.org/10.1016/j.yqres.2012.01.002

Bykova, A. (2020). Permafrost thaw in a warming world: The Arctic Institute's permafrost series fall-winter 2020. The Arctic Institute website, October 1, 2020. Available at https://www.thearcticinstitute.org/permafrost-thaw-warming-world-arctic-institute-permafrost-series-fall-winter-2020/ (accessed January 10, 2021).

Byokava, A. (2021). Permafrost Thaw in the Warming Arctic: Final Remarks. The Arctic Institute's permafrost series fall-winter 2021. April 13, 2021. Available at https://www.thearcticinstitute.org/permafrost-thaw-warming-arctic-final-remarks/. (accessed January 10, 2021).

Cairnes, D.D. (1915). Exploration in southwestern Yukon. Summary Report of the Geological Survey Department of Mines for the calendar year 1914. Sessional paper No. 26-1915. Retrieved from https://publications.gc.ca/collections/collection_2017/rncan-nrcan/M41-2-1914-eng.pdf

Cassie, J. W., Gassen, W. V., & Cruden, D. M. (1988). Laboratory analogue of the formation of molards, cones of rock-avalanche debris. Geology, 16(8), 735-738.

Chen, W., Pourghasemi, H. R., & Naghibi, S. A. (2018). Prioritization of landslide conditioning factors and its spatial modeling in Shangnan County, China using GIS-based data mining algorithms. Bulletin of Engineering Geology and the Environment, 77(2), 611-629.

Chiarle, M., Geertsema, M., Mortara, G., & Clague, J. J. (2021). Relations between climate change and mass movement: Perspectives from the Canadian Cordillera and the European Alps. Global and Planetary Change, 202(October 2020), 103499. https://doi.org/10.1016/j.gloplacha.2021.103499

Chmeleff, J., von Blanckenburg, F., Kossert, K., & Jakob, D. (2010). Determination of the 10Be half-life by multicollector ICP-MS and liquid scintillation counting. Nuclear Instruments and Methods in Physics Research, Section B: Beam Interactions with Materials and Atoms, 268(2), 192–199. https://doi.org/10.1016/j.nimb.2009.09.012

Christeson, G. L., Gulick, S. P. S., van Avendonk, H. J. A., Worthington, L. L., Reece, R. S., & Pavlis, T. L. (2010). The Yakutat terrane: Dramatic change in crustal thickness across the transition fault, Alaska. Geology, 38(10), 895–898. https://doi.org/10.1130/G31170.1

Clague, J. J. (1981). Landslides at the south end of Kluane Lake, Yukon Territory. Canadian Journal of Earth Sciences, 18(5), 959–971. https://doi.org/10.1139/e81-092

Clague, J. J. (1979). The Denali fault system in southwest Yukon Territory: a geologic hazard. Current Research Part A, Geological Survey of Canada, Paper, 79, 169-178.

Clague, J. J., Jozsa, L. A., & Parker, M. L. (1982). Dendrochronological dating of glacier-dammed lakes: an example from Yukon Territory, Canada. Arctic & Alpine Research, 14(4), 301–310. https://doi.org/10.2307/1550793

Clegg, B. F., Clarke, G. H., Chipman, M. L., Chou, M., Walker, I. R., Tinner, W., & Hu, F. S. (2010). Six millennia of summer temperature variation based on midge analysis of lake sediments from Alaska. Quaternary Science Reviews, 29(23–24), 3308–3316. https://doi.org/10.1016/j.quascirev.2010.08.001

Clegg, B. F., Kelly, R., Clarke, G. H., Walker, I. R., & Hu, F. S. (2011). Nonlinear response of summer temperature to holocene insolation forcing in Alaska. Proceedings of the National Academy of Sciences of the United States of America, 108(48), 19299–19304. https://doi.org/10.1073/pnas.1110913108

Cobbett, R., Israel, S., Mortensen, J., Joyce, N., & Crowley, J. (2017). Structure and kinematic evolution of the Duke River fault, Southwestern Yukon. Canadian Journal of Earth Sciences, 54(3), 322–344. https://doi.org/10.1139/cjes-2016-0074

Cronmiller, D., Ward, B. and Bond, J.D. (2018). Surficial geology of Gladstone Creek (NTS 115G/8 and part of 115G/7). Yukon Geological Survey, Open File 2018-20, scale 1:50000.

Cronmiller, D. (2019). Surficial geology, stratigraphy, and placer deposits of the Ruby Range, Yukon Territory (Master's thesis, Department of Earth Sciences, Simon Fraser University). 165 p.

Cwynar, L. C. (1982). A Late-Quaternary Vegetation History from Hanging Lake, Northern Yukon: Ecological Archives M052-001. Ecological Monographs, 52(1), 1-24.

Daniels, L. D., Yocom Kent, L. L., Sherriff, R. L., & Heyerdahl, E. K. (2017). Deciphering the complexity of historical fire regimes: Diversity among forests of western North America. In Dendroecology: tree-ring analyses applied to ecological studies. Edited by M.M. Amoroso, L.D. Daniels, P.J. Baker, and J.J. Camarero. Springer, Cham, Switzerland. pp. 185–210.

Day, K.M., & Fan, C.Y. (1986). Bomb-produced 14C content in tree rings grown at different latitudes. Radiocarbon 28(2A), 346–9.

Delunel, R., Bourlès, D. L., van der Beek, P. A., Schlunegger, F., Leya, I., Masarik, J., & Paquet, E. (2014). Snow shielding factors for cosmogenic nuclide dating inferred from long-term neutron detector monitoring. Quaternary Geochronology, 24, 16–26. https://doi.org/10.1016/j.quageo.2014.07.003

Dodds, C. J., & Campbell, R. B. (1992). Overview, legend, and mineral deposit tabulations for geology of SW Kluane Lake (115G & F [E1/2]), Mount Saint Elias (115B & C [E1/2]), SW Dezadeash (115A), NE Yakutat (114O), and Tatshenshini (114P) map areas, Yukon Territory and British Columbia. Geological Survey of Canada, Open Files, 2188(2191), 85.

Doig, R. (1998). Paleoseismological evidence from lake sediments for recent movement on the Denali and other faults, Yukon Territory, Canada. Tectonophysics, 296(3–4), 363–370. https://doi.org/10.1016/S0040-1951(98)00152-8

Doser, D. I. (2014). Seismicity of Southwestern Yukon, Canada, and its relation to slip transfer between the Fairweather and Denali fault systems. Tectonophysics, 611, 121–129. https://doi.org/10.1016/j.tecto.2013.11.018

Dramis, F., Govi, M., Guglielmin, M., & Mortara, G. (1995). Mountain permafrost and slope instability in the Italian Alps: the Val Pola landslide. Permafrost and Periglacial Processes, 6(1), 73-81.

Duk-Rodkin, A. (1999). Glacial limits map of Yukon Territory. Geological Survey of Canada, Open File, 3694(1), 1.

Dunai, T. J., Binnie, S. A., Hein, A. S., & Paling, S. M. (2014). The effects of a hydrogen-rich ground cover on cosmogenic thermal neutrons: Implications for exposure dating. Quaternary Geochronology, 22, 183–191. https://doi.org/10.1016/j.quageo.2013.01.001

Eberhart-Phillips, D., Haeussler, P. J., Freymueller, J. T., Frankel, A. D., Rubin, C. M., Craw, P., ... & Wallace, W. K. (2003). The 2002 Denali fault earthquake, Alaska: A large magnitude, slip-partitioned event. Science, 300(5622), 1113-1118.

Elliott, J., & Freymueller, J. T. (2020). A Block Model of Present-Day Kinematics of Alaska and Western Canada. Journal of Geophysical Research: Solid Earth, 1–30. https://doi.org/10.1029/2019jb018378

Enkelmann, E., Koons, P. O., Pavlis, T. L., Hallet, B., Barker, A., Elliott, J., Garver, J. I., Gulick, S. P. S., Headley, R. M., Pavlis, G. L., Ridgway, K. D., Ruppert, N., & van Avendonk, H. J. A. (2015). Cooperation among tectonic and surface processes in the St. Elias Range, Earth's highest coastal mountains. Geophysical Research Letters, 42(14), 5838–5846. https://doi.org/10.1002/2015GL064727

Environment Canada (2022). Climate Normals & Averages 1981-2010. Government of Canada / gouvernement du Canada. Climate. Retrieved April 28, 2022, from https://climate.weather.gc.ca/climate_normals/results_1981_2010_e.html?searchType=stnName&txtStationName=burwash&searchMethod=contains&txtCentralLatMin=0&txtCentralLatSec=0&txtCentralLongMin=0&txtCentralLongSec=0&stnID=1525&dispBack=1

Everard, K. A. (1994). Regional characterization of large landslides in southwest Yukon, with emphasis on the role of neotectonics (Doctoral dissertation, University of British Columbia). 165 p.

Fan, X., Yunus, A. P., Scaringi, G., Catani, F., Siva Subramanian, S., Xu, Q., & Huang, R. (2021). Rapidly evolving controls of landslides after a strong earthquake and implications for hazard assessments. Geophysical Research Letters, 48(1), e2020GL090509.

Fernandes, N. F., Guimarães, R. F., Gomes, R. A., Vieira, B. C., Montgomery, D. R., & Greenberg, H. (2004). Topographic controls of landslides in Rio de Janeiro: field evidence and modeling. Catena, *55*(2), 163-181.

Filion, L., Payette, S., Gauthier, L., & Boutin, Y. (1986). Light rings in subarctic conifers as a dendrochronological tool. Quaternary Research, 26(2), 272-279.

Fisher, D., Wake, C., Kreutz, K., Yalcin, K., Steig, E., Mayewski, P., ... & Burns, S. (2004). Stable isotope records from Mount Logan, Eclipse ice cores and nearby Jellybean Lake. Water cycle of the North Pacific over 2000 years and over five vertical kilometres: sudden shifts and tropical connections. Géographie physique et Quaternaire, 58(2-3), 337-352.

Gabet, E. J. (2003). Sediment transport by dry ravel. Journal of Geophysical Research: Solid Earth, 108, 2049. doi:10.1029/2001JB001686

Gajewski, K., Bunbury, J., Vetter, M., Kroeker, N., & Khan, A. H. (2014). Paleoenvironmental studies in southwestern Yukon. *Arctic*: The Kluane Lake Research Station: 50 Years of Northern Science, 67, Supplement 1, 58-70.

Gaines, P. R. (2011). ICP operations guide. A guide for using ICP-OES and ICP-MS.: Inorganic Ventures, 44, 4-8.

Garriss, R. N. (2019). Modeling Surface Roughness as an Indicator of Age and Landslide Susceptibility, and the Spatial Inventory of Prehistoric Landslides: Green River Valley, Washington (Doctoral dissertation, Portland State University).

Geertsema, M., & Pojar, J. J. (2007). Influence of landslides on biophysical diversity—a perspective from British Columbia. Geomorphology, 89(1-2), 55-69. https://doi.org/10.1016/j.geomorph.2006.07.019

Gilbert, R., & Desloges, J. R. (2005). The record of Glacial Lake Champagne in Kusawa Lake, southwestern Yukon Territory. Canadian Journal of Earth Sciences, 42(12), 2127–2140. https://doi.org/10.1139/e05-094

Gorum, T., Korup, O., van Westen, C. J., van der Meijde, M., Xu, C., & van der Meer, F. D. (2014). Why so few? Landslides triggered by the 2002 Denali earthquake, Alaska. Quaternary Science Reviews, 95, 80–94. https://doi.org/10.1016/j.quascirev.2014.04.032

Gosse, J.C., & Klein, J. (2015). Terrestrial cosmogenic nuclide dating. In W. J. Rink & J. W. Thompson (Eds.), Encyclopedia of Scientific Dating Methods (Vol. 29, pp. 799–813). New York: Springer. https://doi.org/10.1007/978-94-007-6304-3_148

Gosse, J. C., & Phillips, F. M. (2001). Terrestrial in situ cosmogenic nuclides: theory and application. Quaternary Science Reviews, 20(14), 1475-1560.

Grämiger, L. M., Moore, J. R., Gischig, V. S., Ivy-Ochs, S., & Loew, S. (2017). Beyond debuttressing: Mechanics of paraglacial rock slope damage during repeat glacial cycles. Journal of Geophysical Research: Earth Surface, 122(4), 1004–1036. https://doi.org/10.1002/2016JF003967

Greene, A. R., Scoates, J. S., Weis, D., & Israel, S. (2004). Flood basalts of the Wrangellia Terrane, southwest Yukon: Implications for the formation of oceanic plateaus, continental crust and Ni-Cu-PGE mineralization. Yukon exploration and geology, 109-120.

Gruber, S., Burn, C.R., Arenson, L., Geertsema, M., Harris, S., Smith, S.L., Bonnaventure, P., and Benkert, B. (2015). Permafrost in mountainous regions of Canada. Paper 169. Proceedings, 68th Canadian Geotechnical Conference and 7th Canadian Permafrost Conference, Canadian Geotechnical Society, pp. 8.

Guthrie, R. H. (2013). Socio-Economic Significance: Canadian Technical Guidelines and Best Practices Related to Landslides: A National Initiative for Loss Reduction, Open File 7311, pp. 1-19. https://doi.org/10.4095/292241

Guzzetti, F., Ardizzone, F., Cardinali, M., Rossi, M., & Valigi, D. (2009). Landslide volumes and landslide mobilization rates in Umbria, central Italy. Earth and Planetary Science Letters, 279(3–4), 222–229. https://doi.org/10.1016/j.epsl.2009.01.005

Haeussler, P. J., Matmon, A., Schwartz, D. P., & Seitz, G. G. (2017). Neotectonics of interior Alaska and the late Quaternary slip rate along the Denali fault system. Geosphere, 13(5), 1445-1463.

Haeussler, P. J., Schwartz, D. P., Dawson, T. E., Stenner, H. D., Lienkaemper, J. J., Sherrod, B., Cinti, F. R., Montone, P., Craw, P. A., Crone, A. J., & Personius, S. F. (2004). Surface rupture and slip distribution of the Denali and totschunda faults in the 3 November 2002 M 7.9 earthquake, Alaska. Bulletin of the Seismological Society of America, 94(6 SUPPL. B), 23–52. https://doi.org/10.1785/0120040626

Harris, S. A., & Mcdermid, G. (1998). Frequency of debris flows on the Sheep Mountain fan, Kluane Lake, Yukon Territory. Zeitschrift Fur Geomorphologie, 42(2), 159–175.

He, X., Ni, S., Zhang, P., & Freymueller, J. (2018). The 1 May 2017 British Columbia-Alaska Earthquake Doublet and Implication for Complexity Near Southern End of Denali Fault System. Geophysical Research Letters, 45(12), 5937–5947. https://doi.org/10.1029/2018GL078014

Heginbottom, J. A., Dubreuil, M. A., & Harker, P. A. (1995). Canada, Permafrost. National Atlas of Canada. Natural Resources Canada, 5th Edition, MCR, 4177.

Hervás, J., & Bobrowsky, P. (2009). Mapping: inventories, susceptibility, hazard and risk. In *Landslides–disaster risk reduction* (pp. 321-349). Springer, Berlin, Heidelberg.

Hewitt, K., Gosse, J., & Clague, J. J. (2011). Rock avalanches and the pace of late Quaternary development of river valleys in the Karakoram Himalaya. Bulletin of the Geological Society of America, 123(9–10), 1836–1850. https://doi.org/10.1130/B30341.1

Heyman, J., Applegate, P. J., Blomdin, R., Gribenski, N., Harbor, J. M., & Stroeven, A. P. (2016). Boulder height - exposure age relationships from a global glacial 10Be compilation. Quaternary Geochronology, 34, 1–11. https://doi.org/10.1016/j.quageo.2016.03.002

Hickman, R. G., Craddock, C., & Sherwood, K. W. (1978). The Denali fault system and the tectonic development of southern Alaska. Tectonophysics, 47(3-4), 247-273.

Hilger, P., Gosse, J. C., & Hermanns, R. L. (2019). How significant is inheritance when dating rockslide boulders with terrestrial cosmogenic nuclide dating?—a case study of an historic event. Landslides, 16(4), 729–738. https://doi.org/10.1007/s10346-018-01132-0

Hilger, P., Hermanns, R. L., Czekirda, J., Myhra, K. S., Gosse, J. C., & Etzelmüller, B. (2021). Permafrost as a first order control on long-term rock-slope deformation in (Sub-)Arctic Norway. Quaternary Science Reviews, 251, 106718. https://doi.org/10.1016/j.quascirev.2020.106718

Hilger, P., Hermanns, R. L., Gosse, J. C., Jacobs, B., Etzelmüller, B., & Krautblatter, M. (2018). Multiple rock-slope failures from Mannen in Romsdal Valley, western Norway, revealed from Quaternary geological mapping and 10Be exposure dating. Holocene, 28(12), 1841–1854. https://doi.org/10.1177/0959683618798165

Hughes, M. K. (2002). Dendrochronology in climatology–the state of the art. Dendrochronologia, 20(1-2), 95-116. https://doi.org/10.1078/1125-7865-00011

Hughes, O. L., Rutter, N. W. and Clague, J. J. (1989). Yukon Territory (Quaternary stratigraphy and history, Cordilleran Ice Sheet), p. 58-62. In R. J. Fulton, ed., Quaternary geology of Canada and Greenland. Geological Survey of Canada, Geology of Canada no. 1,839 p. (also Geological Society of America, The Geology of North America, v. K-1).

Hungr, O., Evans, S.G. and Hutchinson, I. (2001). A Review of the Classification of Landslides of the Flow Type. Environmental & Engineering Geoscience, 7(3), p. 221-238, doi:10.2113/gseegeosci.7.3.221

Hungr, O., Leroueil, S., & Picarelli, L. (2014). The Varnes classification of landslide types, an update. Landslides, 11(2), 167-194.

Huscroft, C. A., Lipovsky, P. S., & Bond, J. D. (2003). Permafrost and landslide activity: Case studies from southwestern Yukon Territory. Yukon Exploration and Geology, D.S. Emond and L.L. Lewis (eds.), Yukon Geological Survey 2003, 107–119 p.

Huscroft, C. A., Lipovsky, P. S., & Bond, J. D. (2004). A regional characterization of landslides in the Alaska Highway corridor, Yukon. Yukon Geological Survey, Open File 2004-18, 65 p., report and CD-ROM.

Hyndman, R. D., Flück, P., Mazzotti, S., Lewis, T. J., Ristau, J., & Leonard, L. (2005). Current tectonics of the northern Canadian Cordillera. Canadian Journal of Earth Sciences, 42(6), 1117-1136.

Israel, S., & Kim, R. (2014). Preliminary investigation into the geologic relationships in the Granite Lake area, parts of NTS 115A/10, 11, 14, and 15, southwest Yukon. In: Yukon Exploration and Geology 2013, K.E. MacFarlane, M.G. Nordling, and P.J. Sack (eds.), Yukon Geological Survey, p. 79-91.

Israel, S., Cobbett, R., and Fozard, C., (2007). Bedrock geology of the Koidern River area, Yukon (parts of NTS 115F/9, 15, 16 and 115G/12) (1:50 000 scale). Yukon Geological Survey, Open File 2007-8.

Israel, S., Murphy, D., Bennett, V., Mortensen, J., & Crowley, J. (2011). Yukon Exploration and Geology 2010 new insights into the geology and mineral potential of the Coast Belt in southwestern Yukon. Yukon Exploration and Geology Yukon Geological Research Yukon Exploration and Geology, 101–123.

Jackson, L. E., Ward, B., Duk-Rodkin, A., & Hughes, O. L. (1991). The last Cordilleran Ice Sheet in southern Yukon Territory. Geographie Physique et Quaternaire, 45(3), 341–354. https://doi.org/10.7202/032880ar

Jensen, B. J. L., Pyne-O'Donnell, S., Plunkett, G., Froese, D. G., Hughes, P. D. M., Sigl, M., McConnell, J. R., Amesbury, M. J., Blackwell, P. G., van den Bogaard, C., Buck, C. E., Charman, D. J., Clague, J. J., Hall, V. A., Koch, J., Mackay, H., Mallon, G., McColl, L., & Pilcher, J. R. (2014). Transatlantic distribution of the Alaskan White River Ash. Geology, 42(10), 875–878. https://doi.org/10.1130/G35945.1

Jibson, R. W. (2009). Using landslides for paleoseismic analysis. International geophysics, 95, 565-601. ISSN 0074-6142, DOI: 10.1016/S0074-6142(09)95008-2

Jibson, R. W., Harp, E. L., Schulz, W., & Keefer, D. K. (2006). Large rock avalanches triggered by the M 7.9 Denali Fault, Alaska, earthquake of 3 November 2002. Engineering Geology, 83(1–3), 144–160. https://doi.org/10.1016/j.enggeo.2005.06.029

Jorgensen, M. T., & Osterkamp, T. E. (2005). Response of boreal ecosystems to varying modes of permafrost degradation. Canadian Journal of Forest Research, 35(9), 2100-2111.

Keefer, D. K. (1984). Landslides caused by earthquakes: Discussion. Bulletin of the Geological Society of America, 95(7), 406–421. https://pubs.geoscienceworld.org/gsa/gsabulletin/article-abstract/95/4/406/202914/Landslides-caused-by-earthquakes?redirectedFrom=PDF

Keefer, D. K. (2002). Investigating landslides caused by earthquakes–a historical review. Surveys in geophysics, 23(6), 473-510.

Keefer, D.K., & Wilson, R.C. (1989). Predicting earthquake-induced landslides, with emphasis on arid and semi-arid region, California. US Geol. Survey Open-File Rep. Lanslides in a semi-arid environment, 2(Part 1), 118-149.

Kennedy, K.E. (2018). Evidence for limited glaciation in northern Kluane Range, southwestern Yukon, with implications for surficial geochemical exploration. In: Yukon Exploration and Geology 2017, K.E. MacFarlane (ed.), Yukon Geological Survey, 89-102.

Kennedy, K.E. and Ellis, S.E. (2020). Surficial geology of the northern Kluane Ranges (parts of NTS 115G/5, 6, 11, 12). Yukon Geological Survey, Open File 2020-5, 4 sheets, scale 1:50 000.

Koch, J. (2009). Improving age estimates for late Holocene glacial landforms using dendrochronology - 590 Some examples from Garibaldi Provincial Park, British Columbia. Quaternary Geochronology, 4, 130–139. 591 https://doi.org/10.1016/j.quageo.2008.11.002

Koch, J., Clague, J. J., & Blais-Stevens, A. (2014). Debris flow chronology and potential hazard along the Alaska highway in Southwest Yukon territory. Environmental and Engineering Geoscience, 20(1), 25–43. https://doi.org/10.2113/gseegeosci.20.1.25

Korschinek, G., Bergmaier, A., Faestermann, T., Gerstmann, U. C., Knie, K., Rugel, G., Wallner, A., Dillmann, I., Dollinger, G., von Gostomski, C. L., Kossert, K., Maiti, M., Poutivtsev, M., & Remmert, A. (2010). A new value for the half-life of 10Be by Heavy-Ion Elastic Recoil Detection and liquid scintillation counting. Nuclear Instruments and Methods in Physics Research, Section B: Beam Interactions with Materials and Atoms, 268(2), 187–191. https://doi.org/10.1016/j.nimb.2009.09.020

Kurek, J., Cwynar, L. C., & Vermaire, J. C. (2009). A late Quaternary paleotemperature record from Hanging Lake, northern Yukon Territory, eastern Beringia. Quaternary Research, 72(2), 246–257. https://doi.org/10.1016/j.yqres.2009.04.007

Lafrenière, M. J., & Lamoureux, S. F. (2019). Effects of changing permafrost conditions on hydrological processes and fluvial fluxes. Earth-science reviews, 191, 212-223.

Lagerbäck Adolphi, E. (2014). Characterization of Weathering Effects in Holocene Loess and Paleosol, Kluane Lake, Yukon, Canada. (Doctoral Dissertation, Uppsala University). 45 p. Retrieved from http://urn.kb.se/resolve?urn=urn:nbn:se:uu:diva-225849

Lahusen, S. R., Duvall, A. R., Montgomery, D. R., & Wartman, J. (2019). Landslides in Cascadia: Using geochronometry and spatial analysis to understand the timing, triggering and spatial distribution of slope failures in the Pacific Northwest United States. Unpublished PhD thesis, University of Washington, 93 p.

Lal, D. (1991). Cosmic ray labeling of erosion surfaces: in situ nuclide production rates and erosion models: Earth and Planetary Science Letters. Earth and Planetary Science Letters, 104(2–4), 424–439. http://trafficlight.bitdefender.com/info?url=http%3A//www.sciencedirect.com/science/article/pii/0012821X9190220C&language=en_US

Lamontagne, M., Halchuk, S., Cassidy, J. F., & Rogers, G. C. (2008). Significant Canadian earthquakes of the period 1600-2006. Seismological Research Letters, 79(2), 211–223. https://doi.org/10.1785/gssrl.79.2.211

Lanphere, M. A. (1978). Displacement History of the Denali Fault System, Alaska and Canada. Can J Earth Sci, 15(5), 817–822. https://doi.org/10.1139/e78-086

Lawrence, D. B. (1946). The technique of dating recent prehistoric glacial fluctuations from tree data. Mazama, 28(13), 57-59.

Leonard, L. J., Mazzotti, S., & Hyndman, R. D. (2008). Deformation rates estimated from earthquakes in the northern Cordillera of Canada and eastern Alaska. Journal of Geophysical Research: Solid Earth, 113(8), 1–18. https://doi.org/10.1029/2007JB005456

Lerbekmo, J.F., Westgate, J.A., Smith, D.G.W., & Denton, G.H. (1975). New data on the character and history of the White Rivervolcanic eruption, Alaska.InQuaternary studies.Edited byR.P.Suggate and M.M. Cresswell. The Royal Society of New Zeal-and, 203–20.

Lerbekmo, J. F. (2008). The White River Ash: Largest Holocene Plinian tephra. Canadian Journal of Earth Sciences, 45(6), 693–700. https://doi.org/10.1139/E08-023

Lewis, W. V. (1954). Pressure release and glacial erosion. Journal of Glaciology, *2*(16), 417-422.

Libby, W. F. (1954). Radiocarbon dating. Endeavour, 13(49), 5-16. Retrieved from https://www.nobelprize.org/uploads/2018/06/libby-lecture.pdf.

Lifton, N., Sato, T., & Dunai, T. J. (2014). Scaling in situ cosmogenic nuclide production rates using analytical approximations to atmospheric cosmic-ray fluxes. Earth and Planetary Science Letters, 386, 149–160. https://doi.org/10.1016/j.epsl.2013.10.052

Lipovsky, P. S., Evans, S. G., Clague, J. J., Hopkinson, C., Couture, R., Bobrowsky, P., Ekström, G., Demuth, M. N., Delaney, K. B., Roberts, N. J., Clarke, G., & Schaeffer, A. (2008). The July 2007 rock and ice avalanches at Mount Steele, St. Elias Mountains, Yukon, Canada. Landslides, 5(4), 445–455. https://doi.org/10.1007/s10346-008-0133-4

Liu, M. (2020). Evaluating thermal regime of cold region roads for climate change adaptation. (Master of Applied Science in Civil Engineering, University of Waterloo). 297 p.

Luckman, B. H., (1998). Dendroglaciologie dans les Rocheuses du Canada. Géographie physique et Quaternaire, 52, 139–151.

Malik, I., & Wistuba, M. (2012). Dendrochronological methods for reconstructing mass movements - an example of landslide activity analysis using tree-ring eccentricity. Geochronometria, 39(3), 180–196. https://doi.org/10.2478/s13386-012-0005-5

Maréchal, A., Mazzotti, S., Elliott, J. L., Freymueller, J. T., & Schmidt, M. (2015). Indentor-corner tectonics in the Yakutat-St. Elias collision constrained by GPS. Journal of Geophysical Research: Solid Earth, 120(5), 3897-3908.https://doi.org/10.1002/2014JB011842.

Maréchal, A., Ritz, J. F., Ferry, M., Mazzotti, S., Blard, P. H., Braucher, R., & Saint-Carlier, D. (2018). Active tectonics around the Yakutat indentor: New geomorphological constraints on the eastern Denali, Totschunda and Duke River Faults. Earth and Planetary Science Letters, 482, 71-80.

Margold, M., Gosse, J. C., Hidy, A. J., Woywitka, R. J., Young, J. M., & Froese, D. (2019). Beryllium-10 dating of the Foothills Erratics Train in Alberta, Canada, indicates detachment of the Laurentide Ice Sheet from the Rocky Mountains at ∼15 ka. Quaternary Research (United States), 92(2), 469–482. https://doi.org/10.1017/qua.2019.10

Margolis, E. Q., Swetnam, T. W., & Allen, C. D. (2007). A stand-replacing fire history in upper montane forests of the southern Rocky Mountains. Canadian Journal of Forest Research, 37(11), 2227-2241.

Marrero, S. M., Phillips, F. M., Borchers, B., Lifton, N., Aumer, R., & Balco, G. (2016a). Cosmogenic nuclide systematics and the CRONUScalc program. Quaternary Geochronology, 31, 160–187. https://doi.org/10.1016/j.quageo.2015.09.005

Marrero, S. M., Phillips, F. M., Caffee, M. W., & Gosse, J. C. (2016b). CRONUS-Earth cosmogenic 36Cl calibration. Quaternary Geochronology, 31, 199–219. https://doi.org/10.1016/j.quageo.2015.10.002

Marrero, S. M., Phillips, F. M., Caffee, M. W., & Gosse, J. (2021). Corrigendum to “CRONUS-Earth cosmogenic 36Cl calibration” [Quat. Geochronol. 31 (2016) 199–219]. Quaternary Geochronology, 61, 101130. https://doi.org/10.1016/J.QUAGEO.2020.101130

Matmon, A., Schwartz, D. P., Haeussler, P. J., Finkel, R., Lienkaemper, J. J., Stenner, H. D., & Dawson, T. E. (2006). Denali fault slip rates and Holocene-late Pleistocene kinematics of central Alaska. Geology, 34(8), 645–648. https://doi.org/10.1130/G22361.1

Mazzotti, S., & Hyndman, R. D. (2002). Yakutat collision and strain transfer across the northern Canadian Cordillera. Geology, 30(6), 495–498. https://doi.org/10.1130/0091-7613(2002)030<0495:YCASTA>2.0.CO;2

McCalpin, J. (1984). Preliminary age classification of landslides for inventory mapping. In Proceedings of the Annual Symposium on Engineering Geology and Soil Engineering, Vol. 21, pp. 99-120.

McColl, S. T., Davies, T. R. H., & McSaveney, M. J. (2010). Glacier retreat and rock-slope stability: debunking debuttressing. In 11th Congress of the International Association for Engineering Geology and the Environment (pp. 467-474). Auckland, New Zealand: CRC Press.

Meighan, L. N., Cassidy, J. F., Mazzotti, S., & Pavlis, G. L. (2013). Microseismicity and tectonics of southwest Yukon Territory, Canada, using a local dense seismic array. Bulletin of the Seismological Society of America, 103(6), 3341–3346. https://doi.org/10.1785/0120130068

Mezger, J. E. (1997). Tectonometamorphic evolution of the Kluane metamorphic assemblage, SW Yukon: evidence for late Cretaceous eastward subduction of oceanic crust underneath North America. Unpublished PhD thesis, University of Alberta, Edmonton. 306 p.

Mezger, J. E. (2000). 'Alpine-type' ultramafic rocks of the Kluane metamorphic assemblage, southwest Yukon: Oceanic crust fragments of a late Mesozoic back-arc basin along the northern Coast Belt. Geology, January, 127–138.

Mezger, J. E. (2003). Geology of the Dezadeash Range and adjacent areas of the northern Coast Mountains (115A), southwestern Yukon: Re-examination of a terrane boundary In: Yukon Exploration and Geology 2002 (edited by Emond, D. S. & Lewis, L. L.). Exploration and Geological Services Division, Yukon Region, Indian and Northern Affairs Canada, 149–163.

Morgan G.C., Rawling G.E., & Sobkowicz J.C. (1992) Evaluating total risk to communities from large debris flows. In: Proc 1st Canadian Symp on Geotechnique and Natural Hazards, Vancouver, Canada, pp 225–236

Morino, C., Conway, S. J., Sæmundsson, Þ., Kristinn Helgason, J., Hillier, J., Butcher, F. E. G., Balme, M. R., Jordan, C., & Argles, T. (2019). Molards as an indicator of permafrost degradation and landslide processes. Earth and Planetary Science Letters, 516, 136–147. https://doi.org/10.1016/j.epsl.2019.03.040

Morris, J. D., Gosse, J., Brachfeld, S., & Tera, F. (2002). Cosmogenic Be-10 and the solid Earth: studies in geomagnetism, subduction zone processes, and active tectonics. Reviews in mineralogy and geochemistry, 50(1), 207-270.

Muller, J.E. (1966). Glaciation Kluane Lake, Yukon Territory. Geological Survey of Canada, "A" Series Map 1178A. https://doi.org/10.4095/107353

NRCan (2022) National Earthquake Database, Natural Resources Canada. http://earthquakescanada.nrcan.gc.ca/stndon/NEDB-BNDS/index-en.php. Accessed 31 April 2022.

Nishiizumi, K., Kohl, C. P., Arnold, J. R., Klein, J., Fink, D., & Middleton, R. (1991). Cosmic ray produced 10Be and 26Al in Antarctic rocks: exposure and erosion history. Earth and Planetary Science Letters, 104(2–4), 440–454. https://doi.org/10.1016/0012-821X(91)90221-3

Northern Climate ExChange, (2011). Compendium of Yukon Climate Change Science 2003-2011. Northern Climate ExChange, Yukon Research Centre, Yukon College, 179 p.

Ojo, A. O., Kao, H., Jiang, Y., Craymer, M., & Henton, J. (2021). Strain accumulation and release rate in Canada: Implications for long-term crustal deformation and earthquake hazards. Journal of Geophysical Research: Solid Earth, 126, e2020JB020529. https://doi.org/10.1029/2020JB020529

Olsson I.U. (1986). A study of errors in 14C dates of peat and sediment. Radiocarbon 28(2A):429–35.

Parks Canada (2019). World Heritage Sites in Canda: Klaune/ Wrangell-St.Elias/ Glacier Bay/ Tatshenshini-Alsek. Retrieved from https://www.pc.gc.ca/en/culture/spm-whs/sites-canada/sec02d

Patton, A. I., Rathburn, S. L., & Capps, D. M. (2019). Landslide response to climate change in permafrost regions. In Geomorphology (Vol. 340, pp. 116–128). Elsevier B.V. https://doi.org/10.1016/j.geomorph.2019.04.029

Patton, A. I., Rathburn, S. L., Capps, D. M., McGrath, D., & Brown, R. A. (2021). Ongoing Landslide Deformation in Thawing Permafrost. Geophysical Research Letters, 48(16). https://doi.org/10.1029/2021GL092959

Peel, M. C., Finlayson, B. L., & McMahon, T. A. (2007). Updated world map of the Köppen-Geiger climate classification. Hydrology and earth system sciences, 11(5), 1633-1644.

Perkins, S. (2012) Death toll from landslides vastly underestimated. *Nature*. https://doi.org/10.1038/nature.2012.11140

Pfiffner O.A., Hermanns R.L., Davies T.R. & Clague J.J. (2021). Editorial: Rock Avalanches. Front. Earth Sci., 9, 651642. doi: 10.3389/feart.2021.651642.

Rainville, R. A., & Gajewski, K. (2013). Holocene environmental history of the Aishihik Region, Yukon, Canada. Canadian Journal of Earth Sciences, 50(4), 397–405. https://doi.org/10.1139/cjes-2012-0103

Rampton, V.N. (1979a) Surficial geology and geomorphology, Burwash Creek, Yukon Territory. Geological Survey of Canada, Map 6-1978.

Rampton, V.N. (1979b) Surficial geology and geomorphology, Generc River, Yukon Territory. Geological Survey of Canada, Map 7-1978.

Rampton, V.N. (1979c) Surficial geology and geomorphology, Congdon Creek, Yukon Territory. Geological Survey of Canada, Map 8-1978.

Rampton, V.N., Paradis, S. (1982) Surficial geology and geomorphology, Taye Lake, Yukon Territory. Geological Survey of Canada, Map 14-1981.

Reimer, P. J., Austin, W. E., Bard, E., Bayliss, A., Blackwell, P. G., Ramsey, C. B., ..., & Talamo, S. (2020). The IntCal20 Northern Hemisphere radiocarbon age calibration curve (0–55 cal kBP). *Radiocarbon*, *62*(4), 725-757.

Reimer, P. J., Brown, T. A., & Reimer, R. W. (2004). Discussion: reporting and calibration of post-bomb 14C data. Radiocarbon, 46(3), 1299-1304.

Reyes, A. V., Luckman, B. H., Smith, D. J., Clague, J. J., & Van Dorp, R. D. (2006). Tree-ring dates for the maximum Little Ice Age advance of Kaskawulsh Glacier, St. Elias Mountains, Canada. Arctic, 14-20.

Roots, C. & Hart, C. (2004). Bedrock Geology. In: Ecoregions of the Yukon Territory: Biophysical properties of Yukon landscapes, C.A.S. Smith, J.C. Meikle and C.F. Roots (eds.), Agriculture and Agri-Food Canada, PARC Technical Bulletin No. 04-01, Summerland, British Columbia, p. 11-14.

Sæmundsson, Þ., Morino, C., Helgason, J. K., Conway, S. J., & Pétursson, H. G. (2018). The triggering factors of the Móafellshyrna debris slide in northern Iceland: Intense precipitation, earthquake activity and thawing of mountain permafrost. Science of the Total Environment, 621, 1163–1175. https://doi.org/10.1016/j.scitotenv.2017.10.111

Scudder, G. G. E. (1997). Environment of the Yukon. Insects of the Yukon. Biological Survey of Canada (Terrestrial Arthropods), Ottawa, 13-57. Retrieved from https://www.researchgate.net/publication/252860187

Seitz, G. J., Haeussler, P. J., Crone, A. J., Lipovsky, P., & Schwartz, D. P. (2008). Eastern Denali Fault Slip Rate and Paleoseismic History, Kluane Lake Area, Yukon Territory, Canada. AGU Fall Meeting, 1, 1947. http://adsabs.harvard.edu/abs/2008AGUFM.T53B1947S%5Cnhttp://file//localhost(null)%5Cnpapers3://publication/uuid/1347ADDA-7C9B-4E32-985A-EB825304AE85

Smart, D. F., & Shea, M. A. (1985). Galactic cosmic radiation and solar energetic particles. *Handbook of geophysics and the space environment*, 6-1.Smith, C.A.S., Meikle, J.C., and Roots, C.F. (editors), (2004). Ecoregions of the Yukon Territory: Biophysical properties of Yukon landscapes. Agriculture and Agri-Food Canada, PARC Technical Bulletin No. 04-01, Summerland, British Columbia, 313 p.

Smith, C.A.S., Meikle, J.C., & Roots, C.F. (editors), 2004. Ecoregions of the Yukon Territory: Biophysical properties of Yukon landscapes. Agriculture and Agri-Food Canada, PARC Technical Bulletin No. 04-01, Summerland, British Columbia, 313 p. Retrieved from http://www.env.gov.yk.ca/animals-habitat/documents/ecoregions_of_yukon_reduced.pdf

Soukup, M. (2018). Testing a myogenic isotope method to monitor relief generation over millions of years. Honours thesis, Dalhousie University, Halifax. 170 p.

Stanley, B. (2012). Structural Geology and Geochronology of the Kluane Schist, Southwestern Yukon Territory. M.Sc. thesis, University of Waterloo, 101 p.

Stashin, S. A. (2021). Late Cenozoic Basin Evolution of the western Canadian Arctic Archipelago: The Beaufort Formation and Iperk Sequence. M.Sc. Thesis, Dalhousie University, Halifax. 168 p.

Sterlacchini, S., Frigerio, S., Giacomelli, P., & Brambilla, M. (2007). Landslide risk analysis: a multi-disciplinary methodological approach. Natural Hazards and Earth System Sciences, 7(6), 657-675.

Strong, T.R., & Driscoll, R.L. (2016). A process for reducing rocks and concentrating heavy minerals: U.S. Geological Survey Open-File Report 2016–1022, 16 p. http://dx.doi.org/10.3133/ofr20161022

Studhalter, R.A., Glock, W.S. & Agerter, S.R. (1963). Tree growth. The Botanical Review, 29(3), 245–365. https://doi.org/10.1007/BF02860823

Stuiver, M., & Polach, H. (1977). Discussion Reporting of 14C Data. Radiocarbon, 19(3), 355-363. doi:10.1017/S0033822200003672.

Sturzenegger, M., Stead, D., Gosse, J., Ward, B., & Froese, C. (2015). Reconstruction of the history of the Palliser Rockslide based on 36Cl terrestrial cosmogenic nuclide dating and debris volume estimations. Landslides, 12(6), 1097–1106. https://doi.org/10.1007/s10346-014-0527-4

Thurber Consultants Ltd. (1989). Kluane terrain hazard mapping study final report. Unpublished engineering report. Vancouver, B.C.: 25 p.

Toohey, M., & Sigl, M. (2017). Volcanic stratospheric sulfur injections and aerosol optical depth from 500 BCE to 1900 CE. Earth System Science Data, 9(2), 809-831. https://doi.org/10.5194/essd-9-809-2017.

Torbenson, M. C. A., Stahle, D. W., Villanueva Díaz, J., Cook, E. R., & Griffin, D. (2016). The relationship between earlywood and latewood ring-growth across North America. Tree-Ring Research, 72(2), 53–66. https://doi.org/10.3959/1536-1098-72.02.53

Turner, D. G., Ward, B. C., Bond, J. D., Jensen, B. J., Froese, D. G., Telka, A. M., ... & Bigelow, N. H. (2013). Middle to Late Pleistocene ice extents, tephrochronology and paleoenvironments of the White River area, southwest Yukon. Quaternary Science Reviews, 75, 59-77.

Turner, D. G., Ward, B. C., Froese, D. G., Lamothe, M., Bond, J. D., & Bigelow, N. H. (2016). Stratigraphy of Pleistocene glaciations in the St Elias Mountains, southwest Yukon, Canada. Boreas, 45(3), 521-536.

USGS (2022) ANSS comprehensive earthquake catalog, United States Geological Survey, http://earthquake.usgs.gov/earthquakes/search/. Accessed 30 April 2022.

UWICER (2017). Dendrochronology Manual. Ugyen Wangchuck Institute for Conservation and Environmental Research, Department of Forests and Park Services. UWICER Press, Lamai Goempa, Bumthang, Bhutan. ISBN: 978-99936-743-0-6.

Wahl, H.E., Fraser, D.B., Harvey, R.C., Maxwell, J.B. (1987) Climate of the Yukon. Climatological Studies, Environment Canada, Ottawa, 40, 323 pp.

Wang, D., & Liu, Q. (2021). Hydrodynamics of froth flotation and its effects on fine and ultrafine mineral particle flotation: A literature review. Minerals Engineering, 173, 107220. Elsevier Ltd. https://doi.org/10.1016/j.mineng.2021.107220

Wang, X. C., & Geurts, M. A. (1991). Late Quaternary pollen records and vegetation history of the southwest Yukon Territory: A review. Géographie physique et Quaternaire, 45(2), 175-193.

Ward, B. C., Bond, J. D., & Gosse, J. C. (2007). Evidence for a 55-50 ka (early Wisconsin) glaciation of the Cordilleran ice sheet, Yukon Territory, Canada. Quaternary Research, 68(1), 141–150. https://doi.org/10.1016/j.yqres.2007.04.002

Willenbring-Staiger, J. (2005). Glacial Erosion in Atlantic and Arctic Canada Determined by Terrestrial In Situ Cosmogenic Nuclides and Ice Sheet Modelling. PhD thesis. Dalhousie University, 246 p.

Yukon Geological Survey (2022). Yukon digital bedrock geology. Yukon Geological Survey. Retrieved from https://yukon.maps.arcgis.com/home/item.html?id=b950bd1b5afa4eab9885d505a3ed98b4

Zêzere, J. L., Ferreira, A. B., & Rodrigues, M. L. (1999). Landslides in the North of Lisbon Region (Portugal): conditioning and triggering factors. Physics and Chemistry of the Earth, Part A: Solid Earth and Geodesy, 24(10), 925-934.

Appendix A.

Field Photo

Supplementary Data Files

File names: field_photos.pdf

Description: Field photos from the 2019 field season.

Appendix B.

Cosmogenic Nuclide Exposure Dating Data (^{10}Be, ^{36}Cl)

Supplementary Data Files

File names: summarized_tcn_data.xlsl

summarized_tcn_data.pdf

Description: All the laboratory, field observations, and technical notes documented during my time at the Cosmic Ray Isotope Sciences at Dalhousie (CRISDal) Lab in 2019/2020.

Appendix C.

Radiocarbon Samples

Supplementary Data Files

File names: radiocarbon_samples.pdf

Description: Photos of radiocarbon samples sent to Keck Carbon Cycle AMS Facility.

Appendix D.

Dendrochronological Samples

Supplementary Data Files

File names: dendro_samples.pdf

Description: Photos of dendrochronological samples analyzed at Simon Fraser University.